2007-05-25

Dynamic Full-Scale Testing of a Pile Cap with Loose Silty Sand Backfill

Immanuel Kaleoonalani Runnels
Brigham Young University - Provo

CYCLIC AND DYNAMIC FULL-SCALE TESTING OF A PILE CAP WITH LOOSE SILTY SAND BACKFILL

by

Immanuel K. Runnels

A thesis submitted to the faculty of

Brigham Young University

in partial fulfillment of the requirements for the degree of

Master of Science

Department of Civil and Environmental Engineering

Brigham Young University

August 2007

BRIGHAM YOUNG UNIVERSITY

GRADUATE COMMITTEE APPROVAL

of a thesis submitted by

Immanuel K. Runnels

This thesis has been read by each member of the following graduate committee and by majority vote has been found to be satisfactory.

Date	Kyle M. Rollins, Chair
Date	Travis M. Gerber
Date	Richard J. Balling

BRIGHAM YOUNG UNIVERSITY

As chair of the candidate's graduate committee, I have read the thesis of Immanuel K. Runnels in its final form and have found that (1) its format, citations, and bibliographical style are consistent and acceptable and fulfill university and department style requirements; (2) its illustrative materials including figures, tables, and charts are in place; and (3) the final manuscript is satisfactory to the graduate committee and is ready for submission to the university library.

Date

Kyle M. Rollins
Chair, Graduate Committee

Accepted for the Department

E. James Nelson
Graduate Coordinator

Accepted for the College

Alan R. Parkinson
Dean, Ira A. Fulton College of Engineering and Technology

ABSTRACT

CYCLIC AND DYNAMIC FULL-SCALE TESTING OF A

PILE CAP WITH LOOSE SILTY SAND BACKFILL

Immanuel K. Runnels

Department of Civil and Environmental Engineering

Master of Science

Pile caps are used in foundation design to aid multiple single piles to act as a pile group to resist lateral forces that may cause overturning moments. The pile cap and pile group resist these forces by pile-soil-pile interaction, base and side friction along the pile cap-backfill interface, and passive earth resistance. Passive earth resistance has been neglected in design due to a limited amount of full-scale testing.

This research presents the results of a combination of hydraulic actuator and eccentric-mass shaker full-scale testing of a pile cap with loose silty sand backfill to quantify the contribution of the passive earth resistance to the lateral force resistance. The test cap is 1.12 m tall and 5.18 x 3.05 m in plan view, connecting 12 steel pipe piles (324mm O.D) placed in a 4 x 3 pattern with center-to-center spacing of 4.4 and 3.3 pile-diameters in the long and short dimensions, respectively.

The hydraulic actuator applied a static load to the system (backfill + pile group) while the eccentric-mass shaker introduced cyclic and dynamic loading to the system. The passive earth resistance accounted for approximately 22% of the total system resistance, with piles contributing approximately 78%. Furthermore, the results produce general correlations between cyclic and dynamic effects on degradation of the backfill provided by the testing and soil characteristics obtained, including target (static) displacement, dynamic displacement amplitude, stiffness, and damping. The dynamic displacement amplitudes during the eccentric mass shaker tests typically ranged between .4 and 2 mm for frequencies between 5 and 9.5 Hz representing behavior under reloading conditions rather than virgin loading conditions. Generally, the presence of the loose silty sand backfill nearly doubled the dynamic stiffness of the pile cap. The stiffness of the backfill and pile cap combined was typically between 100 and 200 kN/mm for frequencies between 4 and 8 Hz, while the stiffness for the backfill alone was typically a decreasing trend between 100 and 40 kN/mm for the same frequency range. The overall isolated loose silty sand damping ratio shows a general increasing trend with values from 32% to 55% for frequencies 3 and 8 Hz.

ACKNOWLEDGMENTS

I wish to express my sincere appreciation to both Dr. Kyle M. Rollins and Dr. Travis M. Gerber for their continual sacrifice of time and energy in a sincere effort to mentor me through the presented research. I have learned dedication, team work, and fortitude from their active examples and will continue to admire them in their individual contributions to the engineering profession, academia, and church and civic service. Most of all, I value the friendship and trust that flourished in our work.

I would also like to recognize Dr. Richard J. Balling for his time as a member of my committee and for the mentoring that he provided while I completed my undergraduate and graduate work. Janice S. Sorenson is an amazing asset to the Civil Engineering Department and here dedication to the students greatly appreciated.

Thanks to Kamehameha Schools Bishop Estates (KSBE) for their generous financial support as well as scholarships provided by the Civil Engineering department.

Most of all, I would like to recognize my parents, Russell and Esther Runnels for their relentless guidance and support. They have been instrumental in providing me with the example of genuine love and hard work and an environment for growth. I am also grateful for the support and understanding provided by my brothers and sister throughout my many years of schooling.

This research was supported through an FHWA pooled-fund study entitled: "Dynamic Passive Pressure on Abutments and Pile Caps" with contributions from the state departments of transportation from California, Montana, New York, Oregon and Utah. The Utah Department of Transportation served as the lead agency with Daniel Hsiao as the contract manager. Funding was provided through Utah DOT contract number 069148. This support is gratefully acknowledged; however, the conclusions presented in this study do not necessarily reflect the view of the sponsoring agencies.

TABLE OF CONTENTS

CHAPTER 1- STATEMENT OF RESEARCH 1

1.1 INTRODUCTION 1

1.2 SCOPE OF RESEARCH 2

CHAPTER 2- LITERATURE REVIEW 5

2.1 INTRODUCTION 5

2.2 RELATED RESEARCH 5

2.3 STATE OF PRACTICE 21

CHAPTER 3- SITE CHARACTERIZATION 27

3.1 INTRODUCTION 27

3.2 SURFACE CONDITIONS 27

3.3 SUBSURFACE CONDITIONS 28

3.4 LOOSE SILTY SAND BACKFILL PROPERTIES 30

CHAPTER 4- TEST SETUP AND METHODOLOGY 39

4.1 INTRODUCTION 39

4.1.1 GENERAL 40

4.1.2 TEST PILE CAP DESCRIPTION 40

4.1.3 REACTION PILE CAP DESCRIPTION 41

4.1.4 HYDRAULIC ACTUATORS 42

4.1.5 ECCENTRIC MASS SHAKER 42

4.1.6 INSTRUMENTATION 44

4.2 TESTING PROCEDURE 50
CHAPTER 5- STATIC RESPONSE OF LOOSE SILTY SAND 53
5.1 INTRODUCTION 53
5.2 LOAD-DEFLECTION CURVES 54
5.2.1 LOOSE SILTY SAND BACKFILL SYSTEM RESISTANCE 54
5.2.2 BASELINE PILE RESISTANCE 57
5.2.3 STATIC PASSIVE EARTH RESISTANCE 61
5.2.4 COMPARISON OF MEASURED & COMPUTED PASSIVE FORCE 62
CHAPTER 6- DYNAMIC RESPONSE OF BACKFILL 67
6.1 INTRODUCTION 67
6.2 DATA PROCESSING PROCEDURES 68
6.3 LOOSE SILTY SAND BACKFILL DYNAMIC SYSTEM RESPONSE 71
6.3.1 LOAD-DEFLECTION CURVES 71
6.3.2 DYNAMIC DISPLACEMENT AMPLITUDE 74
6.3.3 STIFFNESS AND DAMPING 76
6.4 BASELINE PILE DYNAMIC RESISTANCE RESPONSE 79
6.4.1 LOAD-DEFLECTION CURVES 79
6.4.2 DYNAMIC DISPLACEMENT AMPLITUDE 81
6.4.3 STIFFNESS AND DAMPING 84
6.5 DYNAMIC PASSIVE EARTH RESISTANCE RESPONSE 86
6.5.1 LOAD-DEFLECTION CURVES 86
6.5.2 STIFFNESS AND DAMPING 88
CHAPTER 7- CONCLUSION 91
REFERENCES 95
APPENDIX A: INSTRUMENTATION LOCATIONS 97

LIST OF TABLES

Table 2.1: Centrifuge test performed on model of embedded foundation 10

Table 2.2: Measured material damping for loops of increasing displacement amplitude 11

Table 2.3: Approximate movement required to reach minimum active and maximum passive earth pressure conditions. 21

Table 4.1: Test History for August 18, 2005 for loose silty sand 51

Table 4.2: Test history for August 16, 2005 for baseline pile system testing 51

Table 5.1: Summary of assumptions used to compute P_{ult} 63

Table 5.2: Measured and computed ultimate passive force comparison 64

Table A.1: Instrumentation locations 98

Table A.2: Instrumentation locations (continued) 99

LIST OF FIGURES

Figure 2.1: Load-deflection plot showing how the passive force was calculated 6

Figure 2.2: Proposed cyclic hyperbolic model 7

Figure 2.3: Computed and measured load-deflection curves for passive pressure load tests 9

Figure 2.4: Measured load-deflection response for Test BSP 10

Figure 2.5: Load-deflection responses with and without pile-cap embedment in natural soil (left), and comparison between natural soil and compacted gravel backfill (right) 13

Figure 2.6: Effect of backfill type and density on load-deflection response 14

Figure 2.7: Flow chart of structure-embankment modeling procedure 15

Figure 2.8: Schematic view of model of structure-embankment interaction 17

Figure 2.9: Response spectra for computed and recorded motions at PSO 18

Figure 2.10: Applied load versus pile cap displacement at load point 19

Figure 2.11: (Left) Computed load-deflection curves for base friction, passive pressure resistance, pile-soil-pile interaction resistance, and total computed load with gap formation. (Right) Comparison of measured load displacement curve with curves computed using five different methods for computing ultimate passive resistance on pile cap 20

Figure 2.12: Hyperbolic load-deflection curve 24

Figure 2.13: Flowchart of LSH procedures 25

Figure 3.1: Site Map and geotechnical test locations (after Cole 2003) 28

Figure 3.2: Idealized soil profile and strength properties 29

Figure 3.3: Average grain size distribution for backfill soil 31
Figure 3.4: Histogram of unit weight testing of loose silty sand 32
Figure 3.5: First in-place direct shear test max shear stress versus normal stress 33
Figure 3.6: Second in-place direct shear test max shear stress versus normal stress..... 33
Figure 3.7: Shear stress versus deflection of loose silty sand..... 34
Figure 3.8: Maximum shear stress versus normal stress of loose silty sand..... 35
Figure 3.9: 40-60 silica sand shear stress versus deflection curves 35
Figure 3.10: Sand-on-sensor shear stress versus deflection curves 36
Figure 3.11: Combined normal stress versus shear stress curves 36
Figure 4.1: Schematic showing main components used in the testing program 40
Figure 4.2: Sample tekscan real time window 45
Figure 4.3: Equipment setup between test cap and reaction cap 46
Figure 4.4: Pile cap face with instrumentation……..47
Figure 4.5: Plan View of testing facility 48
Figure 4.6: Test setup in front of test cap 49
Figure 4.7: Instrumentation setup on front of pile cap before backfill 49
Figure 5.1: The load-displacement response of the pile cap with loose silty sand backfill 55
Figure 5.2: System load-deflection curves..... 56
Figure 5.3: The load-displacement response of the pile cap with no backfil 57
Figure 5.4: Pull backs and pile only push during testing 58
Figure 5.5: Baseline (no backfill) load-deflection curves..... 60
Figure 5.6: Loose silty sand passive earth load-deflection curves..... 62
Figure 5.7: Measured and computed load-deflection curve comparison 65
Figure 6.1: System free body diagram with system forces represented 68

Figure 6.2: Loose silty sand static and dynamic system load-deflection curves 72

Figure 6.3: Loose silty sand static and dynamic system load-deflection curves (function of frequency) 72

Figure 6.4: Loose silty sand system load-deflection curves (function of frequency) 73

Figure 6.5: System dynamic displacement amplitude versus forcing frequency 75

Figure 6.6: System dynamic displacement amplitude versus resistance. 75

Figure 6.7: Loose silty sand system stiffness versus forcing frequency 77

Figure 6.8: Loose silty sand system damping versus forcing frequency 78

Figure 6.9: Baseline pile static and dynamic system load-deflection curves 79

Figure 6.10: Baseline pile static and dynamic system load-deflection curves in terms of frequency 80

Figure 6.11: Baseline pile load-deflection curve in terms of frequency 81

Figure 6.12: Pile (baseline) dynamic displacement amplitude versus forcing frequency 82

Figure 6.13: Pile (baseline) dynamic displacement amplitude versus resistance 83

Figure 6.14: Pile (baseline) stiffness versus forcing frequency 84

Figure 6.15: Pile (baseline) damping versus forcing frequency 85

Figure 6.16: Static and dynamic passive earth resistance load-deflection curves 86

Figure 6.17: Static and dynamic passive earth resistance load-deflection curves in terms of frequency 87

Figure 6.18: Loose silty sand passive earth stiffness versus forcing frequency 88

Figure 6.19: Loose silty sand passive earth damping versus forcing frequency 90

CHAPTER 1-STATEMENT OF RESEARCH

1.1 INTRODUCTION

Building and bridge foundations often experience lateral load conditions in zones of high seismic or wind activity. Passive earth forces and pressures provided by surrounding soil are often neglected in design. However, the surrounding soil have been proven to provide foundation systems with a large amount of lateral resistance capacity (Duncan and Mokwa, 2001; Cole and Rollins, 2006). Passive earth pressures under static loading conditions can be calculated by using Rankine, Coulomb, or log-spiral methods, although recent research suggests that the log-spiral method may be the most accurate (Duncan and Mokwa, 2001; Rollins and Sparks, 2002). Although the developments of load-displacement relationships have not reached a conclusive widely accepted methodology various methods have been developed such as those employed by CALTRANS (2004), based on Maroney (1995) which assumes a simple linear elastic relationship when estimating the passive earth pressure. Another method is that proposed by Duncan and Mokwa (2001) which uses a hyperbolic relationship for passive earth pressure as a function of deflection.

Numerous methods accounting for static load analysis of passive earth pressure exist; however, very little has been done to address earthquake loading. Earthquake

loading includes cyclic and dynamic effects. Cyclic loading tend to decrease soil strength and stiffness, whereas dynamic loadings is believed to increase soil strength and stiffness due to material and radiation damping. Brigham Young University, in collaboration with the Network for Earthquake Engineering Simulation (NEES) and Utah Department of Transportation (UDOT), has proposed the development of load-displacement curves for typical soils used as backfill in pile cap and abutment applications to account for dynamic and cyclic effects and observe soil behavior. In addition, dynamic displacement amplitude, stiffness and damping will also be observed and investigated.

1.2 SCOPE OF RESEARCH

Typical soils used in the proposed investigation were silty sand compacted to a dense state, silty sand compacted to a loose state, and two gravel backfill section compacted to a dense state. A pile cap test (with no backfill) was also conducted to aid in isolation of the backfill response. The backfill of concern for this thesis will be the silty sand compacted to a loose state.

The data obtained from the loose silty sand and pile (baseline) tests will be used first to quantify the overall contribution of passive earth resistance to the total system resistance in static testing using load-deflection curves. Also, the degradation of the passive earth resistance under cyclic, dynamic loading will be measured and reported. This will aid in summarizing what portion of passive earth degradation is due to relaxation of the soil and subsurface system and what portion is due to cyclic, dynamic effects. Measured ultimate horizontal passive force, P_{ult}, and load-deflection curves will also be compared to commonly practiced methods of estimating passive force.

To better observe and investigate soil behavior during cyclic, dynamic loading the dynamic displacement amplitude, stiffness, and damping will be plotted versus frequency. This will allow for observation of soil behavior to lead to conclusion about whether or not loose silty sand exhibits increases in stiffness and damping with an increase in forcing frequency.

CHAPTER 2-LITERATURE REVIEW

2.1 INTRODUCTION

Pile caps are generally designed to aid piles in distributing and resisting vertical loads, lateral loads, and overturning moments as a group, instead of individually. The pile cap system provides multiple modes of resistance which includes "pile-soil-pile interaction, base and side friction along the concrete-soil interface, the rotational restraint provided by the pile to pile cap connection, and passive earth resistance" (Rollins and Cole 2005). Very little research has been done to assess the contribution of passive earth resistance; although various areas of pile cap lateral resistance have been explored. The type of tests conducted in this research range from the use of model testing to full scale testing.

2.2 RELATED RESEARCH

The following contains literature reviewed pertaining and related to pile cap lateral resistance due to passive earth pressure.

Cole and Rollins (2006)

Cole and Rollins (2006) performed cyclic lateral load tests on full-scale 4 x 3 pile group attached to a concrete pile cap 1.12 m in height by 3.05 m in length by 5.18 m in width. These tests included two tests without any backfill around the pile cap, four tests with different soil types backfilled around the pile cap, and one test with a trench excavated between the pile cap and backfill (Rollins and Cole 2005). The first two tests isolated the passive resistance contributed by the piles without backfill. The following four tests used backfill consisting of clean sand, silty sand, fine gravel, and coarse gravel. The load-deflection curves without backfill were then subtracted from the various backfill load-deflection curves to obtain the passive resistance attributed by the backfill as shown in Figure 2.1.

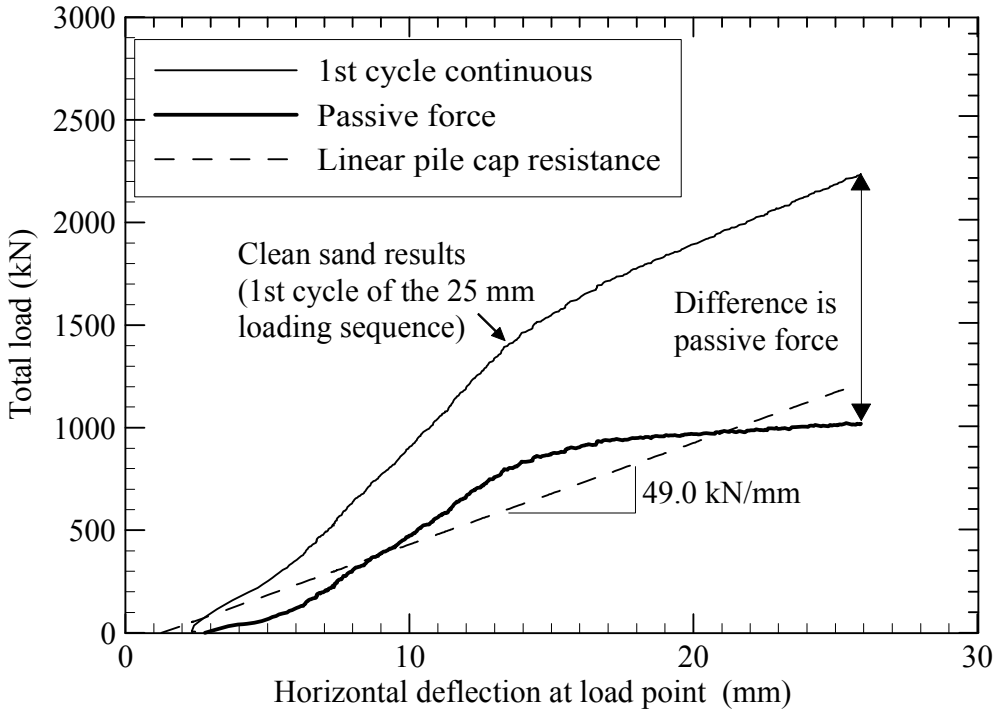

Figure 2.1: Load-deflection plot showing how the passive force was calculated

Rollins and Cole (2006) concluded that the log spiral method in general predicts well the observed failure surface geometry and also was typically within 15% of the measured value (Cole and Rollins 2006). Overall, the pile cap lateral passive resistance contributed between 33% and 47% of the total lateral resistance. To account for cyclic loading conditions, where backfill soil stiffness degenerates and a gap forms between the backfill and pile cap, a cyclic hyperbolic model was developed. Figure 2.2 shows the relationships between reloaded soil stiffness, Kr, as a function of apparent soil movement, Δ_s, and Δ_p, as related to previous maximum deflection that were established.

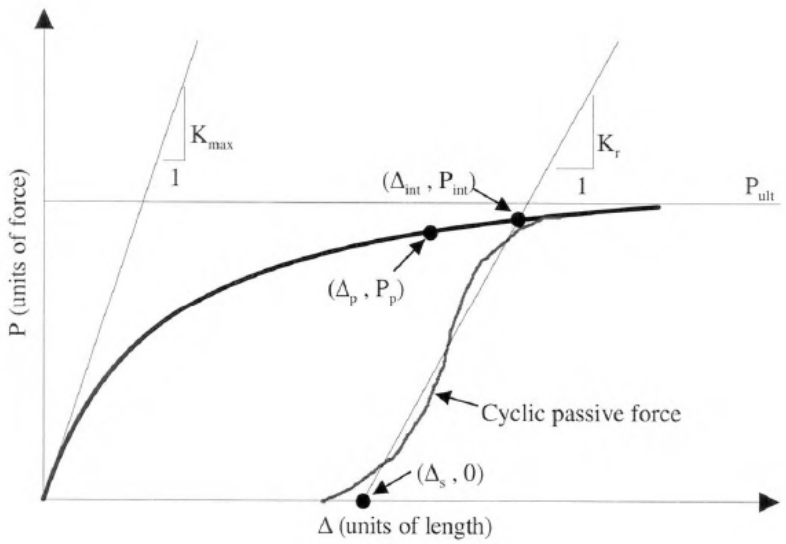

Description of terms
Δ_p – Previous deflection (units of length)
P_p – Previous passive resistance (units of force)
K_{max} - Initial soil stiffness of the load-deflection curve (units of force/length)
K_r - Reloaded soil stiffness (units of force/length)
Δ_s - Apparent soil movement (units of length)
Δ_{int} - Deflection intercept of K_r and hyperbolic relationship (units of length)
P_{int} – Passive load intercept of K_r and hyperbolic relationship (units of force)

Figure 2.2: Proposed cyclic hyperbolic model

Comparing measured results with estimated load-deflection curves using the cyclic hyperbolic model provided varying results but was reasonably successful in modeling the measured passive force-deflection behavior, despite its simplicity (Cole and Rollins 2006).

Duncan and Mokwa (2001)

Duncan and Mokwa (2001) conducted two full-scale tests on a 1.1 meter height, 1.9 meter length, and .9 meter width anchor block. The block was loaded by a ram, using a 2 x 2 pile group as a reaction. The load was applied incrementally over approximately a 90 minute interval. The first test was performed in indigenous soils; namely, hard partially saturated sandy clay and sandy silt. After the first test, the natural soil in front of the anchor block was excavated to a depth equal to the block height and 2.3 meters away from the block. The second test was then performed on crushed run gravel backfill.

Their study considered four elements "(1) movement of structure; (2) strength and stiffness of the soil; (3) adhesion between the structure and soil; and (4) shape of the structure" (Duncan and Mokwa 2001). Duncan and Mokwa acknowledged various methods common in estimating passive earth pressures. They concluded that the test data was best estimated by the Log Spiral Theory with the Ovesen-Brinch Hansen correction. In Figure 2.3, load-deflection curve ranges are computed and measured values fall within provided ranges. The natural soil is shown to have considerably more load resistive strength than that of the gravel backfill.

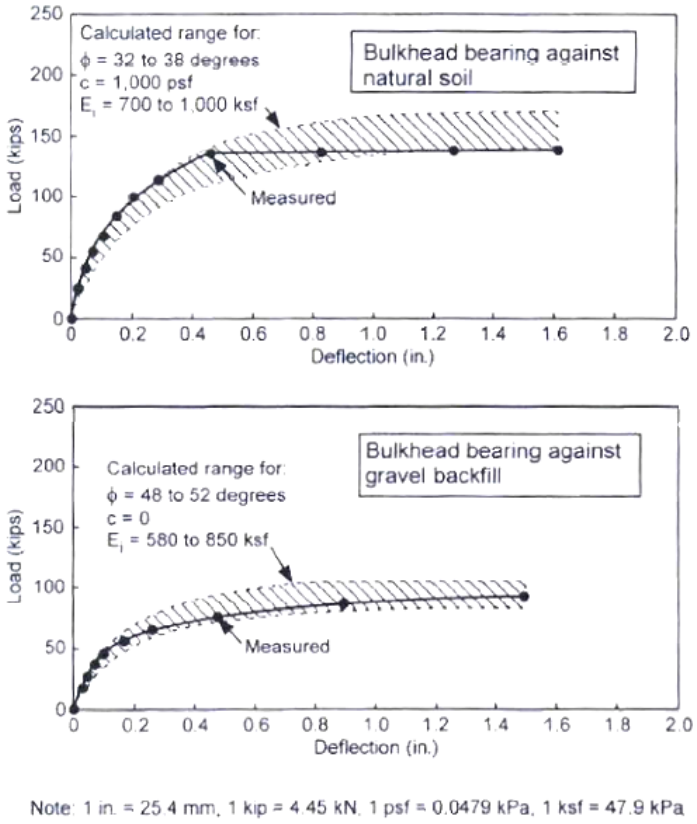

Figure 2.3: Computed and measured load-deflection curves for passive pressure load tests

Gadre and Dobry (1998)

Gadre and Dobry (1998) simulated a foundation in lateral cyclic loading with dimension .84 meter height, 1.14 meter length, and 1.14 meter width using a 28 mm × 38 mm × 38 mm rigid aluminum block. The centrifuge test element was placed in a confining box containing dry Nevada No. 120 at 75% relative density to replicate in-situ conditions. Seven centrifuge tests were conducted (see Table 2.1) to isolate base and side shears, as well as passive and active forces. Three-dimensional static nonlinear finite-element analyses were also performed to predict the measured test data.

Table 2.1: Centrifuge test performed on model of embedded foundation

Test (1)	Partial Contribution: Base shear (2)	Partial Contribution: Sidewall shear (3)	Partial Contribution: Passive/ active force (4)	Vertical load at the base (kN) (5)	Measured ultimate lateral capacity (kN) (6)	Remarks (7)
B	Yes	No	No	53	44	$\mu \sim 0.82$
BL	Yes	No	No	108	88	$\mu \sim 0.82$
S	No	Yes	No	53	38	—
P	No	No	Yes	53	124	$K_p \sim 11.1$
SP	No	Yes	Yes	53	165	—
BSP	Yes	Yes	Yes	53	214	—
BSPL	Yes	Yes	Yes	108	245	—

Note: B = Base shear, S = Sidewall shear, P = Passive/active force, L = vertical Load at the base, and combinations thereof.

They found that, "clear yielding occurs in all tests at a yield displacement of ~2.4 ± 1 cm, and ultimate lateral capacity is typically reached shortly afterward at a displacement somewhere between 3.5 and 5 cm" (Gadre and Dobry 1998). As shown in the load-displacement hysteresis graph (see Figure 2.4), the ultimate lateral load associated with the before mentioned ultimate lateral capacity of the footing was 214 kN.

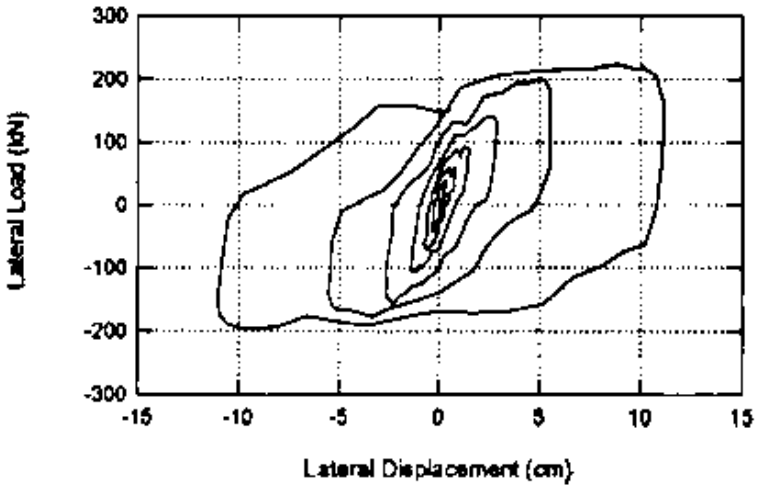

Figure 2.4: Measured load-deflection response for Test BSP

In addition, they found that the passive earth resistance contributed >50% of the total stiffness "at all displacement amplitudes" (Gadre and Dobry 1998). Damping experienced by the test element was developed in the soil and the soil-foundation interfaces. Gadre and Dobry used β_{eq} ratios to estimate and compare damping characteristic in each of the seven tests (Table 2.2). The passive resistance was also found to be a "dominant contributor to the damping of the foundation" (Gadre and Dobry 1998).

Table 2.2: Measured material damping for loops of increasing displacement amplitude

Test (1)	Loop [u (cm)] 1 [0.3] (2)	2 [0.7] (3)	3 [1.4] (4)	4 [2.8] (5)	5 [5.6] (6)	6 [10.9] (7)
B						
Area (kN/cm)	3.6	13.2	50.1	181.5	557.6	1,463.6
β_{eq}	0.12	0.14	0.18	0.24	0.36	0.47
BL						
Area (kN/cm)	3.8	23.1	91.6	334.4	1,006.9	2,747.8
β_{eq}	0.11	0.13	0.17	0.23	0.32	0.45
S						
Area (kN/cm)	4.0	21.5	65.2	160.6	429.1	1,032.9
β_{eq}	0.32	0.37	0.37	0.37	0.39	0.39
P						
Area (kN/cm)	14.9	44.7	135.5	500.2	1,571.6	3,981.5
β_{eq}	0.31	0.29	0.29	0.32	0.41	0.47
SP						
Area (kN/cm)	18.7	69.4	202.4	644.9	1,825.6	5,043.2
β_{eq}	0.32	0.33	0.33	0.35	0.38	0.44
BSP						
Area (kN/cm)	21.1	83.8	267.5	825.8	2,324.2	6,880.6
β_{eq}	0.28	0.30	0.30	0.31	0.37	0.47
BSPL						
Area (kN/cm)	21.5	91.9	300.0	962.1	3,244.2	8,027.5
β_{eq}	0.24	0.24	0.25	0.29	0.38	0.48

Goel and Chopra (1997)

Goel and Chopra (1997) performed analysis on actual earthquake data collected from the instrumented US 101/Painter Street Overpass in Rio Dell, California. Using two

of the nine sets of collected motion data, a structural idealization was created and dynamic equilibrium equations applied to produce abutment forces. These forces were plotted against the computed deformation to obtain the force-deformation hysteresis loops. The loops were then isolated to determine abutment-soil system stiffness and capacity.

The analysis revealed that abutment stiffness was high in the early stages of the earthquakes characterized by small deformations. However, as deformation increased, stiffness decreased during high levels of shaking. As deformations subsided, abutment stiffness was gradually regained only in part and over time. Analysis further found that CALTRANS design values for the abutment capacity in the normal direction were twice that of the actual values. This inconsistency was caused by an assumption of 7.7 ksf (at the time of this study) for soil passive earth pressure. Presently, that design value is at 5.0 ksf (Caltrans, 2004). This discontinuity is due to the overestimation of passive soil resistance in the normal direction. However, design values for loading in the transverse direction compared well with the actual data obtained in the analysis.

Mokwa and Duncan (2001)

Mokwa and Duncan (2001) performed thirty-one full-scale static lateral load tests. The test group consisted of three groups of four HP 10 × 42 piles, a buried concrete wall with no piles, and two single HP 10 × 42 piles. The pile cap dimensions were 1.5 m × 1.5 m. Load-deflection response data was taken in natural soil conditions with and without pile cap embedment, gravel and other common backfill conditions, and no soil conditions.

In natural conditions, pile cap resistance produced small deflections of <2.5 mm (see Figure 2.5). However, removing the soil from sides and front of cap to isolate pile lateral resisting strength produced large deflections in comparison. Gravel backfill conditions resulted in ~4 mm deflections.

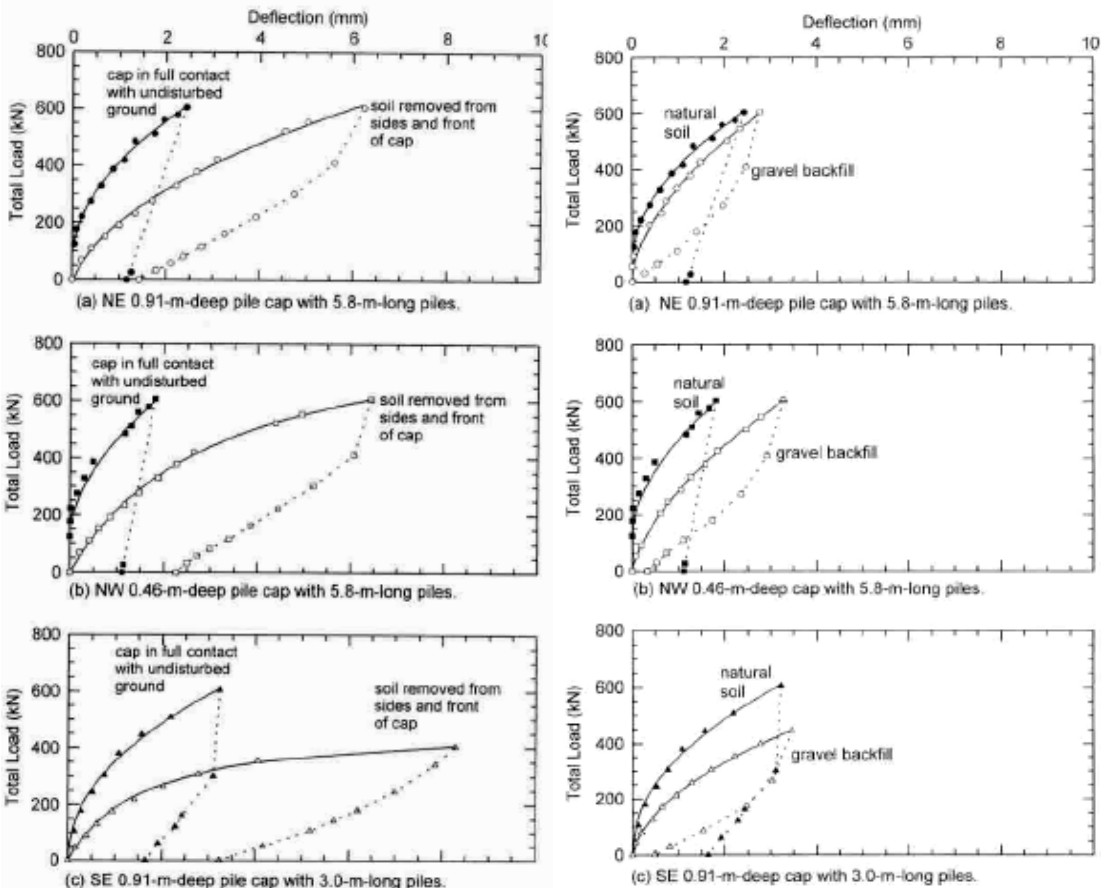

Figure 2.5: Load-deflection responses with and without pile-cap embedment in natural soil (left), and comparison between natural soil and compacted gravel backfill (right)

Compacted and loose sand conditions were also included in these tests. Various sand conditions were modeled, tested and their performance compared with the typical gravel backfill as well as natural soil conditions (see Figure 2.6). Overall, Mokwa and Duncan (2001) found that when natural gravel and sand backfills are used to resist lateral

loading, they provided ~50% of the overall lateral resistance. Furthermore, they concluded that the passive resistance developed in the front of the pile cap is proportional to the strength and stiffness of the soil around the cap. Also, deflections can be minimized by increasing the depth or thickness of the cap.

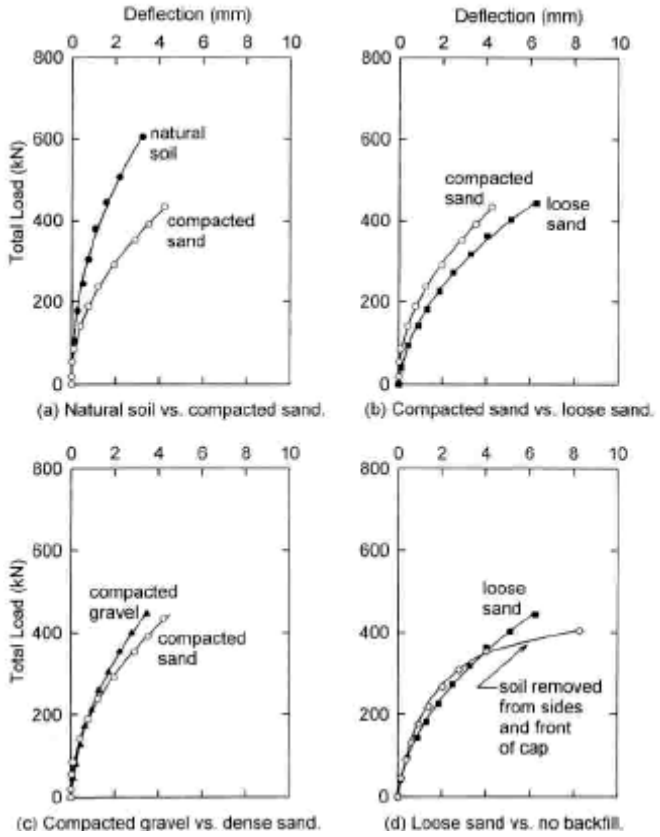

Figure 2.6: Effect of backfill type and density on load-deflection response

Price and Eberhard (2005)

Price and Eberhard (2005) identified the importance of four phenomena that are typically neglected in seismic analysis and modeling that contribute to the complex interaction between bridges and embankments. These phenomena are three-dimensional embankment response, nonlinear soil behavior, soil-structure interaction, and

embankment scattering. By conducting parametric studies which compared measured and computed values for abutment acceleration response histories, response spectra, structural periods, damping ratios, and abutment stiffness, they were able to conclude that considering three-dimensional embankment effects and specification of soil properties is important.

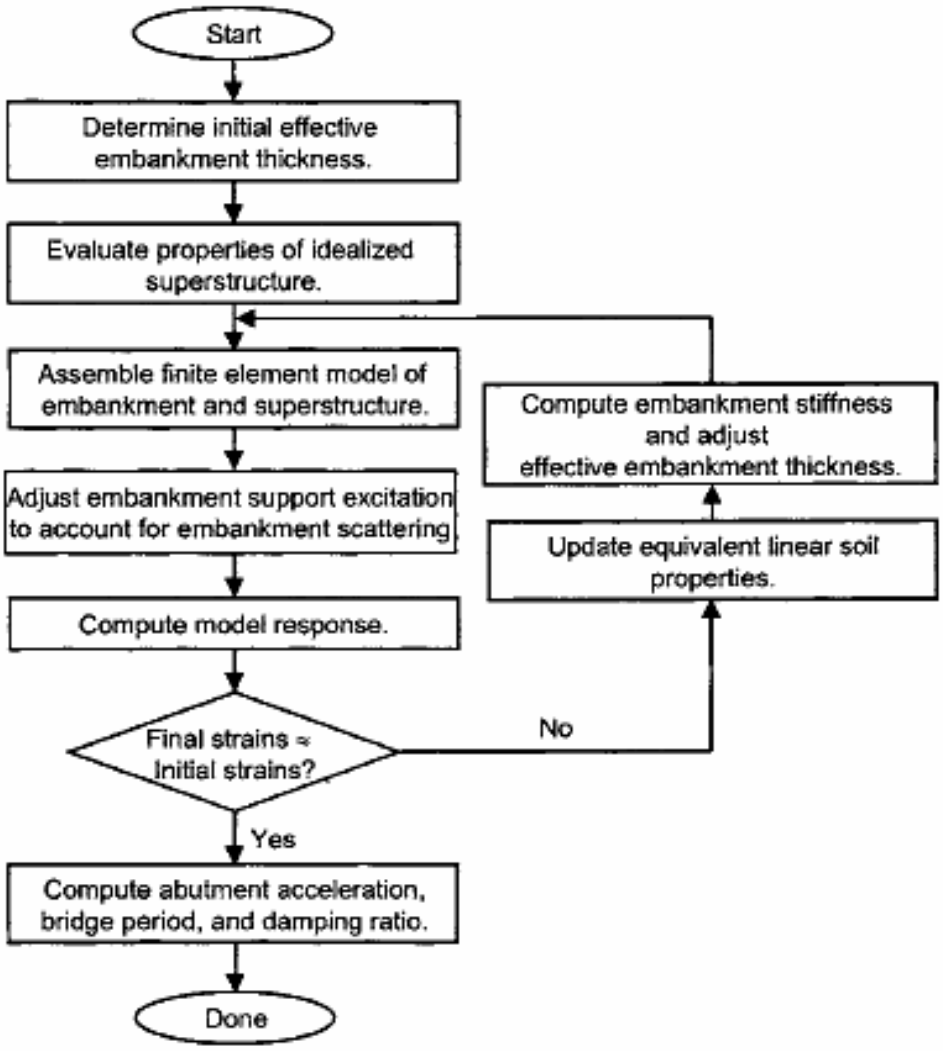

Figure 2.7: Flow chart of structure-embankment modeling procedure

To model these phenomena, an iterative process was used and is shown in Figure 2.7. Key aspects of the model include "(1) a procedure to account for three-dimensional effects using a strain-dependent variable thickness; (2) implementation of an equivalent linear soil material model to account for nonlinear soil behavior; (3) calibration of two equivalent single-degree-of-freedom systems accounting for soil-structure interaction in the horizontal and vertical directions; (4) and modeling of embankment scattering with a Green's function model of half-space compliance" (Price and Eberhard 2005).

The first aspect of the model uses strain-dependent variable thickness to account for three-dimensional effects. Beginning with equation 2.1, an initial effective embankment thickness, B_0 is found. Following along the model flow chart (Figure 2.7), if the model must iterate, B must be recalculated using equation 2.2 which is dependant upon the embankment stiffness K.

$$B_0 = (2.00 + 0.53H)\left(\frac{H}{\omega}\right)^{-0.15} \quad \textbf{(2.1)}$$

$$\frac{B}{B_0} = \frac{K}{K_0} + \ln(1+\alpha_s)\left[\frac{1}{\alpha_s} - \frac{1}{\frac{K}{K_0}\sqrt{1+\alpha_x} - 1}\right] \quad \textbf{(2.2)}$$

The second aspect of the model is the implementation of an equivalent linear soil material model to account for soil behavior. Figure 2.8 shows the proposed linear model and the effects of soil-structure interaction are included in the model. Building upon

equations provided by Humar (1990), Price and Eberhard are able to find values for k_{eq}, m_{eq}, and ξ_{eq}. The other key aspects will not be mentioned in this summary.

After the model was created, the results were compared to recorded data and case studies from the Painter Street Overcrossing (PSO) located in Rio Dell, California which experienced six particular earthquakes. Figure 2.9 represents the comparisons of some of the computed and measured earthquakes and their respective response spectra.

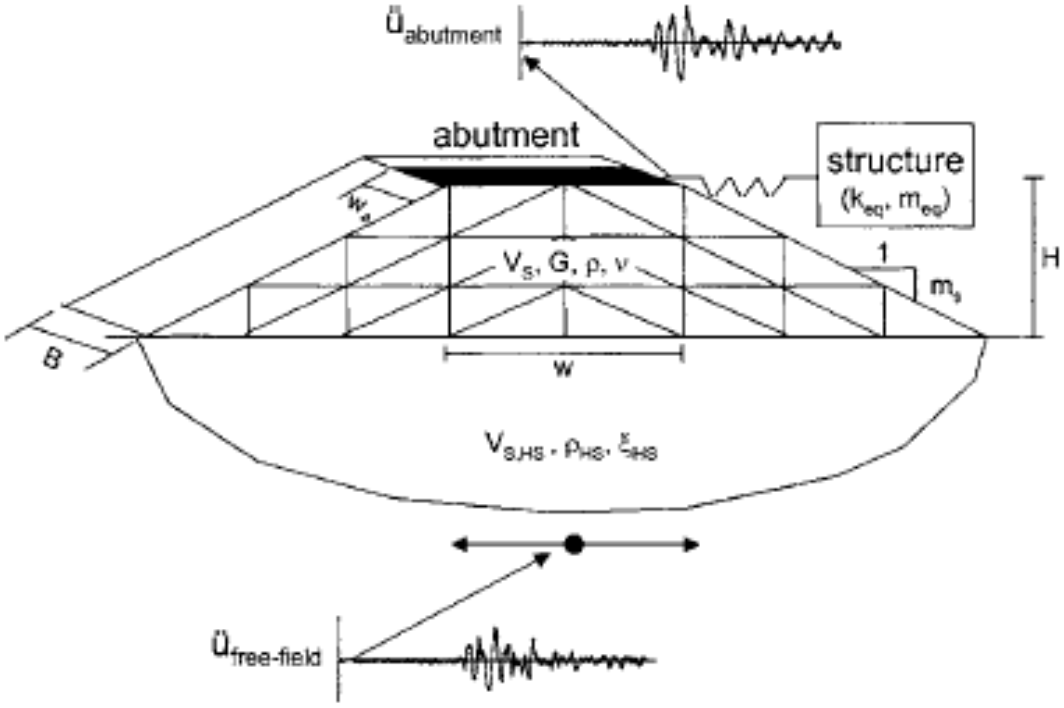

Figure 2.8: Schematic view of model of structure-embankment interaction

Price and Eberhard (2005) summarized five conclusions that are listed here. First, accuracy of computed seismic demand for a range of earthquakes was significantly improved by the use of a varying thickness plane-strain model. Second, increases of 13-64% were observed for the effective fundamental transverse periods of the equivalent

linear model, "leading to significantly altered abutment response spectra". Third, abutment response was "significantly decreased" when soil-structure interaction is considered. However, this computed response was not sensitive to small variations in soil parameters. Fourth, embankment scattering was negligible for "most intense ground motion" and "significant" for moderate ground shaking. Finally, the shear-wave velocity and modulus reduction for the embankment soils must be accurately modeled.

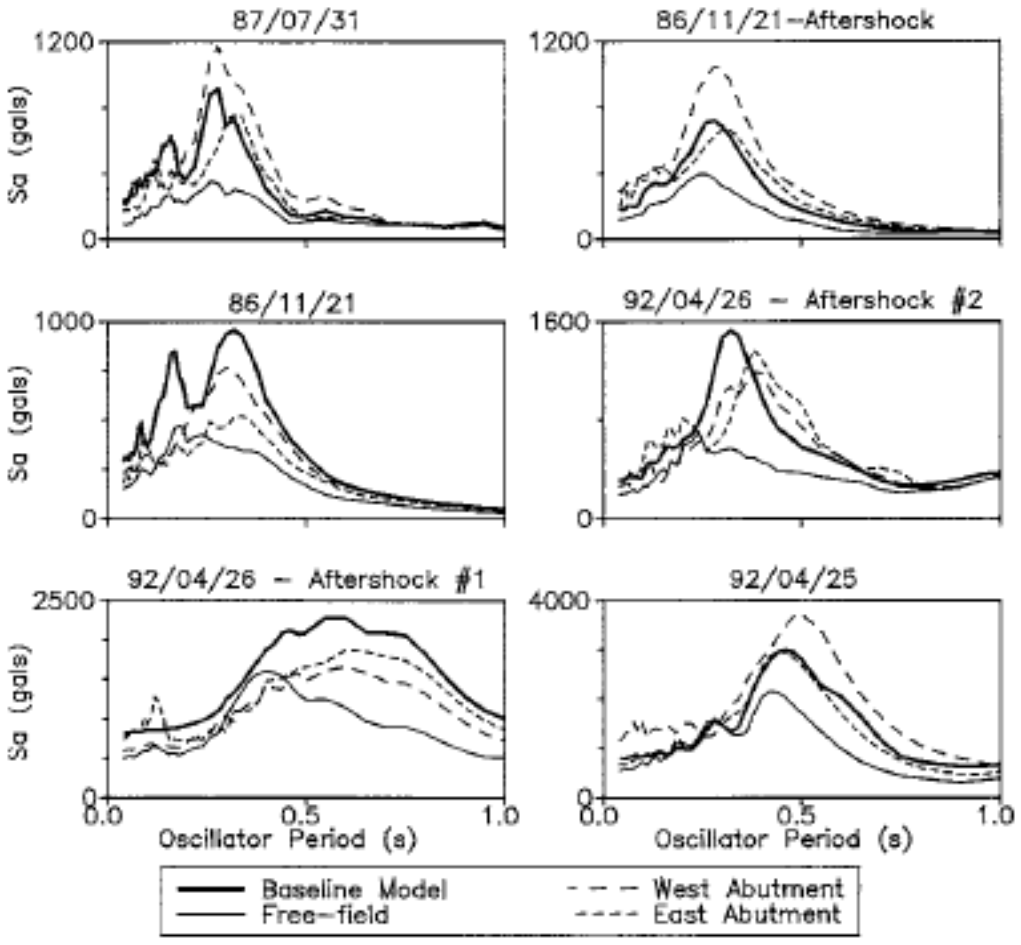

Figure 2.9: Response spectra for computed and recorded motions at PSO

Rollins and Sparks (2002)

Rollins and Sparks (2002) conducted a static lateral load test on a full-scale 3 × 3 driven pile group with "fixed-head" end constraints. The lateral force resisting components included: pile-soil-pile interaction, passive pressure on the backside of the pile cap, and base friction on the pile cap. Side friction was not considered in this test. The backfill consisted of sandy gravel, compacted to ASTM standard D1157. Load, displacement, and strain monitoring instrumentation were applied and data collected.

Lateral load test results were plotted against deflection as shown in Figure 2.10. Loading was applied in incremental, static setting, which allowed for a well defined curve and a maximum loading of 2750 kN. Small differential deflections were observed between front, middle, and back row piles.

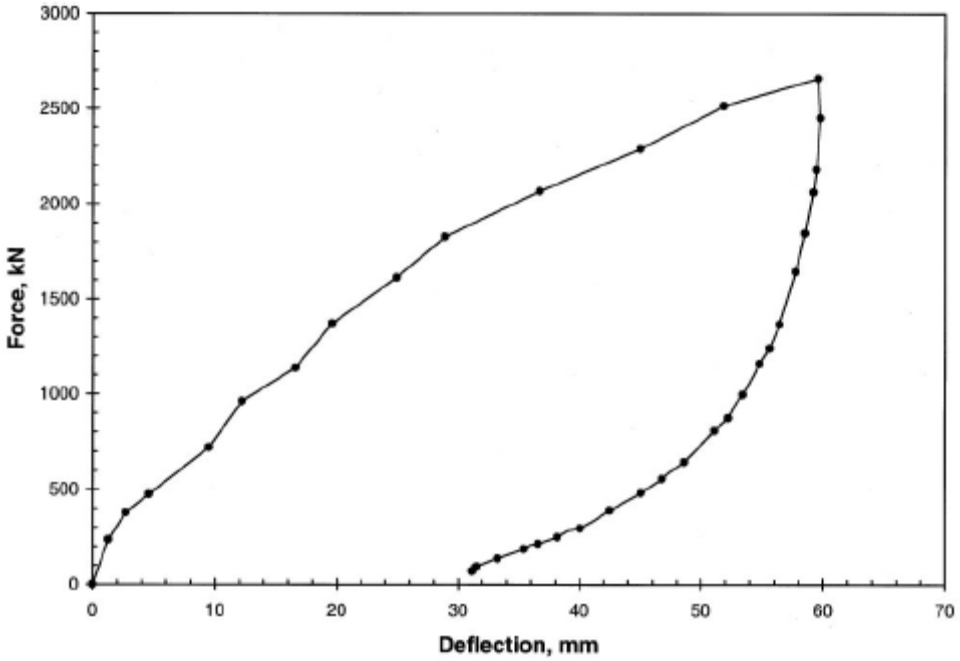

Figure 2.10: Applied load versus pile cap displacement at load point

Base Interface friction resistance was based on simple calculations and on normalized skin friction mobilization curves developed by Rollins et al. (1997). Full base friction capacity was reached with a deflection of 12.7 mm. Pile-soil-pile interaction was analyzed using p-multipliers, P_M. This concept treats each pile in a pile group as a single pile and multiplies the stiffness of the soil by a reduction factor P_M. Passive earth pressures and forces were computed using log-spiral, Coulomb, Rankine, Caltrans, and Group methods. The log-spiral method provided the best comparison with measured resistance values which compares well to the findings of Duncan and Mokwa (2001). A summary of data is included in Figure 2.11.

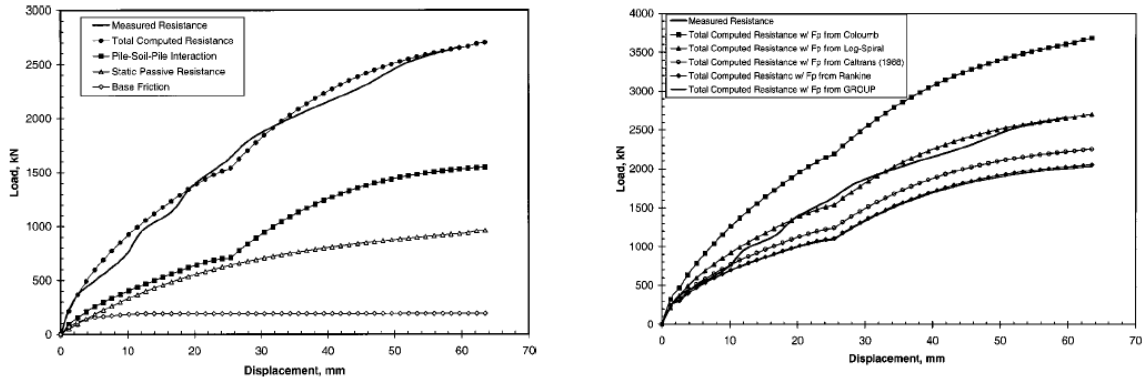

Figure 2.11: (Left) Computed load-deflection curves for base friction, passive pressure resistance, pile-soil-pile interaction resistance, and total computed load with gap formation. (Right) Comparison of measured load displacement curve with curves computed using five different methods for computing ultimate passive resistance on pile cap

Rollins and Sparks (2002) concluded that at low displacements (≈25 mm) the total resistance consists of 13% base friction, 46% pile-soil-pile interaction, and 41% passive resistance. At higher displacements (≈70 mm), the total resistance is made up of 7% base friction, 57% pile-soil-pile interaction, and 36% passive resistance. Overall, it was found

that a movement of 6% of the pile cap height was needed to mobilize full passive resistance in the dense compacted sandy gravel.

2.3 STATE OF PRACTICE

Currently, there are four methods widely accepted for computing ultimate passive earth pressure, namely, Caltrans (2004), AASHTO (2004), Duncan and Mokwa (2001), and Shamsabadi (2006).

AASHTO (2004)

Referencing the work of Clough and Duncan 1991, AASHTO calculates approximate values of relative movement required to reach active or passive earth pressure conditions (see Table 2.3).

Table 2.3: Approximate movement required to reach minimum active and maximum passive earth pressure conditions.

		Value of Δ/H	
Type of Backfill		Active	Passive
Dense sand		0.001	0.01
Medium-dense sand		0.002	0.02
Loose sand		0.004	0.04
Compacted silt		0.002	0.02
Compacted lean clay		0.01[a]	0.05[b]
Compacted fat clay		0.01[a]	0.05[b]

[a]Δ= movement of top of wall required to reach minimum active or maximum passive pressure, by tilting or lateral translation. H= height of wall
[b]Under stress conditions close to the minimum active or maximum passive earth pressures, cohesive soils creep continually. The movements shown would produce active or passive pressures only temporarily. With time, the movements will continue if pressures remain constant. If movement remains constant, active pressures will increase with time and passive pressures will decrease with time.

However, this method does not account for the path that the soil takes from zero to the ultimate active or passive earth pressures. Most engineers assume that it is linear, others that it is hyperbolic. Furthermore, it is still uncertain if these assumptions break down under cyclic loading conditions. Questions about whether cyclic loads will follow the same loading path cannot yet be answered. Dynamic loading conditions and associated damping effects are known to increase the passive earth pressure values but much is unknown about how the load and unloading paths will be influenced

Caltrans (2004)

Acting on the recommendations of Maroney (1995), Caltrans adopted a Bi-Linear Load deflection curve. This curve normalizes all walls to the response of the tested 5.5 ft wall used by Maroney. Using the following two equations (see Equations 2.1 and 2.2), Caltrans produces a force deflection curve.

$$P_{ult} = (5.0\ ksf) * (\frac{H}{5.5\ ft}) * A_{wall} \quad \textbf{(2.1)}$$

$$k_{abut} = (20\ kip/in) * (\frac{H}{5.5\ ft}) * width \quad \textbf{(2.2)}$$

This method neglects soil type, density, and strength properties. These neglected characteristics are essential to calculate spectral displacements or spectral acceleration, S_d and S_a respectively.

If soil type is assumed to be soft but conditions are stiffer than expected the S_d will be unconservative in calculating the force produced, as expressed in Equation 2.3.

$$F = m * (\frac{\omega^2}{g}) * S_d \quad \textbf{(2.3)}$$

Duncan and Mokwa (2001)

As previously mentioned in the literature review, Duncan and Mokwa did account for crucial aspects of passive earth pressure by including strength and stiffness of the soil and friction or adhesion between the structure and soil to name a few. The calculation of P_{ult} is dependant upon some of these soil characteristics and is placed in a general hyperbolic relationship equation as seen below.

$$P = \frac{y}{\left[\frac{1}{K_{\max}} + R_f \frac{y}{P_{ult}}\right]} \quad \textbf{(2.4)}$$

The initial stiffness K_{max} calculations are based on estimated values for E (Young's Modulus) and v (Poisson's ratio). Also, the failure ratio R_f are estimated by experience. This gives the hyperbolic load-deflection curve presented in Figure 2.12. Although the test data that was obtained compared well with the theoretical load-deflection curve calculated using the methodology above, the loading was such that it did not include cyclic and dynamic effects that may be experienced if the soil had experienced an earthquake.

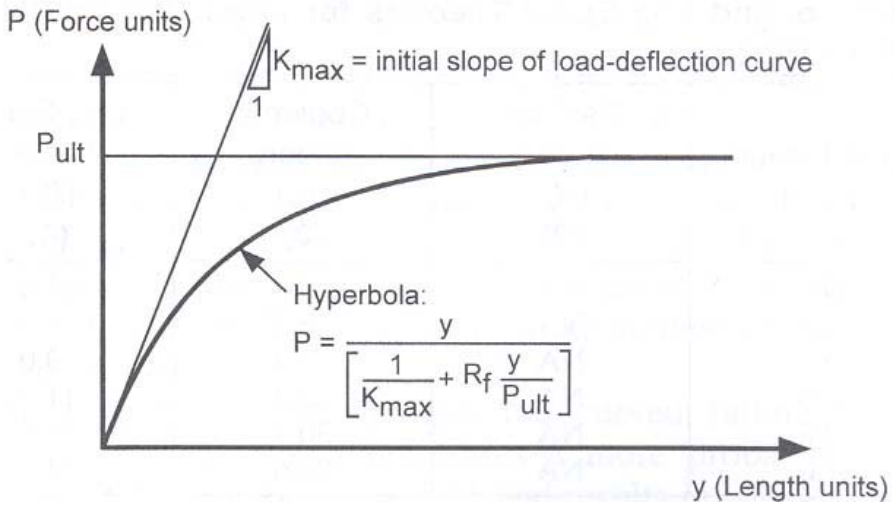

Figure 2.12: Hyperbolic load-deflection curve

Shamsabadi (2001)

Considering bridges under lateral earthquake loading, Shamsabadi (2001) makes use of mobilized Logarithmic-Spiral failure surfaces coupled with modified Hyperbolic soil stress-strain behavior (know as the LSH model) to estimate abutment nonlinear force-displacement capacity as a function of wall displacement and soil backfill properties. Using seven common soil parameters, namely ε_{50}, R_f, ε_f, φ_i, c_i, F_{ih}, and y_i, a common engineer will be able to build an LSH model that has been found in good agreement with measured force-displacement capacities. Figure 2.13 best illustrates this method using a flowchart. Please refer to Shamsabadi (2001) for appropriate information regarding tables and equation referred to in this flowchart.

In step one, the user would estimate model parameters ε_{50}, R_f, and ε_f. That is strain at 50% of failure strength, failure ratio, and strain at failure respectively. These

parameters define the hyperbolic curve that is characteristic of soils and its stress-strain relationship as described by Duncan and Chang (1970).

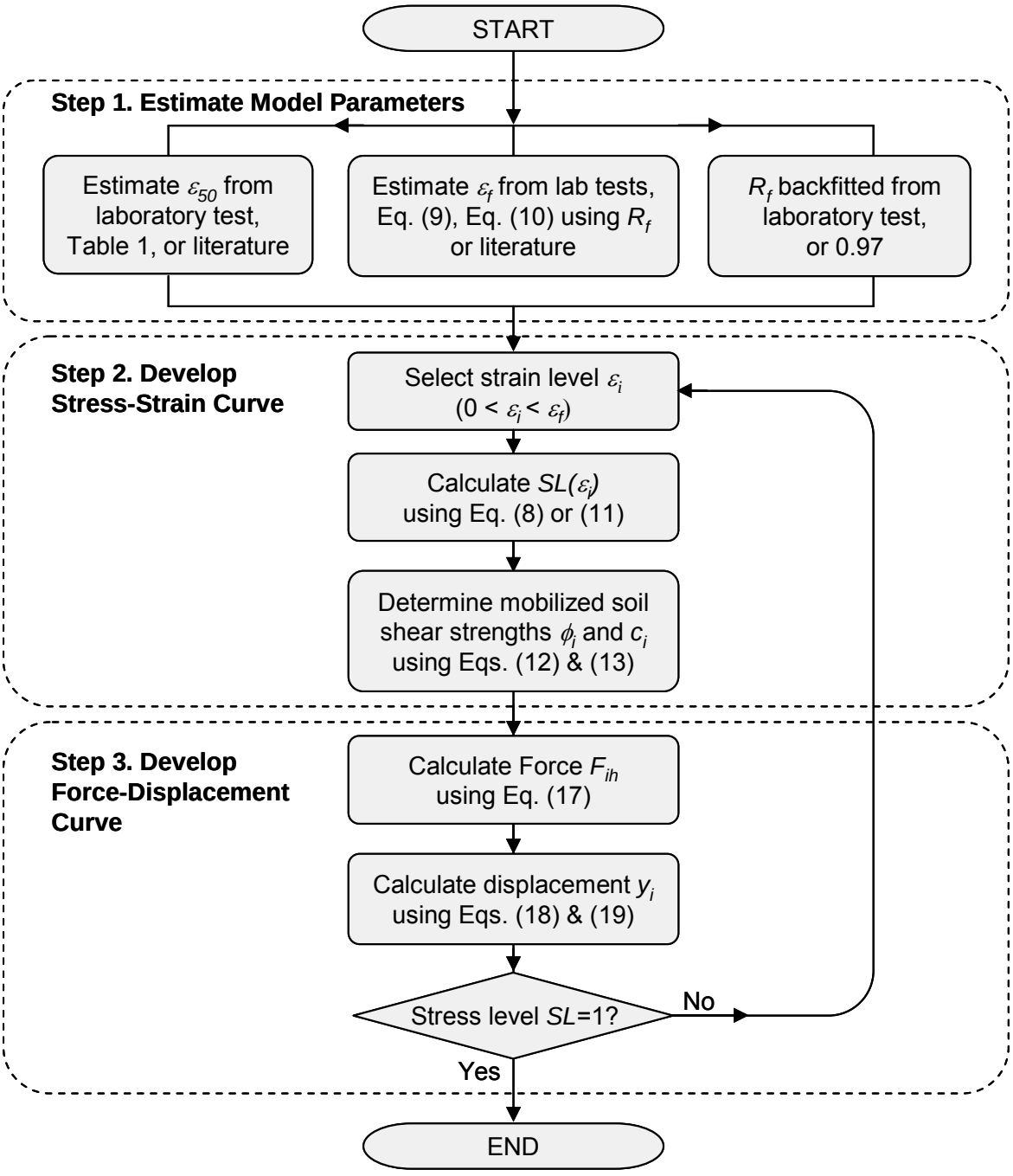

Figure 2.13: Flowchart of LSH procedures

In step two, the user selects a strain level by choosing ε_i. This will determine parameters φ_i and c_i which are backfill parameters leading to estimating nonlinear abutment-backfill capacity. This is where Shamsabadi begins to build upon the current discussion. He considers the mobilized failure zone as vertical slices and estimates the internal forces of each slice to estimate F_{ih} and y_i in step three. Using F_{ih} and y_i a force-displacement curve can be created and checked through an iterative process.

CHAPTER 3-SITE CHARACTERIZATION

3.1 INTRODUCTION

The research for this thesis was conducted at the Interstate 15 (I-15) National Testbed site located in Salt Lake City, Utah at South Temple Street near 700 West underneath Interstate 15. The site used for this study was also used previously for lateral pile group interaction testing (Rollins and Cole 2005) and passive force-deflection testing (Cole 2003). As part of these studies, a comprehensive geotechnical investigation was conducted to characterize the subsurface soils at the testing site. A map of the site showing the location of the test cap relative to previous geotechnical testing locations and bridge foundations for the interstate is shown in Figure 3.1.

3.2 SURFACE CONDITIONS

The site is relatively vacant, located underneath Interstate-15. Several full-scale pile and pile group tests have been performed in this area, both during and after the reconstruction of I-15. The surface topography is relatively flat at an elevation of approximately 1,289 meters. In the immediate vicinity of the test pile cap, the surface soils were excavated prior to construction, creating an excavated ground surface 1.1 m on average below the surrounding ground surface.

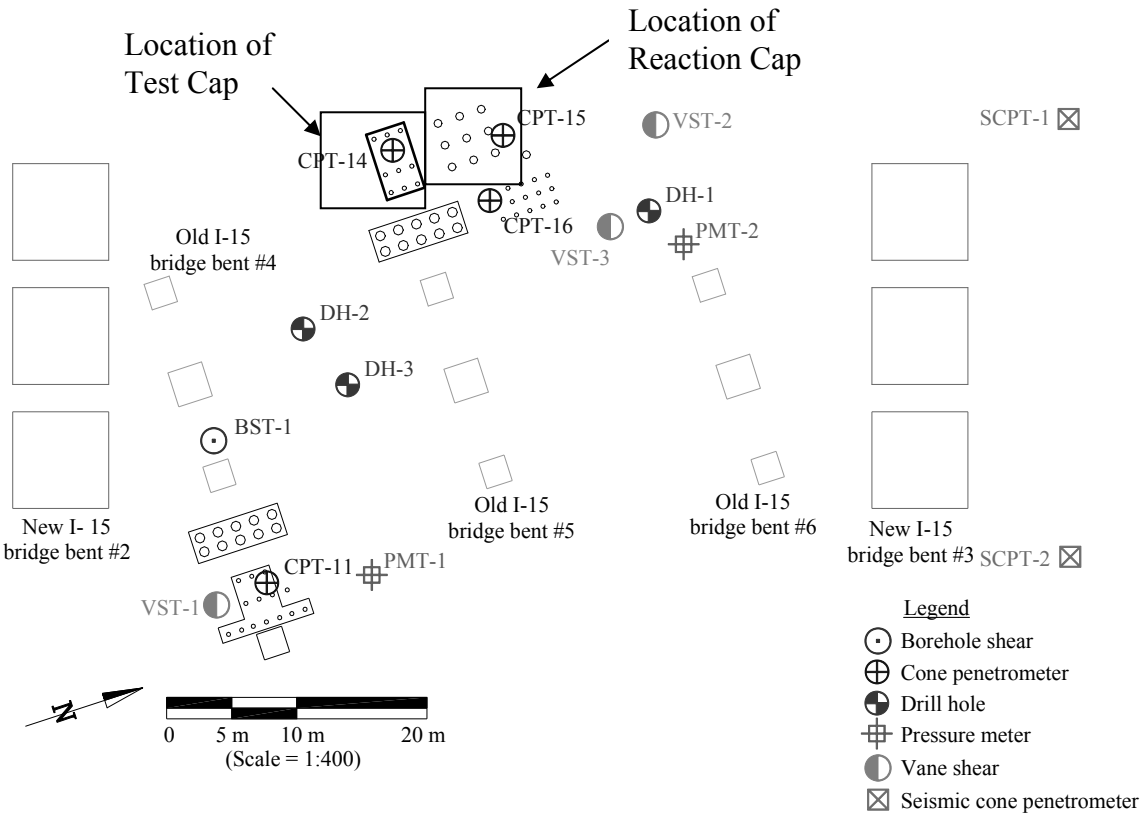

Figure 3.1: Site Map and geotechnical test locations (after Cole 2003)

3.3 SUBSURFACE CONDITIONS

The results of several geotechnical investigations conducted at the test site have been complied and presented by Cole (2003). In-situ testing consisted of standard penetration testing (SPT), cone penetration testing (CPT), pressuremeter testing (PMT), vane shear testing (VST), bore hole shear testing (BST), shear wave velocity testing (SCPT), nuclear density testing, and in-situ direct shear testing. The SPT test relies on blow counts to ascertain approximate relative densities of soil strata. The CPT test yielded various data such as cone tip resistance (q_c), sleeve friction (f_s), and pore water

pressure (u). A number of CPT tests were conducted with agreeable results indicating that subsurface conditions are generally consistent throughout the site. Laboratory results

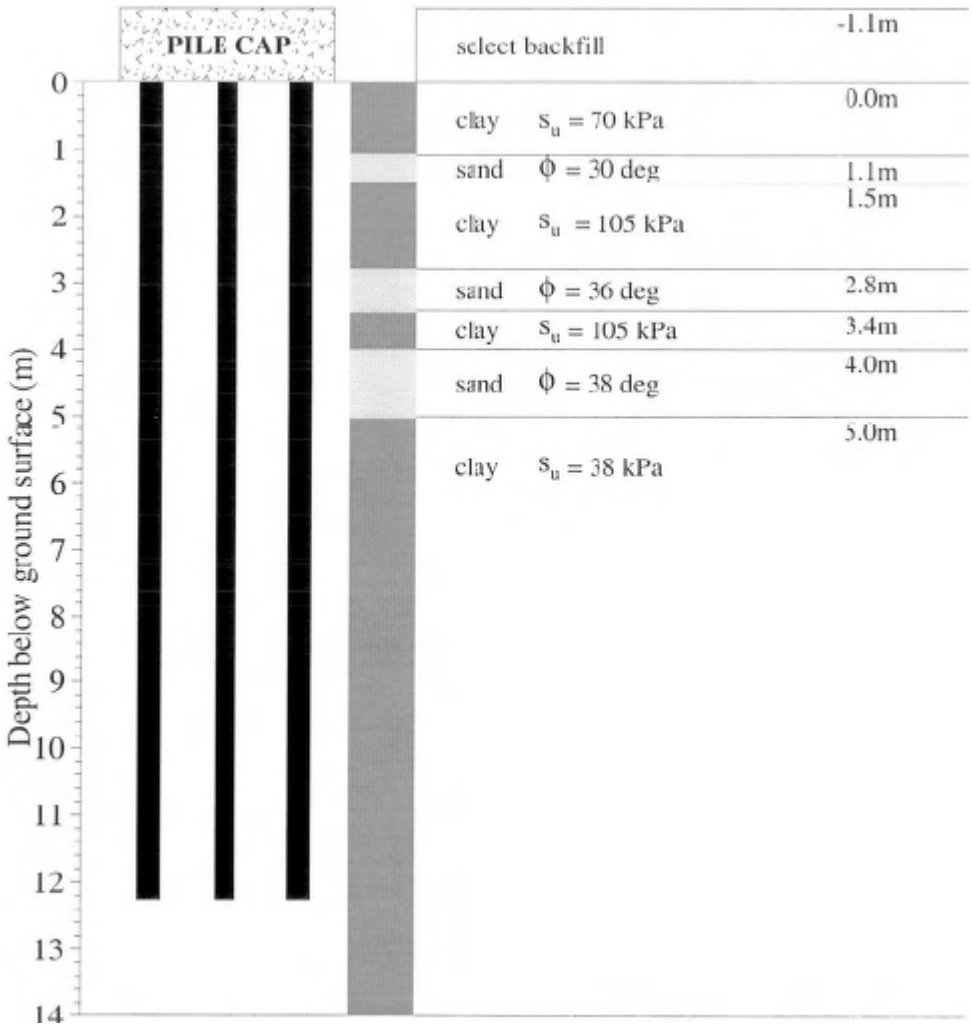

Figure 3.2: Idealized soil profile and strength properties

consisted of obtaining index properties such as natural moisture content, fines content, unit weights, Atterberg limits and soil classification. Consolidation and shear strength testing has also been performed.

The near-surface soils consist of clay, silt and sand deposited after the regressive phase of Lake Bonneville. Most of these surficial deposits were deposited during the Holocene to uppermost Pleistocene age, and during the last cycle of Lake Bonneville. The surficial deposits are underlain by lacustrine clay and silt of late Pleistocene age deposited by Lake Bonneville (Personius and Scott, 1992). In general, subsurface soils consist of approximately 5 m of moderately to highly plastic clays interbedded with medium dense silty sand layers, underlain by highly plastic, sensitive clays to a depth of 9.5 m. Deeper soils generally consist of alternating layers of silty sand and moderately plastic clay. An idealized soil profile developed by Cole showing basic soil types and shear strength parameters is shown in Figure 3.2.

3.4 LOOSE SILTY SAND BACKFILL PROPERTIES

A sieve test was conducted on a sample of the backfill soil and the grain-size distribution curve is shown in Figure 3.3. The grain-size distribution curve shows reasonable correlation with the curve for the same silty sand reported by Rollins and Cole (2005) which is also shown in Figure 3.3. Rollins and Cole also performed a hydrometer analysis to determine the percentage of silt and clay. According to their test, the silty sand consisted of 2.4% gravel, 52.9% sand, 44.7% fines, 38.5% silt, and 6.2% clay. The C_u and C_c values were determined to be 14.8 and 2.8. The sieve test conducted in this research suggests that the silty sand had 5.6% gravel, 53.6% sand, and 40.8% fines. A hydrometer test was not conducted to enable a better comparison in the silty and clay region. However, with the general agreement noted above the silty sand backfill classified as SM according to the Unified Soil Classification system (ASTM D 2487) and

A-4 according to the AASHTO M-145 system. Rollins and Cole (2005) found the optimum moisture content for silty sand tested at standard and modified proctor effort to be 16.8 and 13.6 percent, respectively. Also, they determined the maximum dry density to be 16.90 kN/m^3 (107.5 pcf) and 17.75 kN/m^3 (112.9 pcf) for standard and modified Proctor effort, respectively

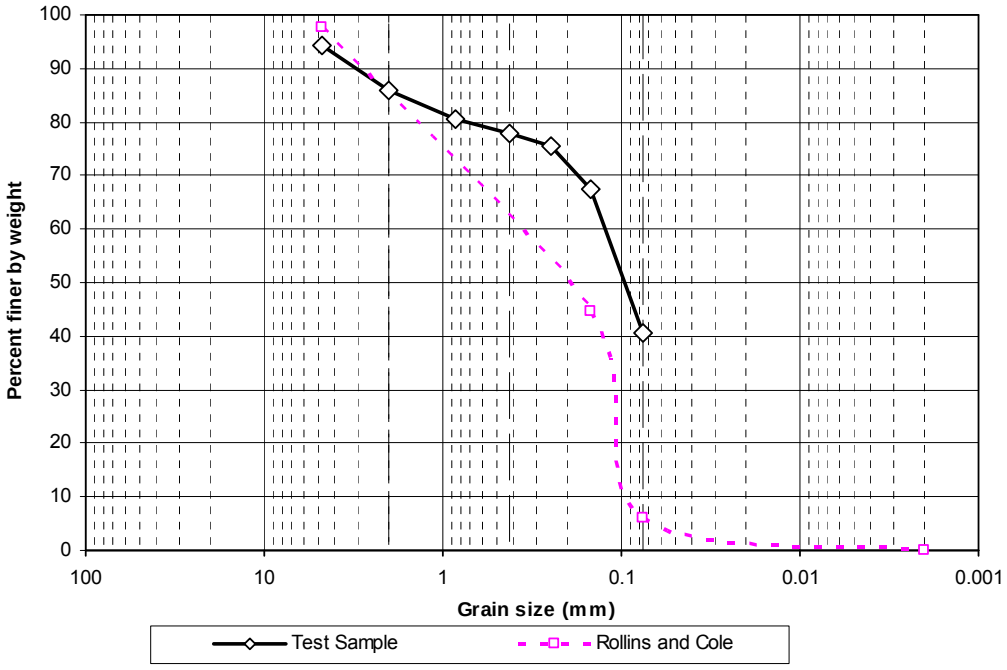

Figure 3.3: Average grain size distribution for backfill soil

The target unit weight for the backfill was 85-90 percent of the standard Proctor which corresponds to a density range of 14.37 kN/m^3 (91.46 pcf) to 15.21 kN/m^3 (96.84 pcf). A nuclear moisture-density gauge was used to test each 100 mm (4 in) -thick lift of the compacted fill during placement. A histogram of the measured density is shown in Figure 3.4. The average in-situ dry density from these tests was 15.69 kN/m^3 (99.9 pcf),

which is 92.8 percent of the standard Proctor maximum unit weight. This is slightly above the desired range.

Prof. James Bay, of Utah State University, performed SASW testing at the site after the backfill had been compacted into place. These tests indicated that the Rayleigh wave velocity for loose silty sand was 85.34 m/sec (280 ft/sec).

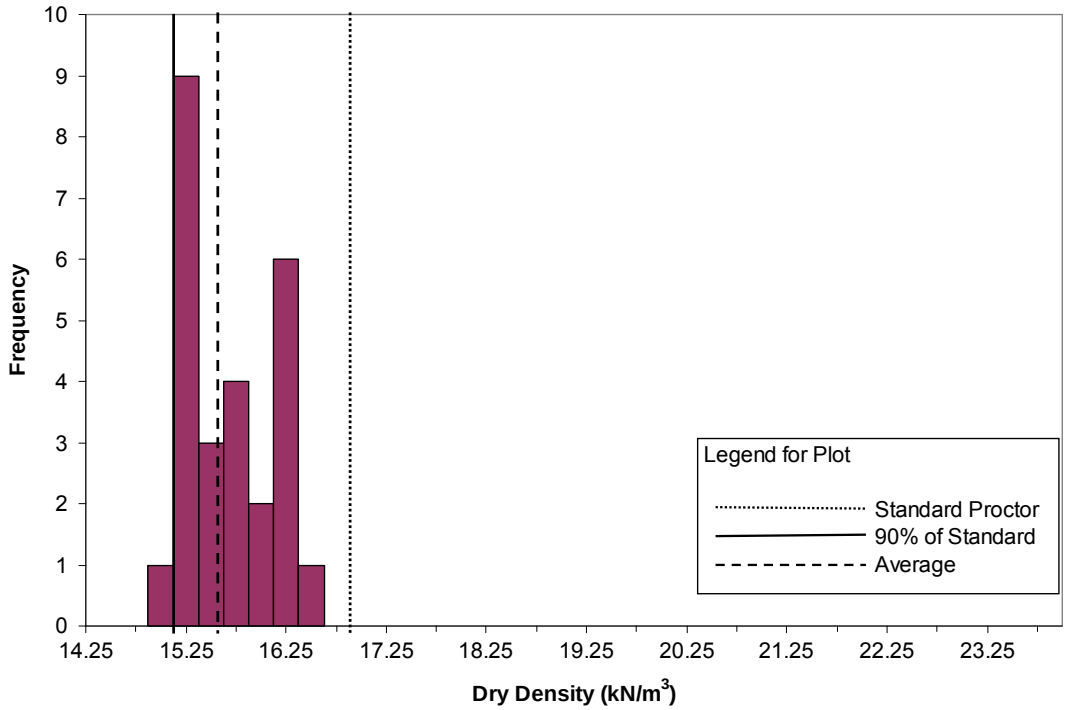

Figure 3.4: Histogram of unit weight testing of loose silty sand

Two in-place direct shear tests were conducted on site using a 0.46 m x 0.46 m x 0.23 m steel box into which a block of soil was trimmed. The first in-place direct shear test (Figure 3.5) produced cohesion (c) and friction angle (φ) values of 6.8 kPa and 28, respectively. The second test (Figure 3.6) produced cohesion (c) and friction angle (φ) values of 2.3 kPa and 29, respectively.

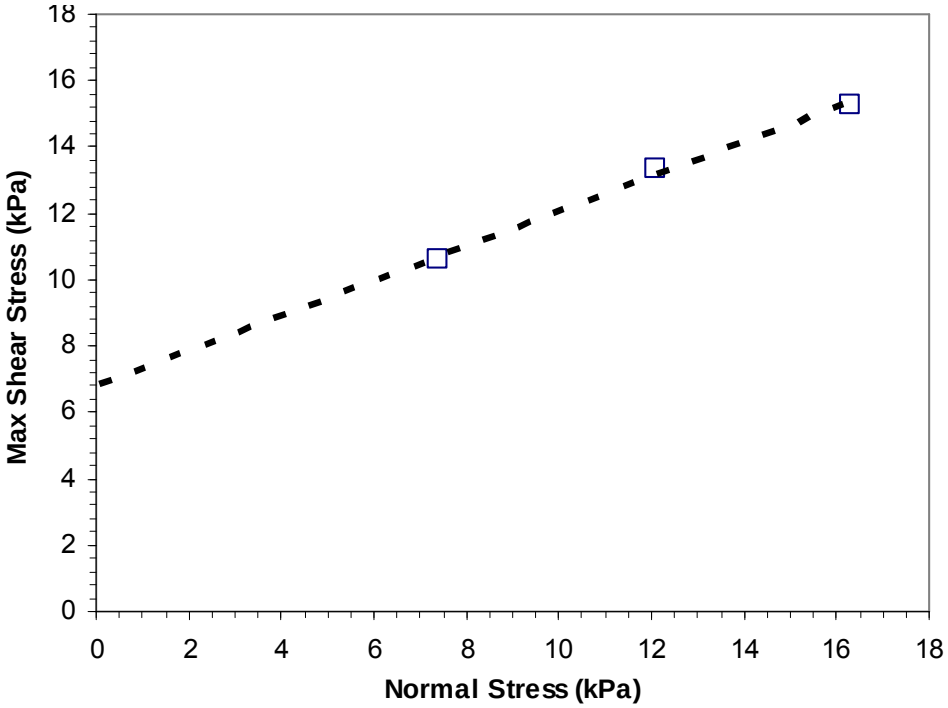

Figure 3.5: First in-place direct shear test max shear stress versus normal stress

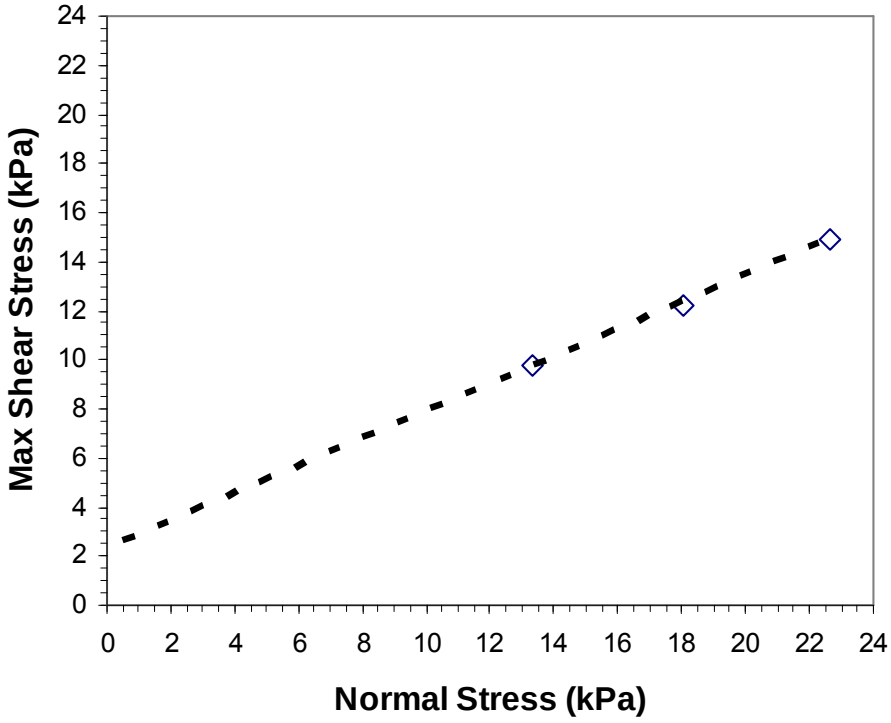

Figure 3.6: Second in-place direct shear test max shear stress versus normal stress

Lab direct shear testing was also conducted on the silty soil at density and moisture conditions corresponding to the field conditions. The samples were tested at the in-place moisture content in the lab at a density of 15.75 kN/m^3 (100.2 pcf) under drained conditions. The normal stresses used in the lab testing were higher than in-situ conditions due to the lower limit of the direct shear machine causing a constraint. Typical graphs of shear stress versus horizontal deflection, as well as shear stress versus normal stress are presented in Figure 3.7 and Figure 3.8. Values for cohesion (c) and friction angles (φ) were found to be 13.5 kPa (230.5 psf) and 27 degrees, respectively based on the tests conducted at the three lowest confining pressures.

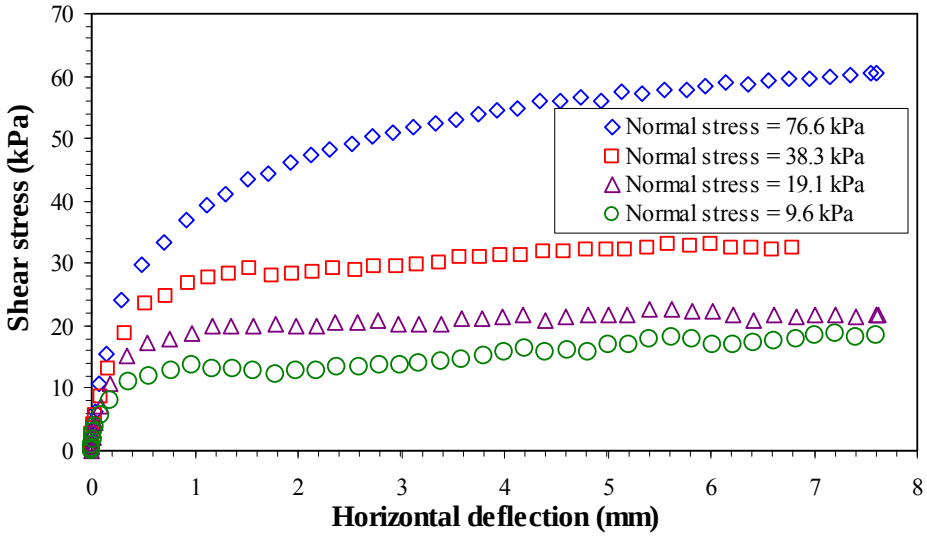

Figure 3.7: Shear stress versus deflection of loose silty sand

Two additional direct shear tests were conducted. A 40-60 silica sand in dry conditions was tested by itself to get general soil characteristic of the sand. After which, a portion of the tactile sensor and a concrete stone was placed in the machine to model and quantify interface characteristics. Normal stresses used for testing were 23.94, 47.88, and

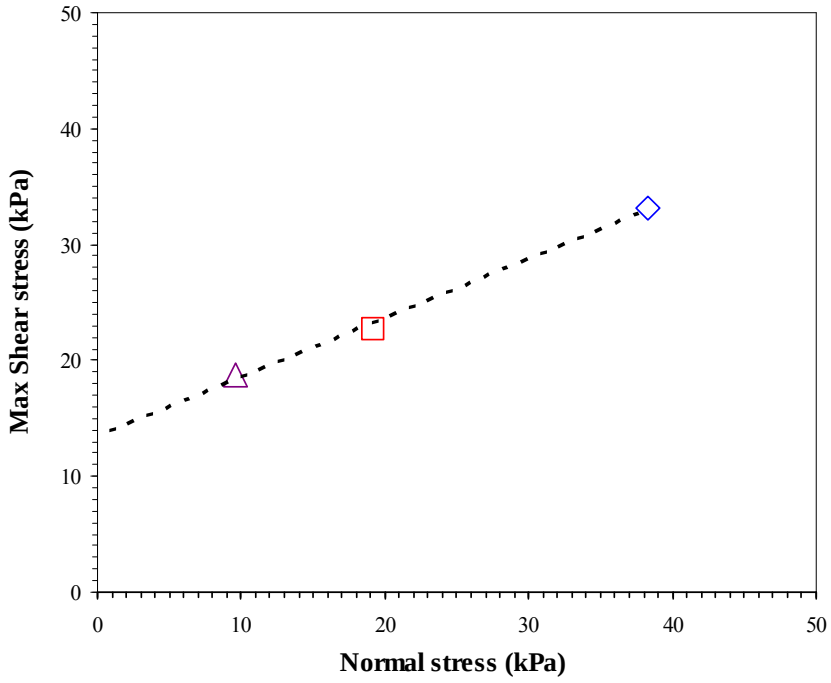

Figure 3.8: Maximum shear stress versus normal stress of loose silty sand

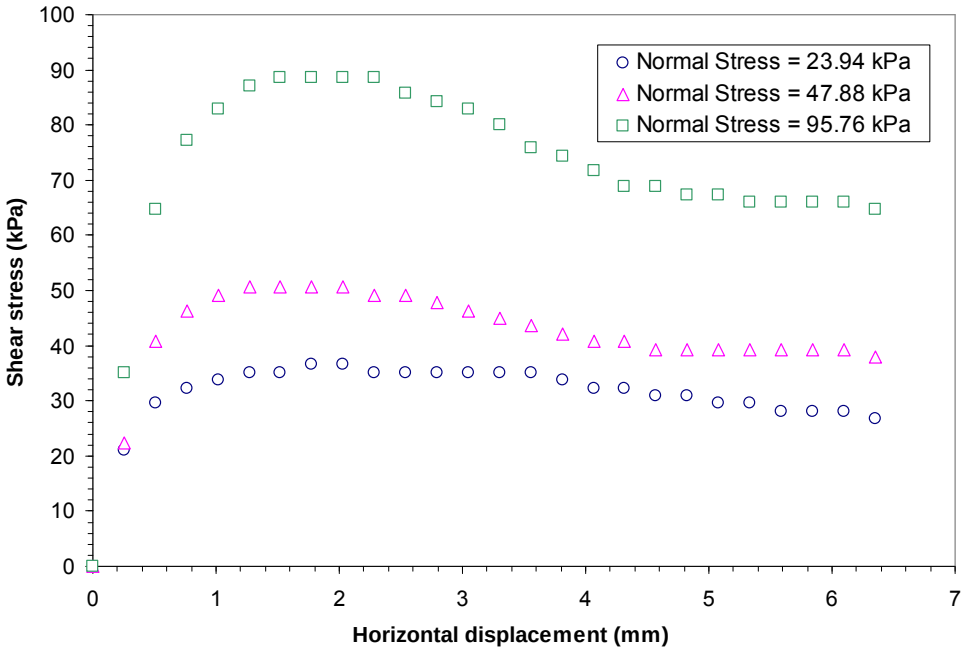

Figure 3.9: 40-60 silica sand shear stress versus deflection curves

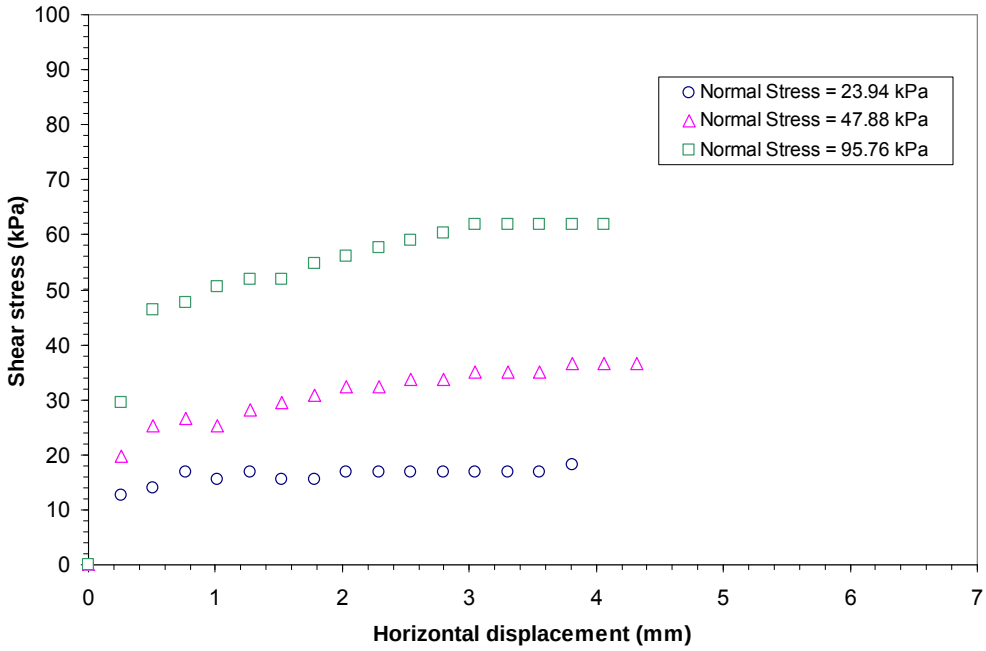

Figure 3.10: Sand-on-sensor shear stress versus deflection curves

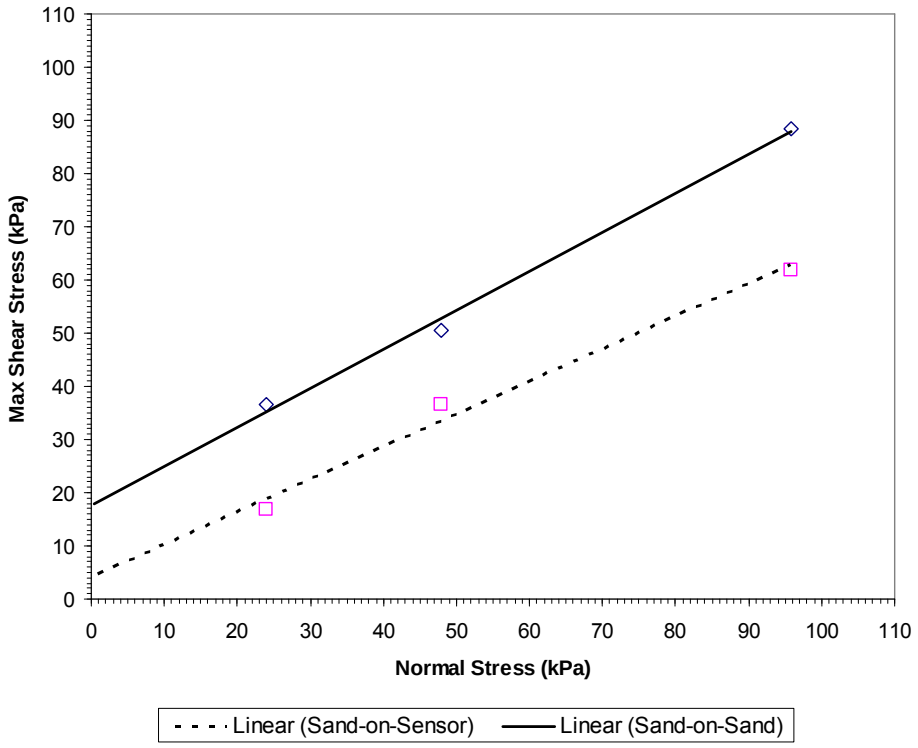

Figure 3.11: Combined normal stress versus shear stress curves

95.76 kPa (500, 1000, and 2000 lb/ft^2). The sand-on-sand samples were tested in the lab and values for cohesion (c) and friction angle (φ) were found to be 17.6 kPa (366.7 psf) and 36.3, respectively. The sand-on-tactile sensor was also tested at previously mentioned normal streses and the values for cohesion (c) and friction angle (φ) were found to be 4.2 kPa (88 psf) and 31.5, respectively. Typical graphs of shear stress versus horizontal deflection, as well as the combined (sand-on-sand and sand-on-sensor) shear stress versus normal stress presented in Figure 3.9, Figure 3.10, and Figure 3.11.

CHAPTER 4-TEST SETUP AND METHODOLOGY

4.1 INTRODUCTION

The full scale field testing described in this study involved static, cyclic, and dynamic lateral loading of a pile cap with and without backfill. As before mentioned, this site was used by Rollins and Cole (2006) and Cole (2003) of Brigham Young University. They had conducted a series of full scale tests to determine the ultimate passive pressure produced by various backfill soils and the development of this pressure with pile cap deflection. Those tests only involved static and slowly applied cyclic loadings. In this study, five full-scale lateral load tests were performed on the same pile cap with similar soils, namely: silty sand (dense and loosely compacted), gravel densely compacted with a 3 ft. compacted gravel zone and 6 ft compacted gravel zone with the loosely placed silty sand in the remainder of the backfilled area, and finally a no backfill case to isolate the pile contributions to stiffness and damping and thereby isolating the backfill passive earth resistance, stiffness, and damping characteristics. However, these tests were performed dynamically or with rapidly applied cyclic loads. This makes it possible to evaluate the dynamic stiffness and damping produced during dynamic loading. The load tests were performed between the dates of August 15, 2005 and August 26, 2005. This report will focus on the test results of the silty sand compacted loosely and the no backfill (baseline)

case. This section will cover the equipment used and the test setup. This section will also summarize the backfill soil characteristics of the soil under consideration (loose silty sand) and testing procedures used throughout the tests.

4.1.1 GENERAL

Figure 4.1 shows the main elements of the load testing program, each of which is discussed in more detail in the following text.

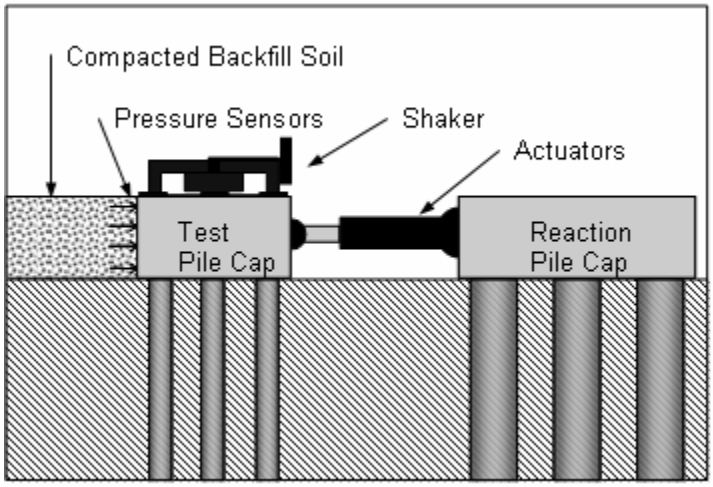

Figure 4.1: Schematic showing main components used in the testing program

4.1.2 TEST PILE CAP DESCRIPTION

The pile cap used for this research is the same used by Rollins and Cole, but retrofitted to accommodate two hydraulic actuators and an eccentric mass shaker. The cap is 1.12 m (3.67 ft) high with a width of 5.18 m (17 ft) and a depth of 3.05 m (10 ft). The pile cap connects 12 steel pipes installed in a 4 x 3 configuration. The piles are 324 mm (12.76 in) outside diameter, 9.5 mm thick wall, and spaced center-to-center at 4.4

and 3.3 pile-diameters in the long and short dimensions, respectively. The steel pipe piles are ASTM A252, Grade 3 (i.e., 310 MPa minimum yield strength); however, manufacturer mill certifications for 192 specimens of this type of pipe pile had average yield strength of 404.6 MPa based on a 0.2% offset criteria. The piles extend to a depth of approximately 12.2 m (40.03 ft) and are filled with concrete. The steel pile sections are embedded approximately 75 mm into the concrete cap. There is also a circular reinforcing cage consisting of six #25 vertical bars and a #13 spiral at a 305 mm pitch which extends approximately 1.7 m into each pile and 1.06 m into the cap.

4.1.3 REACTION PILE CAP DESCRIPTION

Adjacent to the test pile cap is a reaction pile cap constructed approximately 3.84 m north of the existing test pile cap. The existing piles shown to the north of the test cap in Figure 3.1 had to be extracted and reinstalled somewhat to the north using a vibratory hammer so that they would be where needed for the reaction cap. The reaction pile cap is 1.12 m tall and 5.19 x 5.33 m in plan view (with the short direction corresponding to the north and south faces, matching the test cap). The cap connects nine steel pipe piles installed in a 3 x 3 configuration with 3 pile-diameter center-to-center spacing. The steel pipe piles have a diameter of 610 mm (24.02 in) with a wall thickness of 12.7 mm (same grade as the test piles), and a depth of approximately 12.2 m (40.03 ft) with the uppermost 2.7 m containing reinforced concrete and the remainder filled with soil. The steel pile sections are embedded approximately 75 mm into the concrete cap. There is also a circular reinforcing cage consisting of eight #32 vertical bars and a #13 spiral at a 152 mm pitch which extends approximately 2.74 m into each pile and 1.0 m into the cap.

4.1.4 HYDRAULIC ACTUATORS

The test pile cap and reaction cap were connected by two hydraulic load actuators installed in parallel. Each actuator (manufactured by MTS Corporation) has a load capacity of 2.7 and 2.0 MN in compression and tension, respectively, and has a stroke of ±508 mm and a maximum travel velocity of approximately 100 mm/sec while maintaining a constant rate of loading or displacement during the test period. The ends of the actuators are equipped with swiveling heads, creating a moment-free pinned connection. The two actuators were connected at mid-height of the test pile cap and reaction pile cap with four high-strength, threaded steel rods, installed in sleeves which extended the full length of the pile caps. The actuators were used to slowly push the test pile cap to predetermined displacement levels. The actuators were unable (and not intended) to apply a rapid cyclic loading due to the high levels of load required to initially displace the pile cap.

4.1.5 ECCENTRIC MASS SHAKER

The George E. Brown, Jr. Network for Earthquake Engineering Simulation (NEES) provided an eccentric mass shaker from the University of California Los Angeles equipment site. The shaker (model MK-15 manufactured by ANCO Engineers) was mounted on top of the existing pile cap and anchored with chemically bonded steel anchors embedded in the pile cap. The eccentric mass shaker was used to create a cyclic, dynamic loading superimposed on the static loading provided by the actuators. The shaker has uni-directional force and frequency capacities of 445 kN and 25 Hz (but not at

the same time). Due to safety concerns (potential loosening of the anchors), the shaker was operated during testing at levels not exceeding approximately 356 kN.

The force-frequency relationship for the shaker is controlled by the eccentricity provided by the configuration of its four baskets and their internal brick payloads. The equation relating force and frequency is given by Equation 4.1:

$$Force = u * 0.102 * (WR) * \omega^2 / 1000 \quad \textbf{(4.1)}$$

where force is expressed in kips, u is the loop amplitude in inches, and ω is frequency in hertz, and WR is the total eccentricity of the weight and basket per basket in lb-in. During testing of the loose silty, only one basket configuration was used and the WR value was equal to 6127 lb-in (692.2 kN-mm). During the no-backfill (baseline) testing, two different basket configurations were used in an attempt to bracket the changing fundamental frequency. (Due to logistical constraints it was not possible to fully bracket the changing fundamental frequency of the pile-cap system with the loose silty sand backfill). The first configuration involved two partially loaded baskets with a WR value of 6127 lb-in (692.2 kN-mm) each, resulting in maximum safe operating frequency of 8 Hz. This configuration was used for the first four static displacement levels. At higher displacement levels, a second configuration involving two partially loaded baskets with an eccentricity of 3984 lb-in (450.1 kN-mm) each was used, resulting in maximum safe operating frequency of 10 Hz.

4.1.6 INSTRUMENTATION

Load and displacement were measured throughout the tests. Eight linear variable differential transducers (LVDT) were used to directly measure the displacement of the pile cap and reaction foundation as the actuator applied load. Accelerometers were mounted on the pile cap to compute relative displacement of the pile cap as it was shaken.

Load was measured directly by strain-gauge load cells built into the actuators. Pressure at the soil cap-interface was measured using four earth pressure cells and two thin-film tactile pressure sensors manufactured by Tekscan, Inc. The earth pressure cells were mounted flush on the side of the pile cap. This was accomplished by chiseling about 292 mm diameter circles in the pile cap, and then resurfacing the roughened surface with cement grout. A water seal was then applied to the cement grout. A vertical groove was cut from the pressure cell to the top of the cap to accommodate the handles and wiring of the pressure cells. To further protect the pressure cells a small steel pipe was cut in half lengthwise and placed over the handles of the pressure cells. After this manner, the four earth pressure cells were mounted flush with the face of the pile cap.

The tactile pressure sensors measured pressures on a grid of approximately 10.2 mm spacing over a 530 mm wide and 490 mm high area. The sensors were made of polyester sheets embedded with semi-conductive material. Horizontal and vertical sensing elements intersect at “sensels”. The change in the resistance over each sensel determines the pressure acting on the sensor. Each tactile pressure sensor used in this testing contained 2016 sensels. An electronic handle was attached to each tactile sensor and was used to transfer data from the sensing pad to a laptop or computer for data

acquisition using software provided by Tekscan called “I-scan”. The sensors were equilibrated and calibrated in a lab before being used in the field using a pneumatic bladder system. The equilibration and calibration should be conducted using material that will be in contact with the tactile pressure sensor during field tests; however, experiments were conducted with concrete surfaces and fine to medium grade sand. These experiments found that equilibration and calibration could be reasonable accomplished using the bladder system.

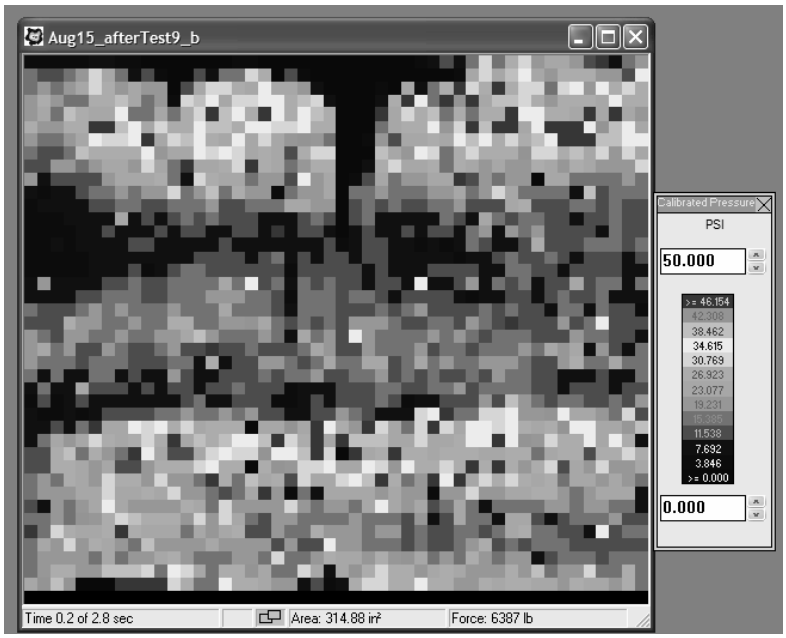

Figure 4.2: Sample tekscan real time window

The tactile pressure sensors were evenly spaced vertically along the height of the pile cap. To protect the lower tactile pressure sensor’s handle a square hole was cut into the face of the pile cap, the handle was then attached to the tactile pressure sensors and placed in the cut, and finally the cut was covered by a steel plate. Small holes were punctured along the outer edges of the tactile pressure sensors to allow entrapped air to

escape during backfilling. The data acquisition software allows the pressures to be viewed along the sensor in real-time. A sample real-time window is shown in Figure 4.2. The figure shows the reading from the tactile pressure sensors immediately after the shaker run at 50 mm. Each small square in the figure represents a sensel on the tactile pressure sensor. Due to the grey scale format of the figure some resolution in color was lost.

The field data was recorded using the NEES mobile field station, and a laptop was used to collect data from the tactile pressure sensors. The NEES mobile station recorded data at 0.005 Hz, and the laptop recording the tactile pressure sensors recorded data at 0.01 Hz. Figure 4.4 shows the general setup of the instrumentation. Instrumentation locations are summarized in Appendix A.

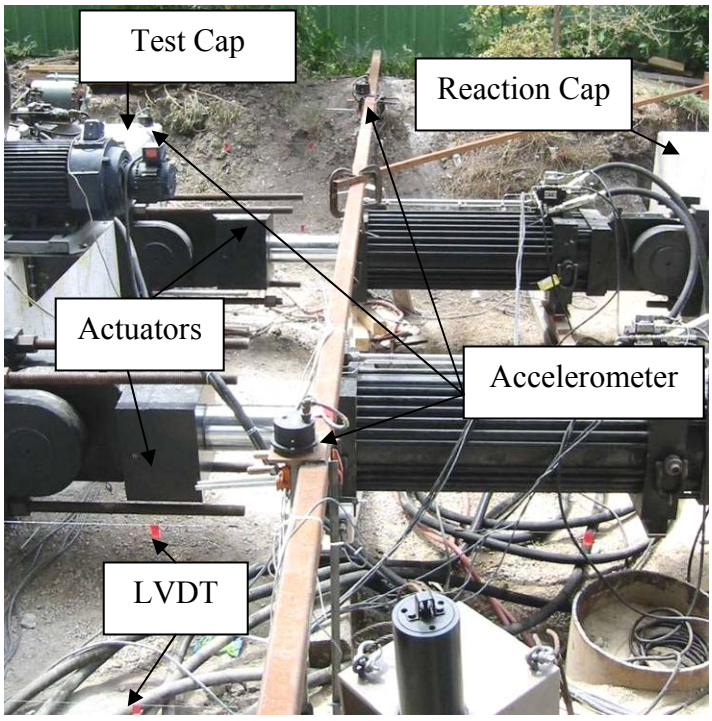

Figure 4.3: Equipment setup between test cap and reaction cap

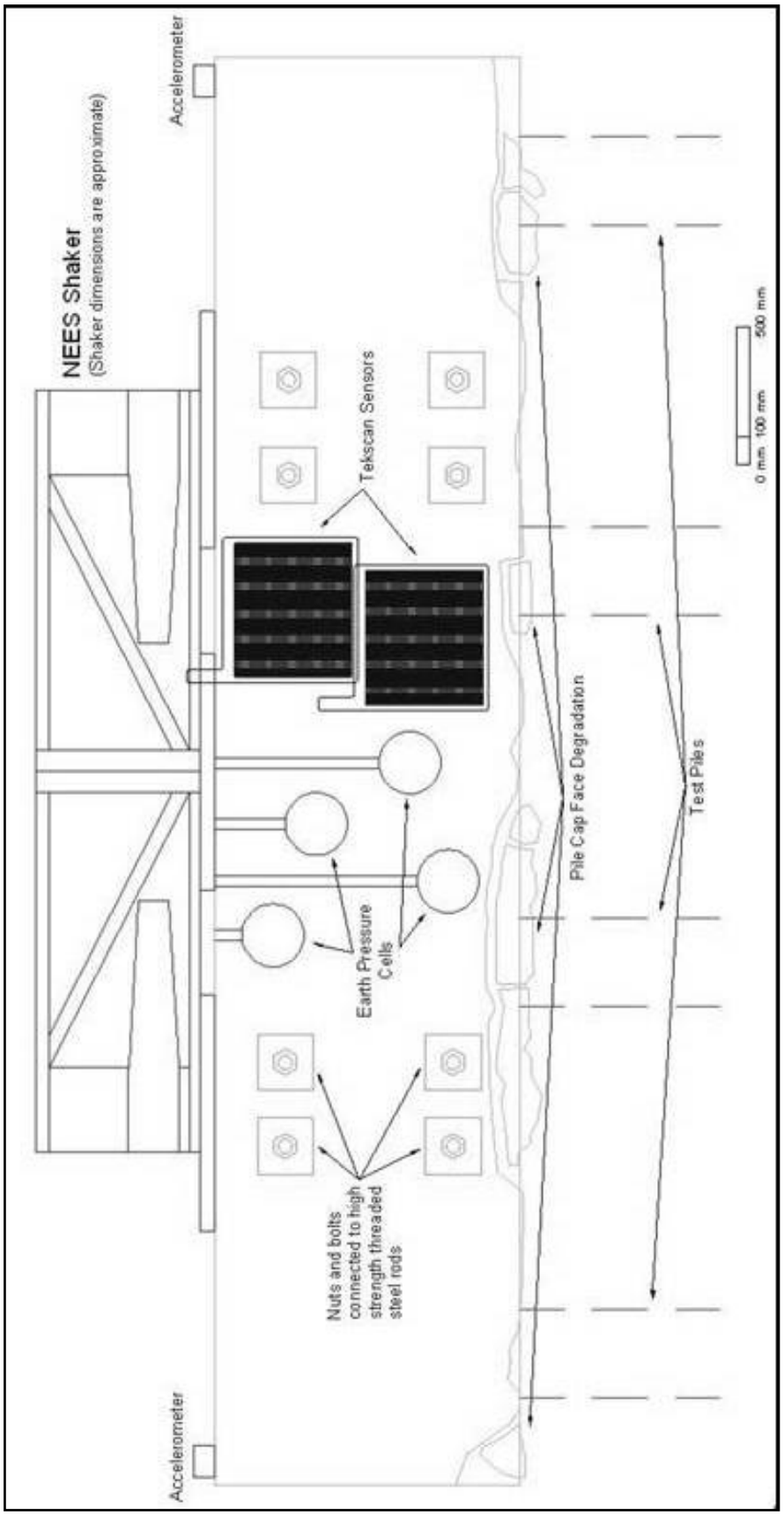

Figure 4.4: Pile cap face with instrumentation

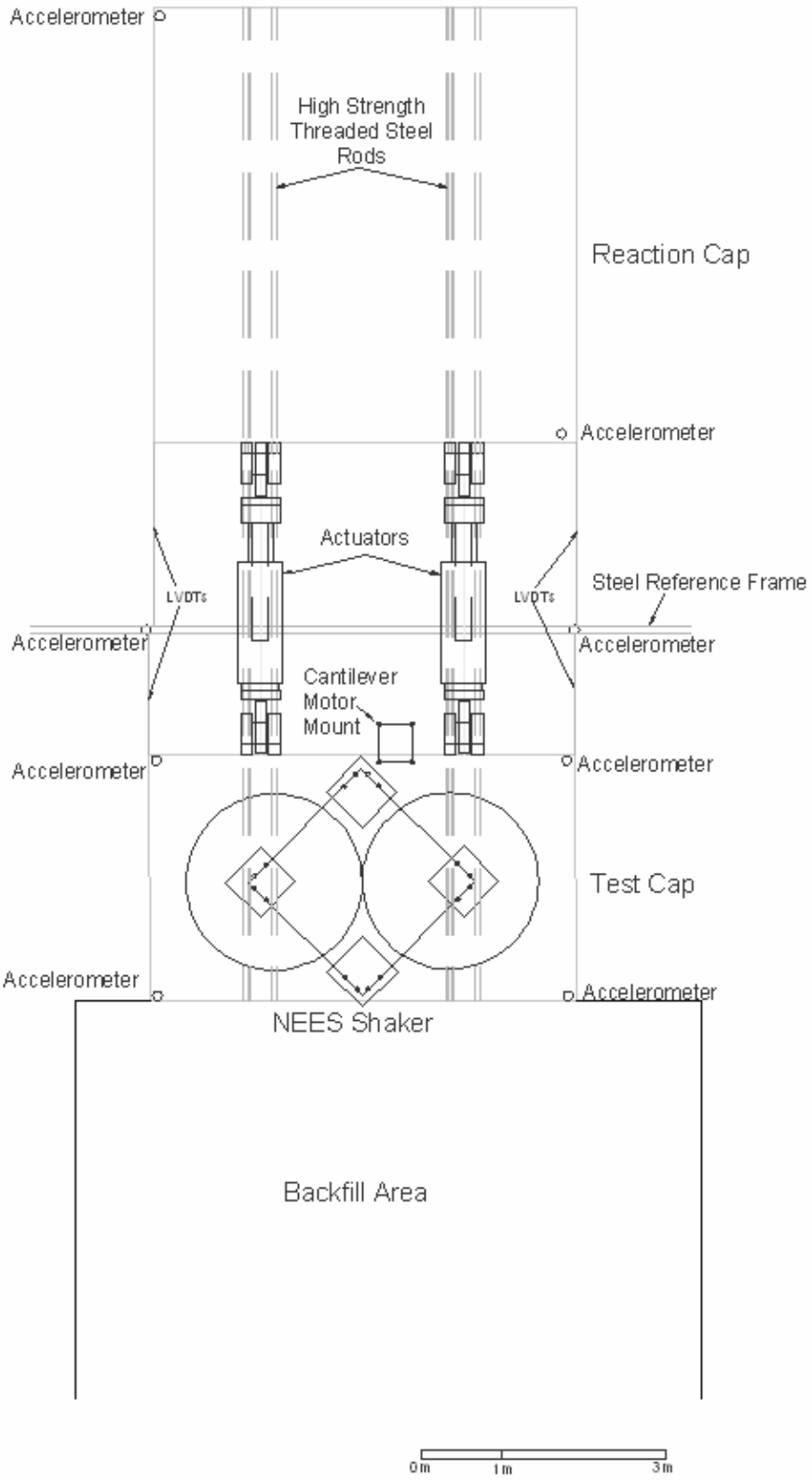

Figure 4.5: Plan View of testing facility

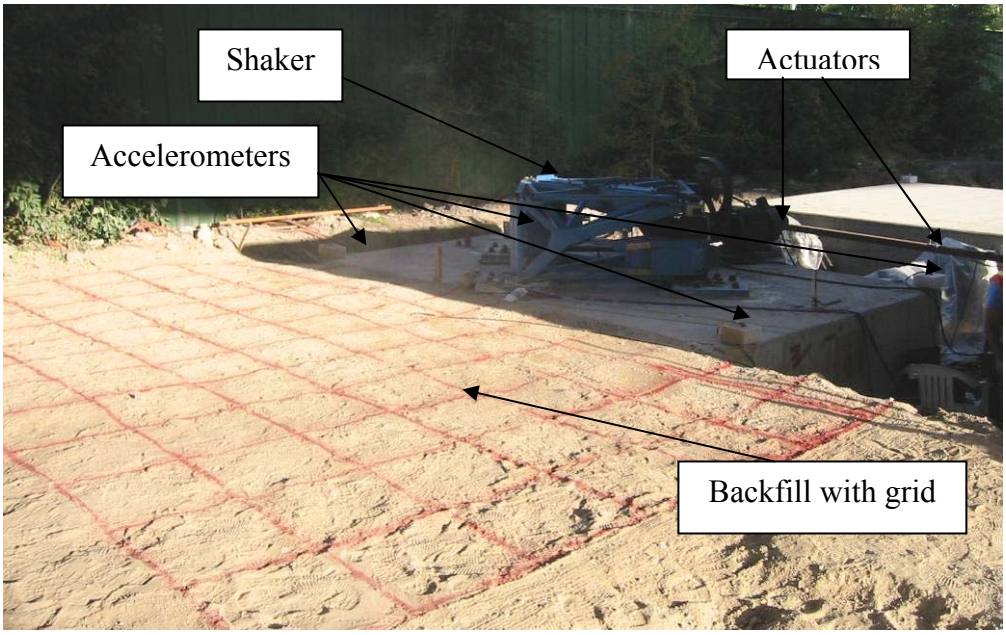

Figure 4.6: Test setup in front of test cap

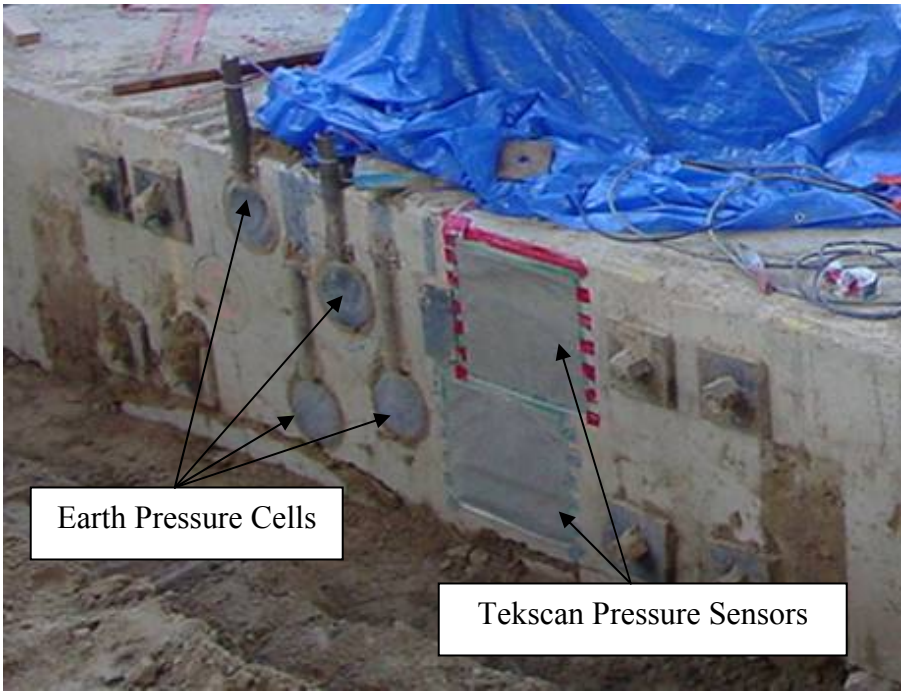

Figure 4.7: Instrumentation setup on front of pile cap before backfill

The backfill was placed along the longer side of the pile cap and extended beyond each side of the side of the pile cap to capture three-dimensional effects. Backfill placement extended approximately 4.9 m (16 ft) behind the cap in order to ensure that the resulting log-spiral failure surface occurred within the limits of the backfill. A grid was painted on top of the backfill for crack mapping purposes. Figure 4.4 and Figure 4.5 show drawings of the cap face and plan view of the site, respectively. Figure 4.3, Figure 4.6, and Figure 4.7 show photos taken of the actuators, backfill area, and pile cap instrumentation, respectively.

4.2 TESTING PROCEDURE

Following instrumentation setup the front face of the test pile cap was backfilled with loose silty-sand material. Throughout the backfill operation, a total of six accelerometers were placed in the backfill material at specified locations. Upon completion of the backfill, data samples were taken from the Tekscan sensors to get an initial at-rest passive pressure on the pile cap. Backfilling normally took a full day for completion, and testing continued the following day.

The testing began with the shaker being ramped up from 1 Hz to about 8 Hz without any load from the actuators. This beginning shaker test was considered the first test. After the shaker run, the actuators pushed the cap to a target deflection of 6.35 mm (0.25 in), and then the shaker was ramped again to a frequency of about 8 Hz. This test was considered test two. The actuators then pushed the cap to a target deflection of 12.7 mm (0.50 in). The sequence of an actuator push followed by a run of the shaker

constituted a test. Each actuator push increased the pile cap deflection by about 6.35 mm (0.25 in) referring to Table 4.1, the testing sequence is shown.

Table 4.1: Test History for August 18, 2005 for loose silty sand

Test	Target Deflection (mm)	Actual Deflection (mm)	Maximum Frequency (Hz)	Length of Test (min:sec)
1	0	0	8	7:12
2	6.35	6.34	8	6:31
3	12.7	12.65	8	6:21
4	19.05	19.03	8	6:17
5	25.4	25.31	8	6:29
6	31.75	31.57	8	6:56
7	38.1	37.90	8	6:30
8	44.45	44.21	8	6:43

Table 4.2: Test history for August 16, 2005 for baseline pile system testing

Test	Target Deflection (mm)	Actual Deflection (mm)	Maximum Frequency (Hz)	Length of Test (min:sec)
1	0	1.27	7.5	04:22
2	6.35	4.88	8	05:01
3	12.7	10.66	8	07:31
4	19.05	17.04	8	05:31
5	25.4	23.32	9.5	05:23
6	31.75	29.58	9.5	05:03
7	38.1	35.91	9.5	06:04
8	44.45	42.22	9.5	07:09
9	50.8	49.48	9.5	05:56

The baseline pile testing will be subtracted from the loose silty sand data to isolate the passive earth resistance. For this reason, and for future reference a summary of the testing performed for the baseline pile will be included here. The testing procedure for the baseline case is the same. The only thing that changes is that the frequency range tested started at 1 Hz to 10 Hz. However, some test varied in regards to frequency ranges

tested and only the data falling into the range of 1 Hz to 9.5 Hz was included in the processing of figures presented in chapters five and six (see Table 4.2).

CHAPTER 5-STATIC RESPONSE OF LOOSE SILTY SAND

5.1 INTRODUCTION

This chapter will present and discuss the static response of the loose silty sand backfill testing. System (pile cap plus backfill) load-deflection curves will be presented and compared for three cases. The first case is the maximum load-deflection curve defined by connecting the peak load and deflection points for each increment of loading. The second case is the relaxation load-deflection curve obtained by connecting the load and deflection points at each load increment immediately prior to cyclic loading. The third case is the post-cyclic load-deflection curve which is defined by connecting the load and deflection points at each load increment immediately after the completion of cyclic loading. These three curves will be plotted and compared relative to the baseline load-deflection curves provided by the pile cap without any backfill. Finally, the baseline curves will be subtracted from each of the appropriate loose silty sand curves (maximum, relaxation, and post-cyclic) to reflect the passive earth resistance contribution to each of these load-deflection curves.

5.2 LOAD-DEFLECTION CURVES

The loose silty sand test was recorded from start to finish and produced raw load-deflection curves representing the system resistance response. The pile cap was also tested without backfill to quantify the pile contribution and create a baseline load-deflection curve. Passive soil resistance was isolated by subtracting the lateral resistance contributed by the piles from the total system resistance. Using actuator load data versus linear variable differential transducer (LVDT) data load-deflection curves were produced and compared.

5.2.1 LOOSE SILTY SAND BACKFILL SYSTEM RESISTANCE

The data collected from the actuator and LVDT were plotted to produce load deflection curves. Using the initial starting point of the record for that day allowed the deflections to be zeroed and plotted as shown in Figure 5.1. The lateral load testing was typically performed in an incremental fashion using the following procedure. First, the two actuators pushed the pile cap to a specified deflection point then natural creep of the soil occurred before cyclic testing with the shakers took place. After the cyclic loading sequence produced by the shakers, which will be discussed in Chapter 6, additional relaxation of the load occurred and the post-cyclic load-deflection point was defined. The actuators were then used to increase the load to the next deflection increment and the procedure was repeated until the next target deflection was achieved. Target deflections were 6.35, 12.7, 19.05, 25.4, 31.75, 38.1, 44.45, and 50.8 mm. Prior to beginning the entire testing series, a set of cyclic lateral load tests were performed with the eccentric mass shaker.

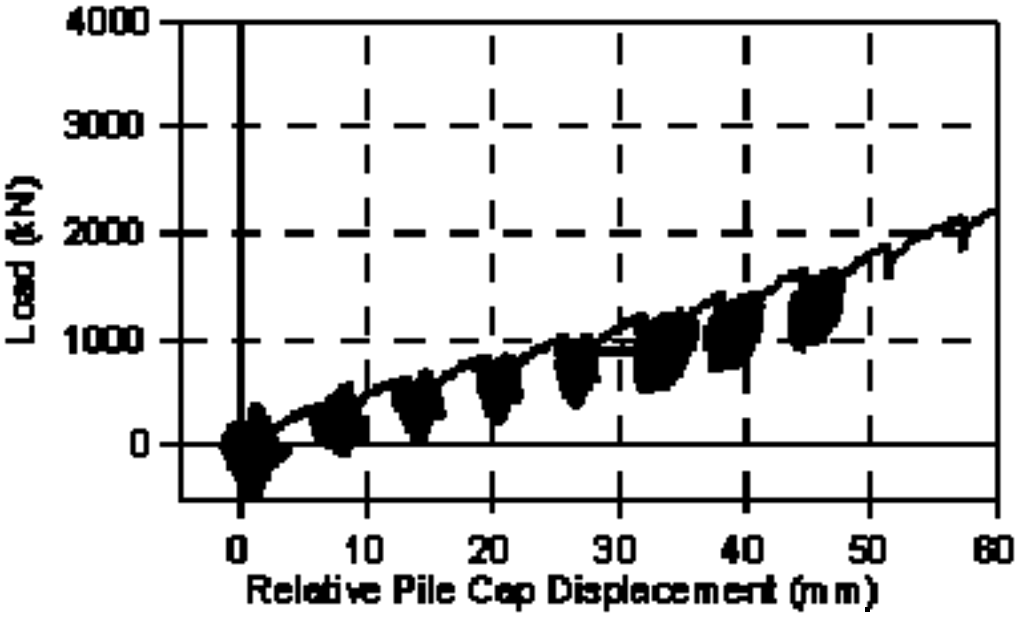

Figure 5.1: The load-displacement response of the pile cap with loose silty sand backfill

The actuator push, creep (relaxation point), and post-cycling point constitute the static portion of the testing. The dynamic shaker testing that occurred between the relaxation point and the post-cycling point will be considered later. Collecting the maximum loads at the end of each push with its associated zeroed displacement produced a maximum load-deflection curve as shown in Figure 5.2. The relaxation and post-cycling load-deflection curves are also plotted in Figure 5.2. The relaxation load-deflection curve refers to the collection of load-deflection points following creep in the soil after the push to the target deflection was completed but just before the eccentric shaker tests were begun. Although actuator deflection load was held constant, dissipation of the soil response following the initial push is represented by the relaxation load-deflection curve.

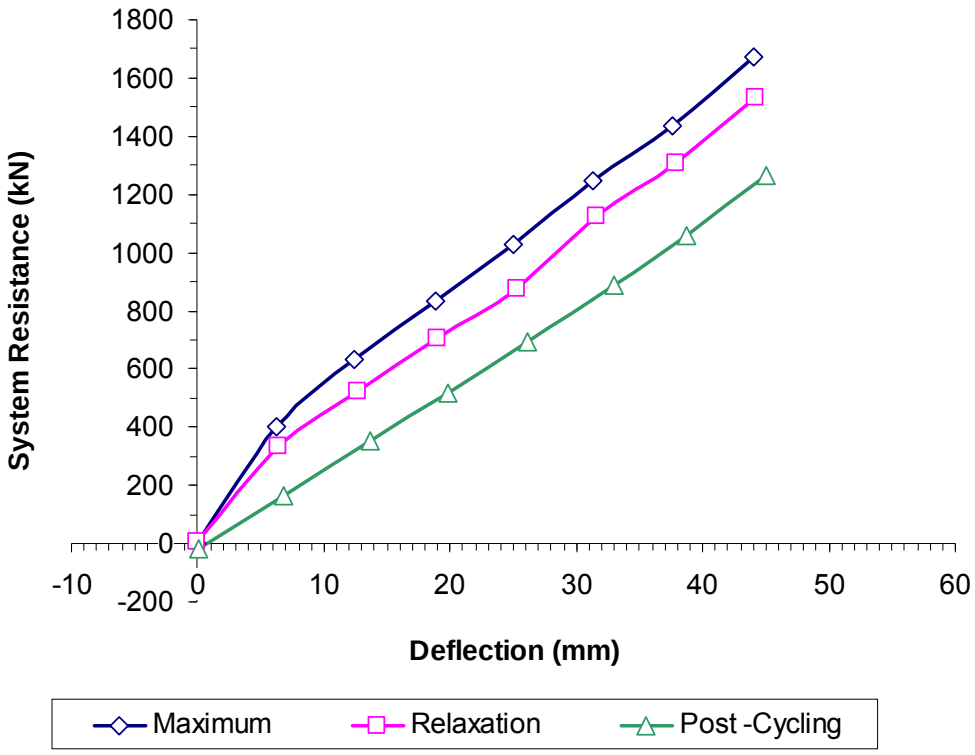

Figure 5.2: System load-deflection curves

The load-deflection plots in Figure 5.2 include the loose silty sand passive resistance and the pile/pile cap resistance, thus constituting the total system resistance. The maximum load-deflection curve exhibits the greatest degree of non-linear behavior, but the relaxation curve and the post-cycling load-deflection curves become progressively more linear. In fact, for deflections greater than about 10 mm, all three curves appear to exhibit very linear behavior. The percent degradation expressed by the difference of the relaxation and maximum load normalized by the maximum load decreased range from ~20% at low deflection levels to ~8% at high deflection levels. This is approximately a median load degradation of 124 kN. The percent degradation expressed by the difference of the post-cycling and maximum load normalized by the maximum load decreased from

~60% at low deflections to ~20% at high deflections. This is approximately a median load degradation of 334 kN.

5.2.2 BASELINE PILE RESISTANCE

To enable the isolation of the passive resistance provided by the loose silty sand, the pile cap resistance was obtained by shaking and pushing the pile cap with no backfill in place. The same loading procedure was used for this test to facilitate comparisons. Data from actuators and LVDTs were graphed and a load-deflection curve for the full test is presented in Figure 5.3. The stiffness represented in the graph is approximately 27 kN/mm (155 kip/in).

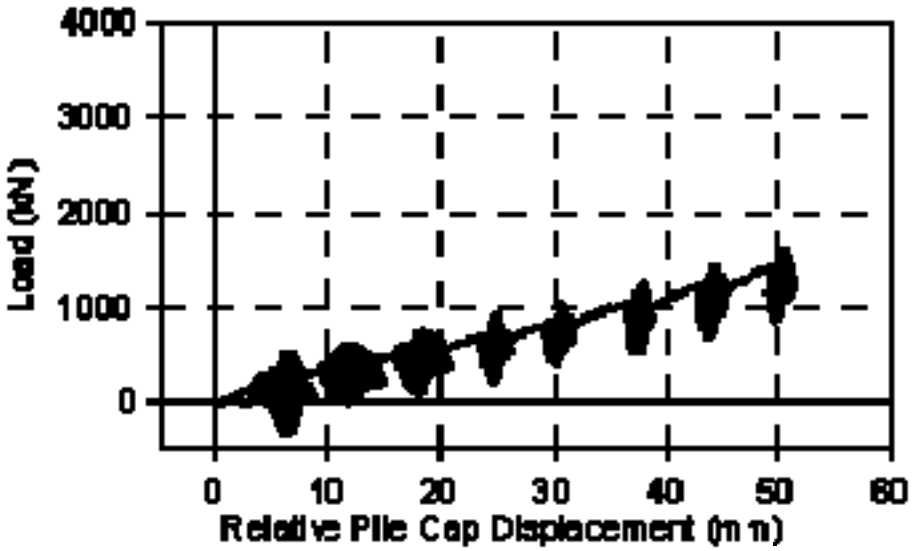

Figure 5.3: The load-displacement response of the pile cap with no backfil

To verify that the baseline load-deflection curve for the no backfill test remained consistent throughout subsequent backfill testing, comparisons were made with the load-

deflection curves obtained when the pile cap was pulled-back to its initial position at the end of each test day. Although the load-deflection curve during pull-back was not recorded at the end of the loose silty sand testing, the pullback curves from tests before and after this test suggest that the stiffness deduced from the other tests held constant throughout the testing week. Because a gap formed between the pile cap and the backfill soil during pull-back, the pull-back curves should indicate the lateral contribution due to the pile cap only particularly at small displacements. Figure 5.4 shows load-deflection curves during pull-backs recorded following the backfill tests involving dense silty sand backfill and a 3 ft gravel backfill between the pile cap and the loose silty sand. Also shown in the figure is the load-deflection curve produced by the actuator pushing the pile cap during the test with no backfill.

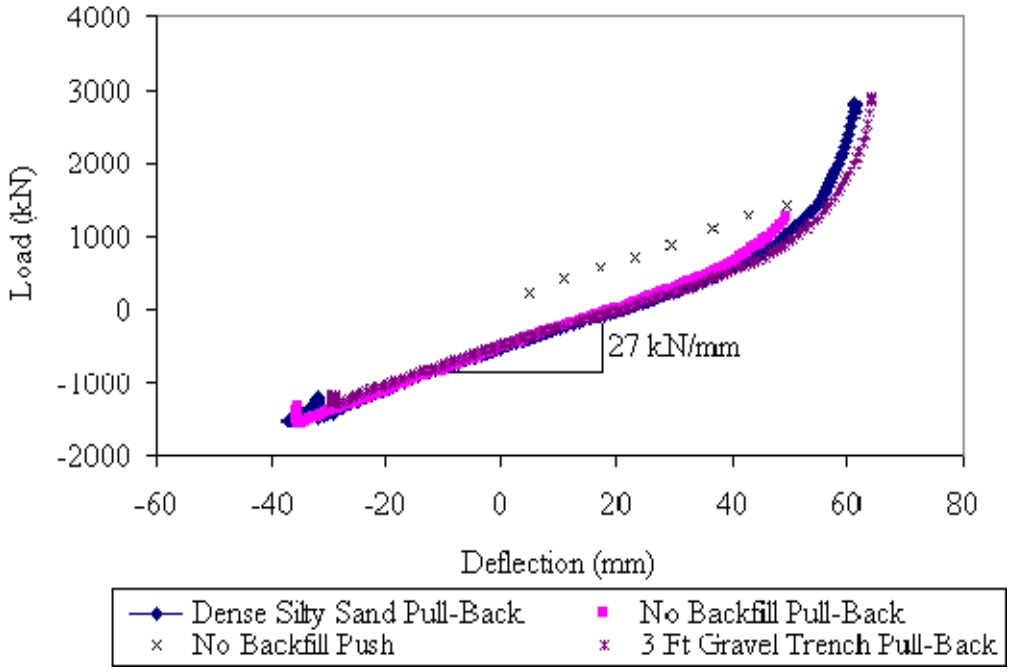

Figure 5.4: Pull backs and pile only push during testing

The beginning of the pull-back curve is at a deflection 2 to 2.5 in. The beginning of the pull-back curve is characterized by a steep concave upward shape to the load-deflection relationship. The pull-back load-deflection curve gradually changes from a curve into an approximately linear relationship. The curved portion of the load-deflection curve during pull-back can be attributed to the passive resistance of the backfill which is still in contact with the pile cap and is contributing to the overall passive resistance in this region. As the slope of the load-deflection curve becomes linear, the pile cap loses contact with the backfill soil and most of the lateral resistance is provided by the pile cap only. As shown in Figure 5.4, the slope of the load-deflection curve with no backfill during pushing is similar to the slope of the linear portion of the load-deflection relationships during pull-backs further verifying the accuracy of the baseline slope for the piles.

Reducing recorded data consistent with the method applied to the loose silty sand data allowed for the maximum, relaxation, and post-cycling load-deflection curves also to be extracted and produced as shown in Figure 5.5. A comparison between the maximum load-deflection curve for the total system and the pile cap (baseline) static, maximum resistance curve indicates that the pile cap accounts for ~78% of the total system resistance over a wide range of deflections.

The load-deflection curves in Figure 5.5 quantify the contribution of the pile cap to lateral resistance. The percent degradation expressed by the difference between the relaxation and maximum load normalized by the maximum load ranged from about ~20% at small deflection to ~7% at larger deflections. The loose silty sand backfill tests yielded approximately the same percent degradations when comparing the relaxation and

maximum load curves; however, with a larger median load degradation of 124 kN compared to a median load degradation of 87 kN for the no backfill case. The percent degradation expressed by the difference of the post-cycling and maximum load normalized by the maximum load resulted in a range from about ~60% at small deflection to ~15% at large deflection; also similar for the loose silty sand case. This is approximately a median load degradation of 169 kN (334 kN for the loose silty sand case). The median load degradation for the backfill case are larger than the no backfill case because the total load in the system is higher due to the added resistance provided by the loose silty sand backfill.

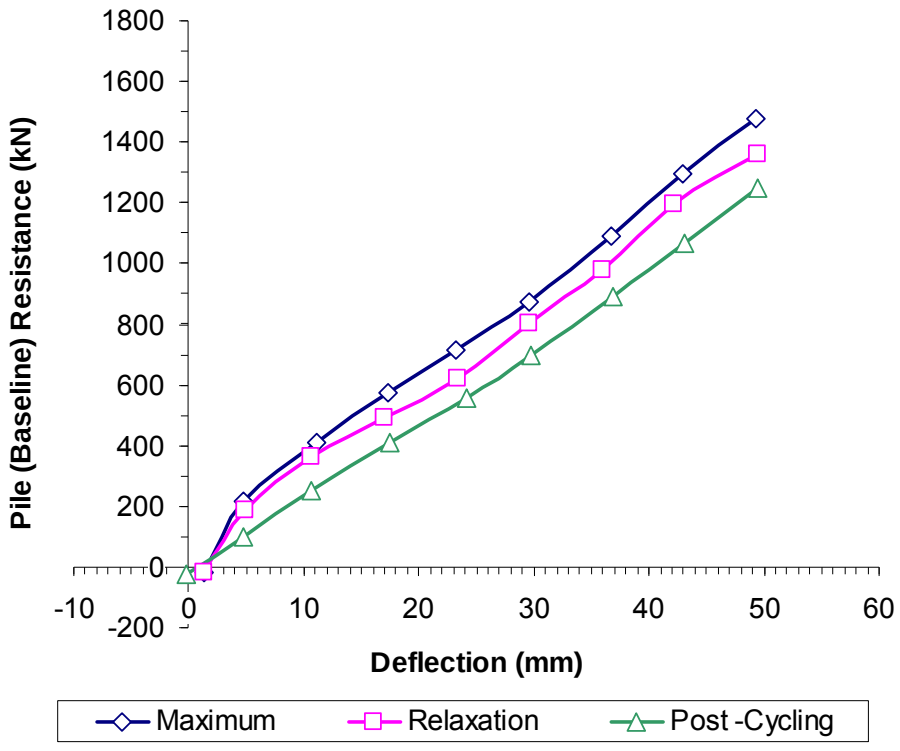

Figure 5.5: Baseline (no backfill) load-deflection curves

5.2.3 STATIC PASSIVE EARTH RESISTANCE

To isolate the static passive earth resistance, the pile cap (baseline) resistance is subtracted from the loose silty sand system response. Identical deflection values between the system resistance and pile resistance load-deflection curves are not typically achieved and were not experienced in this testing. Thus using the deflection values of the system resistance as a reference, an interpolation of the loads for the pile resistance was needed to produce loads that would be subtracted from the system resistance response at a common deflection. The maximum, static passive resistance curve accounts for ~22% of the total system resistance at a given deflection (compare Figure 5.2 with Figure 5.6).

The percent degradation between the relaxation and maximum load was ~30% at small deflection but decreased to ~15% at greater deflections; higher percent degradations then those presented in the loose silty sand case and no backfill case. This is approximately a median load degradation of 37 kN. The overall degradation of the passive earth resistance due to relaxation is a median value of ~17%. The percent degradation expressed by the difference of the post-cycling and maximum load normalized by the maximum load a decreased from about ~90% at small deflections to ~50% at larger deflections; 30% and 35% percent higher, beginning of the range and ending of the range respectively, than the range presented for the loose silty sand backfill case and no backfill case. This is a median load degradation of approximately 180 kN. The overall degradation of the passive earth resistance due to cyclic, dynamic loading is a median value of ~53%. Relaxation of the passive earth resistance at the conclusion of cycling load typically reduced the resistance to about 30% of its initial maximum value.

The remaining capacity of the system is attributed to both residual strength in the backfill soil and the pile resistance.

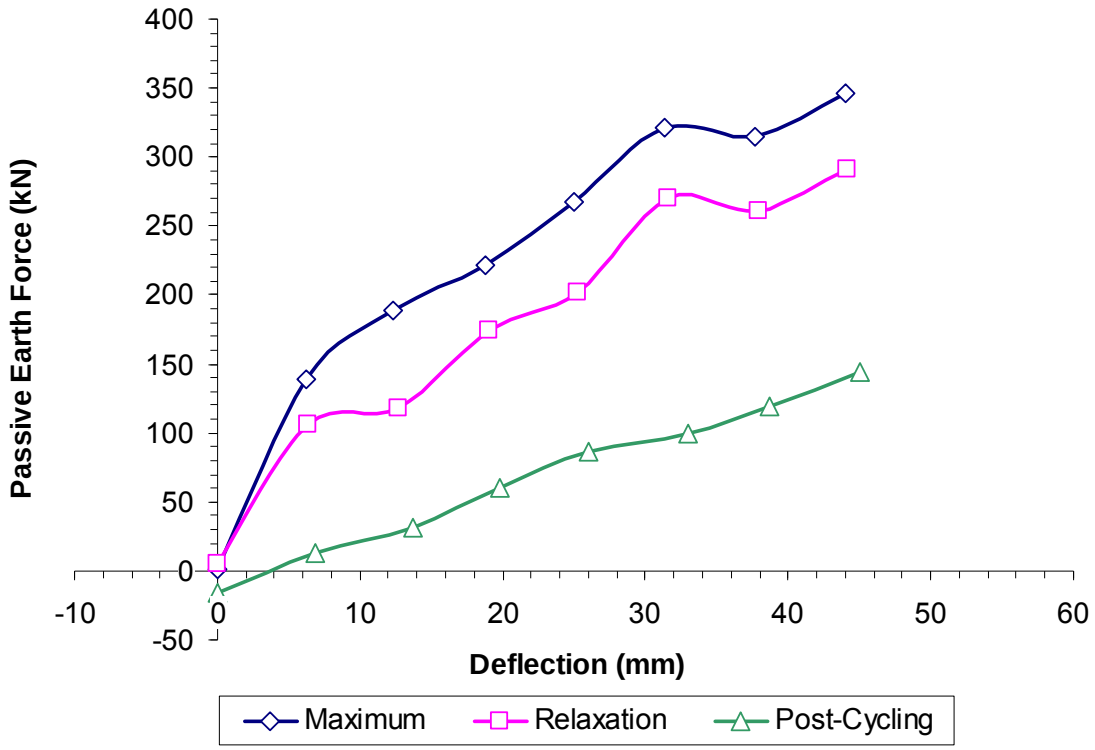

Figure 5.6: Loose silty sand passive earth load-deflection curves

5.2.4 COMPARISON OF MEASURED & COMPUTED PASSIVE FORCE

The literature presented in chapter 2 discusses several methods used to calculate the ultimate horizontal passive force, P_{ult}, and produce force-deflection curves. Commonly used methods include Rankine, Coulomb, Log-spiral, and Caltrans. These methods were used to compute the ultimate horizontal passive force and compared to the loose silty sand measured results. Table 5.1 summarizes the assumptions used to calculate

the four previously enumerated methods. The parameters are in general agreement with the measured properties with two exceptions. First, the cohesion in the backfill has been neglected. If cohesion were to be included the computed P_{ult} would be much higher than the measured value in all cases. This was also the parameter which was most uncertain from the field and lab data. Secondly, the initial stiffness parameter (k) of 200 kips/ft^2 was at the low end of the range of values for either natural or compacted soil suggested by Duncan and Mokwa (2001). This low value was necessary to produce better agreement with the measured curve and is likely due to the fact that the soil in this test was in an very loose state.

Table 5.1: Summary of assumptions used to compute P_{ult}

cap width,	b (ft) =	17.00
cap height,	H (ft) =	3.67
embedment depth,	z (ft) =	0.00
surharge,	q_s (psf) =	0.0
cohesion,	c (psf) =	0.0
soil friction angle,	ϕ (deg.) =	28.0
wall friction,	δ (deg.) =	20
initial soil modulus,	E_i (kip/ft^2) =	200
poisson's ratio,	ν =	0.30
soil unit weight,	γ_m (pcf) =	110.0
adhesion factor,	α =	1.00
Δ_{max}/H, (0.04 suggested) =		0.05

The Rankine method assumes a linear failure surface and neglects wall friction. The Coulomb method also assumes a linear failure surface but accounts for wall friction. The Log-spiral method uses a log-spiral shaped failure surface and includes the wall friction in its calculations. All three implicitly assume that soil pressure increases with depth. Caltrans uses a bi-linear model that only accounts for the height and the area of the

soil-wall interface. The cohesion is neglected and does not add to the soil resistance for all four cases.

Table 5.2: Measured and computed ultimate passive force comparison

Method	Ultimate Horizontal Passive Force, P_{uh}	Percent Error
Measured	347 kN	-
Rankine	182 kN	-47
Coulomb	337 kN	-3
Log Spiral	312 kN	-10
Caltrans	926 kN	+166

Applying these assumptions to each method appropriately and converting the results to SI units provided the comparisons found in Table 5.2. The Rankine method under estimated the ultimate passive force by 47%, while the Caltrans method over estimated the ultimate passive force by 166%. The Coulomb and Log-spiral methods provided the best correlation with an under estimated ultimate passive force of 3% and 10% respectively.

In the literature review provided in chapter 2, Duncan and Mokwa (2001) reported that the passive earth force was best estimated by applying the Log-spiral method with the Ovesen-Brinch Hansen correction, well known as the Duncan and Mokwa Hyperbolic method. This method, as well as the Caltrans method, is used to compute load-deflection curves to compare with the maximum passive earth force curve found in Figure 5.6 (see Figure 5.7).

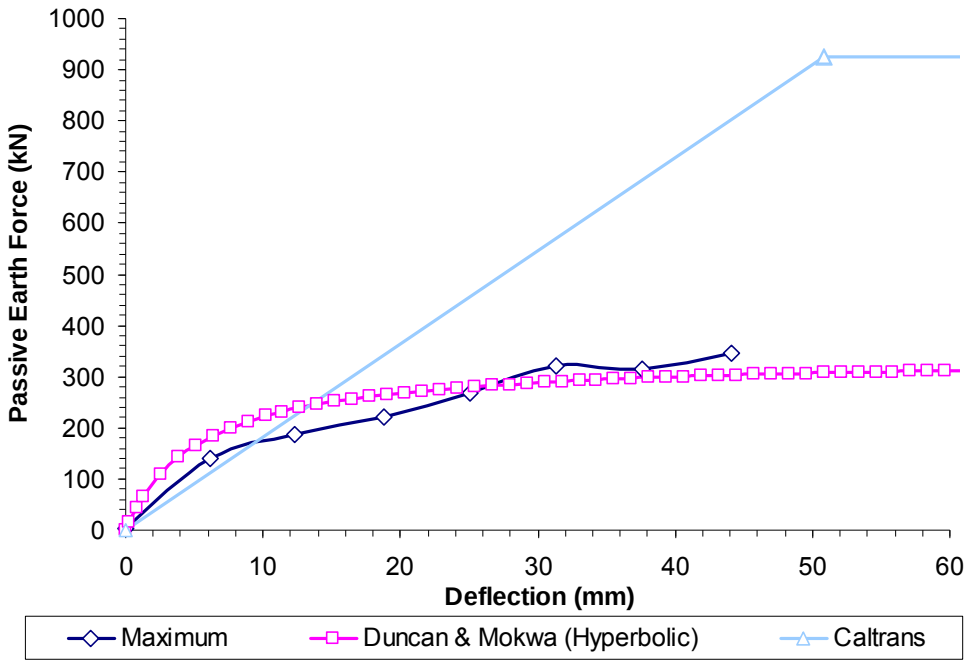

Figure 5.7: Measured and computed load-deflection curve comparison

The over estimation of the Caltrans method can be graphically seen in Figure 5.7. However, the Duncan and Mokwa hyperbolic method provides a generally good estimate in the region of highest deflection.

CHAPTER 6-DYNAMIC RESPONSE OF BACKFILL

6.1 INTRODUCTION

To better understand the cyclic, dynamic response data presented in this chapter, a section will be included which discusses the data processing procedures used to obtain the cyclic, dynamic response information. This chapter will then present and discuss the results from the cyclic, dynamic load testing involving the loose silty sand backfill. System cyclic, dynamic load-deflection curves as a function of target displacement will be shown. In addition, system cyclic, dynamic load-deflection curves are presented as a function of forcing frequency. The cyclic, dynamic degradation relationship as a function of frequency from 1 to 8 Hz will also be quantified. These same relationships will also be presented separately for the baseline response under cyclic, dynamic loading. The baseline curves will then be subtracted from the appropriate system curves to obtain the cyclic, dynamic load-deflection curves for the passive resistance contribution. Based on the appropriate dynamic load-deflection curves, stiffness and damping for the system, baseline, and passive resistance will be presented and discussed.

6.2 DATA PROCESSING PROCEDURES

A simplified graphical model of the physical test features was created and is presented in Figure 6.1. The left direction is taken as positive directional notation also the positive signal direction for the accelerations obtained from the accelerometer instrumentation.

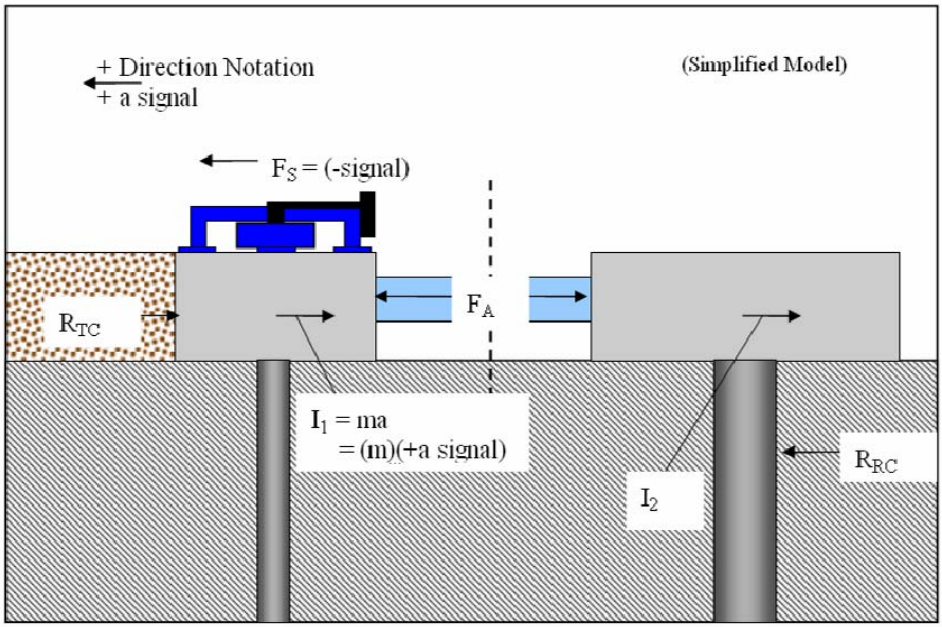

Figure 6.1: System free body diagram with system forces represented

As shown in Figure 6.1, R_{TC} is the reaction provided by the backfill soil and pile cap with components of stiffness and damping. R_{RC} is the reaction provided by the pile of the reaction cap having both stiffness and damping components. F_s is the shaker force provided to the system with a negative signal in the left direction. I_1 and I_2 are the inertial force for each mass, test cap and reaction cap respectively. When the shaker force changes direction, then the acceleration of the pile cap is taken as a negative value and

used in appropriate calculations of the inertial force. Including both pile caps in a free body diagram yields two equilibrium equations, a static and dynamic equilibrium equation (Equations 6.1 and 6.2 respectively).

$$-R_{TC} + R_{RC} + F_s = 0 \quad \textbf{(6.1)}$$

$$-R_{TC} + R_{RC} + F_s - I_1 - I_2 = 0 \quad \textbf{(6.2)}$$

.

If the system free body were cut into two free bodies, a left side and a right side, at the dash line (through the actuator), then two additional equilibrium equations are obtained (Equations 6.3 and 6.4 respectively). These equations allow the dynamic response of the reaction cap to be excluded from the free-body of each pile cap because the forces on the actuators are known. Solving Equation 6.4 for F_a, and then substituting it into Equation 6.3 and solving Equation 6.3 for F_s and substituting this into Equation 6.2 (the dynamic equilibrium equation) results in a balanced equation with all forces canceling. With this confirmation, the left equilibrium equation (Equation 6.3) was used to model the system to obtain dynamic displacement amplitude, average load, stiffness, and damping values.

$$-R_{TC} - I_1 + F_s + F_a = 0 \quad \textbf{(6.3)}$$

$$R_{RC} - F_a - I_2 = 0 \quad \textbf{(6.4)}$$

Solving Equation 6.3 for R_{TC} allows the load in the system (backfill + pile cap) or baseline (no backfill) case to be isolated. To begin the data processing, an input file was

prepared which included the load from the actuator, acceleration measurements acquired from the accelerometer, double integrated displacements from the accelerometer (the LVDTs became unreliable due to noise caused by vibration of the pile cap), and the loop counter signal from the eccentric shaker. In addition, the time record and approximate shaker frequency was included. Noise was experienced in the accelerometer data but was reduced by filtering producing reasonable results.

Using the model discussed previously this data was processed by a spreadsheet designed to calculate the shaker force, inertial force, dynamic displacement amplitude, the maximum, minimum, and median values of the displacement, stiffness, damping, and load. In the case of the load, the eccentric shaker force (calculated using Equation 4.1) and the inertial force load was added/subtracted to/from the actuator load to determine the reaction of the test cap, R_{TC}. The inertial force is calculated using:

$$I_1 = g * 386.4 * \text{mass} \quad \textbf{(6.5)}$$

where g is the measured accelerations and mass includes contributions from the weight of the test pile cap (93.5 kips), the weight of an 8 ft length of the 12 test piles which are assumed to be moving with the cap (17 kips), half the weight of the two actuators (8.8 kips), the weight of the eccentric shaker (5 kips), and the weight of the backfill within a log-spiral shear zone (30 kips).

Resulting system force-displacement loops were used to solve for the dynamic displacement amplitude, u (given by the difference between the maximum and minimum displacements in a given hysteresis loop divided by two), the stiffness, k, (given by the

difference between the maximum and minimum load in a given hysteresis loop divided by two then divided by the dynamic displacement amplitude). The average peak-to-peak slopes for the first 20 force-displacement loops during the dwell time at an increment of 0.5 Hz were used. Isolation of each cyclic effect was not exact due to the ramping nature of the eccentric shaker, starting at 1 Hz to 8 Hz as mentioned before. Damping, ζ, was calculated from the backfill force-displacement loops using the equation 6.5:

$$\xi = \frac{1}{4\pi}\frac{A}{E_s} \tag{6.6}$$

where the area of the hysteresis loop is represented by A, and E_s is the stored strain energy which equals 0.5 ku_o, in which case k is the slope of the loop (stiffness) and u_o is its displacement amplitude.

6.3 LOOSE SILTY SAND BACKFILL DYNAMIC SYSTEM RESPONSE

6.3.1 LOAD-DEFLECTION CURVES

The average load and displacement were extracted from the output file produced by the data processing spreadsheet. The average was taken over twenty hysteresis loops. Average load-deflection curves for the dynamic tests are presented in Figure 6.2 and 6.3 in terms of deflection and frequency, respectively. The static maximum, relaxation and post-cycling load-deflection curves are also shown in these figures for comparison.

The dynamic system load-deflection curves correlate well with the previously presented static loose silty sand curves. When the dynamic system response curves are

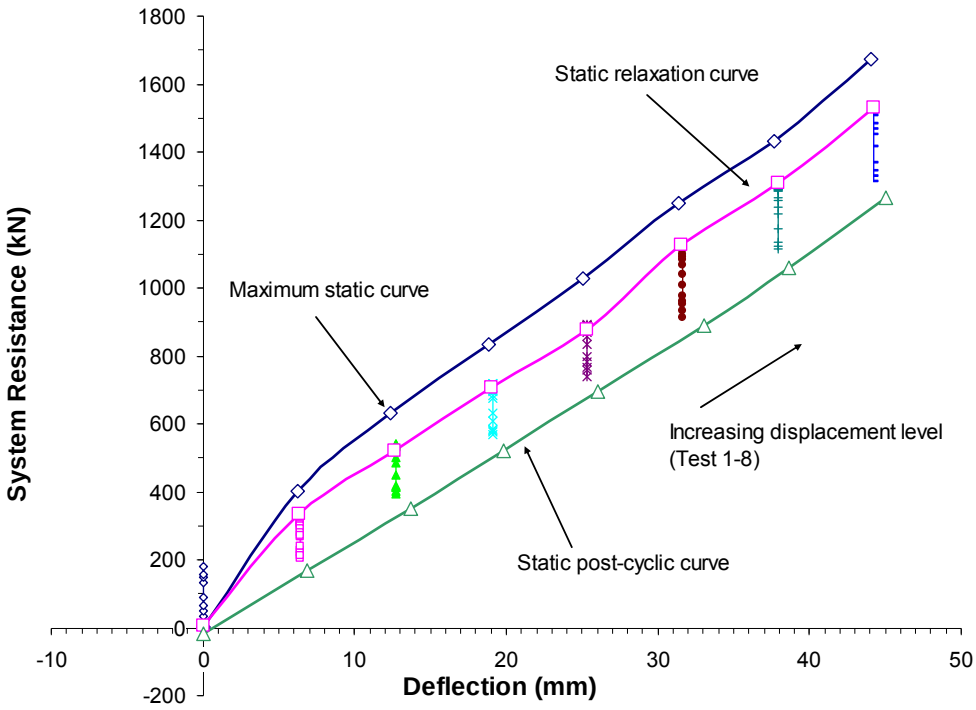

Figure 6.2: Loose silty sand static and dynamic system load-deflection curves

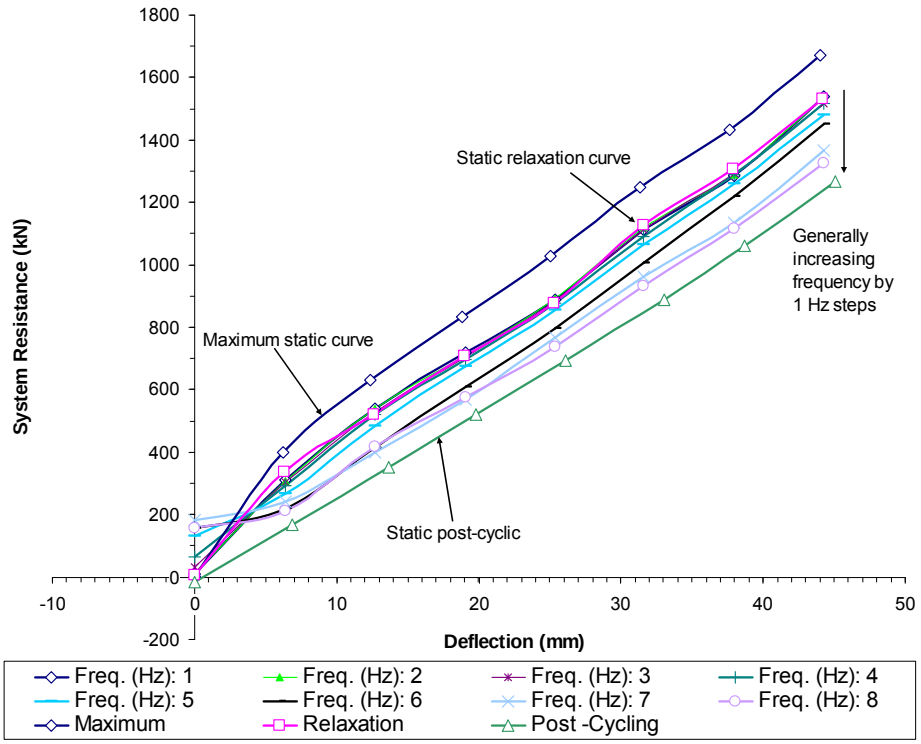

Figure 6.3: Loose silty sand static and dynamic system load-deflection curves (function of frequency)

superimposed upon the static loose silty sand system response curves, the dynamic response falls between the static relaxation and post-cycling curve as shown in Figure 6.2 and Figure 6.3. In Figure 6.2 a space is observed between the last point on the dynamic system load-deflection plot and the superimposed static system post-cycling load-deflection curve. This is caused by additional degradation in the system as the eccentric shaker ramped down from its 8 Hz peak frequency but not included in these curves.

Observing the data used to create Figure 6.2 and Figure 6.3, the load appears to increase as the forcing frequency increases from 1 to 3 Hz for each target deflection (tests 1 through 8). This increase is characteristic of the pile coming in contact with the backfill and activating the passive earth resistance. However, the peak passive earth response is reached and the backfill passive earth resistance then begins to degrade with the increase in frequency for each test. This degradation that is observed is not constant and could also be attributed to or a function of gapping effects or subsurface relaxation.

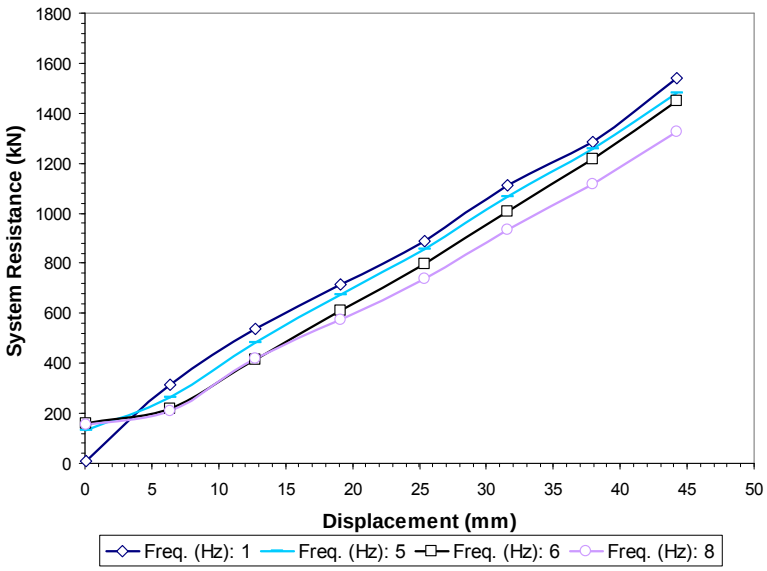

Figure 6.4: Loose silty sand system load-deflection curves (function of frequency)

Figure 6.4 plots the average load-deflection curves from the data in Figure 6.3 for selected frequencies. Observing the system load-deflection curves as a function of frequency closely (Figure 6.4), the frequencies 1 to 5 Hz generally show a trend of degradation (although increases in load are present as noted previously in the 1 to 3 Hz range). As the frequency rises out of this range to the 5 to 8 Hz range, frequencies 6 and 8 Hz. tend to map over one another at small deflections (0 to 19 mm deflection) but then the curve for 8 Hz. begins to show increased degradation.

6.3.2 DYNAMIC DISPLACEMENT AMPLITUDE

The dynamic displacement amplitude, u_0, was calculated for each load-deflection loop. The median dynamic displacement amplitude over the 20 loops for each frequency in each test is presented in Figure 6.6 and Figure 6.6.

The dynamic displacement amplitude is plotted as a function of the forcing frequency in Figure 6.5 for the tests conducted at each static deflection increment starting at 0 mm deflection at the left and increasing to the right at 6.35 mm increments. Due to resonance effects the dynamic displacement increases dramatically from 1 Hz to the peak displacement, which typically occurred between 6 and 7.5 Hz, and then deceased. The maximum displacement amplitude for each curve defines the damped natural frequency of the system. As the initial static deflection level increased, the peak displacement amplitude tended to decrease and the natural frequency of the system tended to increase. For example, peak dynamic displacement amplitudes decrease from about 1.7 mm for the test at zero static deflection to less than 1.3 at a static deflection 44 mm.

The damped natural frequency appeared to be about 5.5 Hz for the zero static deflection case, but then increased to a value of around 7 Hz at higher deflection levels.

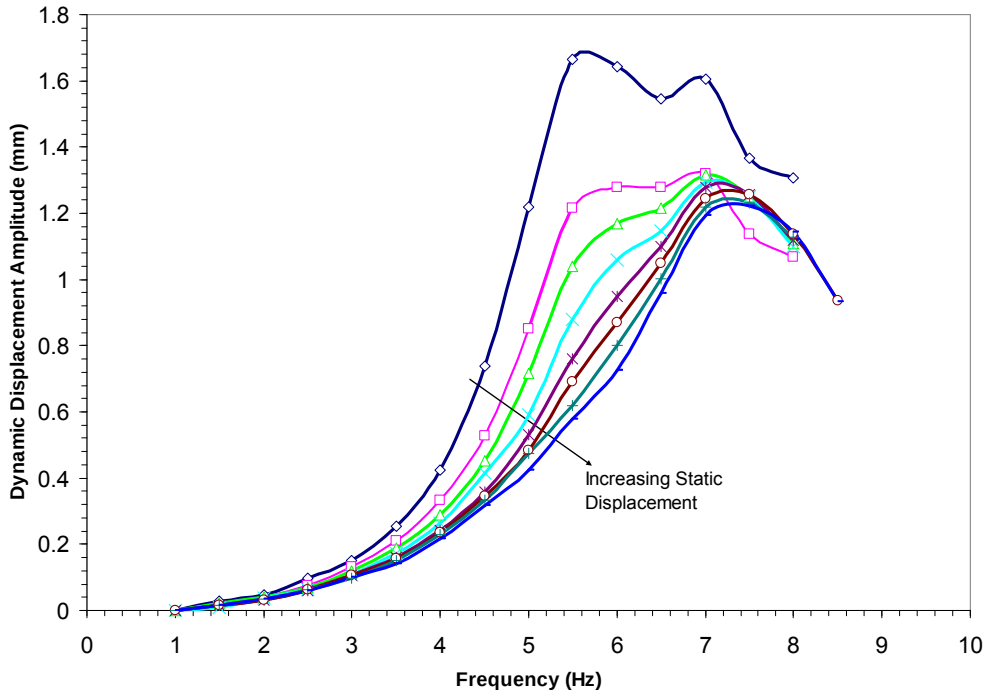

Figure 6.5: System dynamic displacement amplitude versus forcing frequency

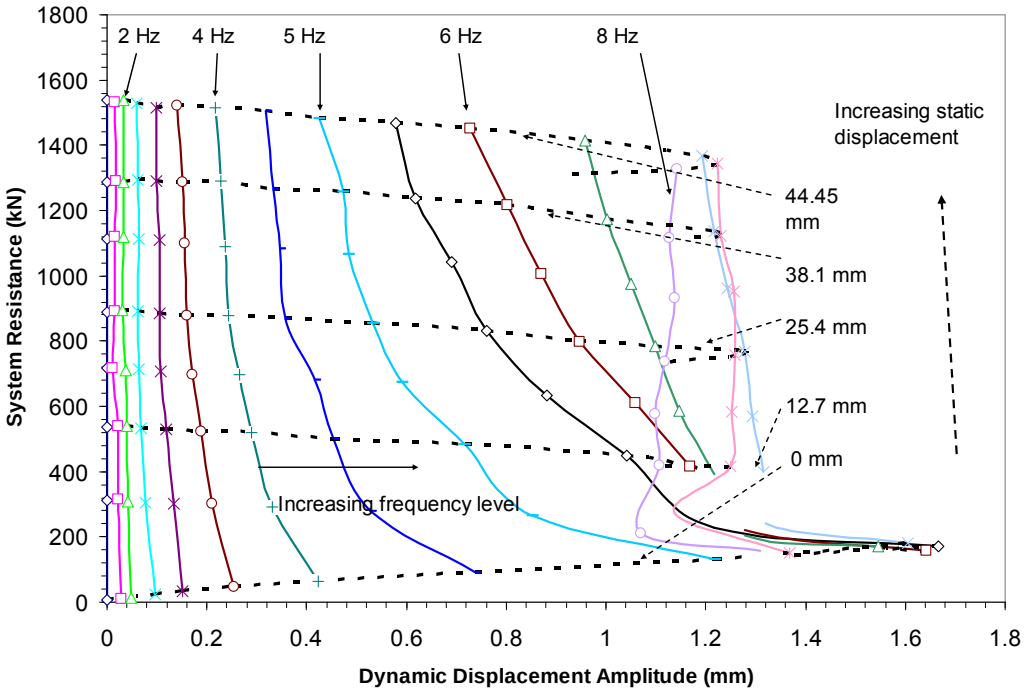

Figure 6.6: System dynamic displacement amplitude versus resistance.

However, the plot exhibits bi-modal resonance effects that are suspected to be the superposition of the resonance produced by the test cap and the reaction cap or possibly the effect of variations in gap widths around the piles in the cap.

In Figure 6.6, the solid curves which generally slope downward to the right represent the dynamic displacement amplitude as a function of frequency and static deflection level. These curves generally show that as the static displacement goes from 0.0 to 44.45 mm the average load increases and the dynamic displacement amplitude decreases. However, differences in the dynamic displacement amplitude do not begin to be distinguishable until the forcing frequency exceeds about 3.5 Hz because the system shows resonant characteristics between 7 and 7.5 Hz, the curves for these frequencies do not always follow the general trends. The dashed relatively horizontal curves represent the dynamic displacement amplitude as a function of the static displacement level. These curves typically show that as the frequency increases for a given static deflection level, the system resistance decreases slightly for all tests except that conducted prior to any loading. At frequencies around 7 Hz the curves pass through resonance and the system resistance is slightly decreased once again. The peak dynamic amplitude experienced by the system ranged from 1.2 mm to 1.3 mm

6.3.3 STIFFNESS AND DAMPING

Plots of the dynamic stiffness as a function of forcing frequency are provided for each static displacement level in Figure 6.7. The plots show stiffness values in the region of 100 kN/mm to 200 kN/mm. Although there appears to be a trend toward decreasing stiffness with increasing frequency particularly at low frequencies, it is important to note that the results obtained below 3 Hz are based on deflection values which are just slightly

higher than the noise in the system. As noted in Equation 4.1 the force applied by the eccentric mass shaker increases with frequency. As a result, the applied force at low frequencies is small, making deflections small. This is turn makes computed stiffness and damping values at these low frequencies somewhat questionable. Figure 6.7 shows a trend of decreasing stiffness from 3 to 6 Hz. Thereafter, the system begins to increase in stiffness. This pattern of decreasing then increasing stiffness is due in part to the increases and decrease in dynamic displacement amplitude caused by system resonance. Generally, as deflection increases, the stiffness tends to decrease and this behavior is reflected in the test results show in Figure 6.7. Apart from these trends, there does not appear to be any consistent trend in the stiffness as a function of the initial static deflection level.

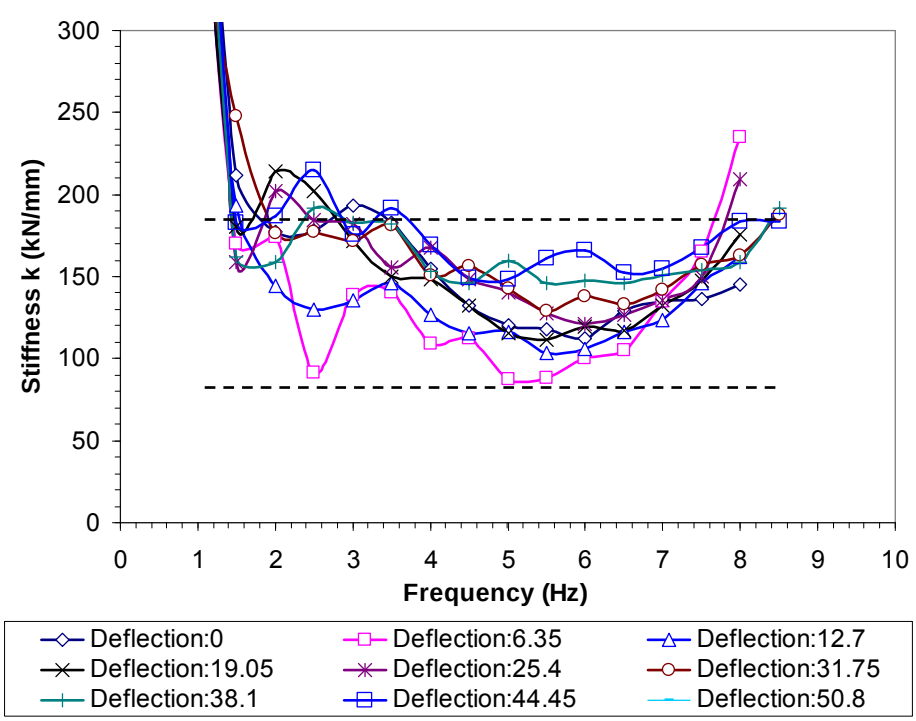

Figure 6.7: Loose silty sand system stiffness versus forcing frequency

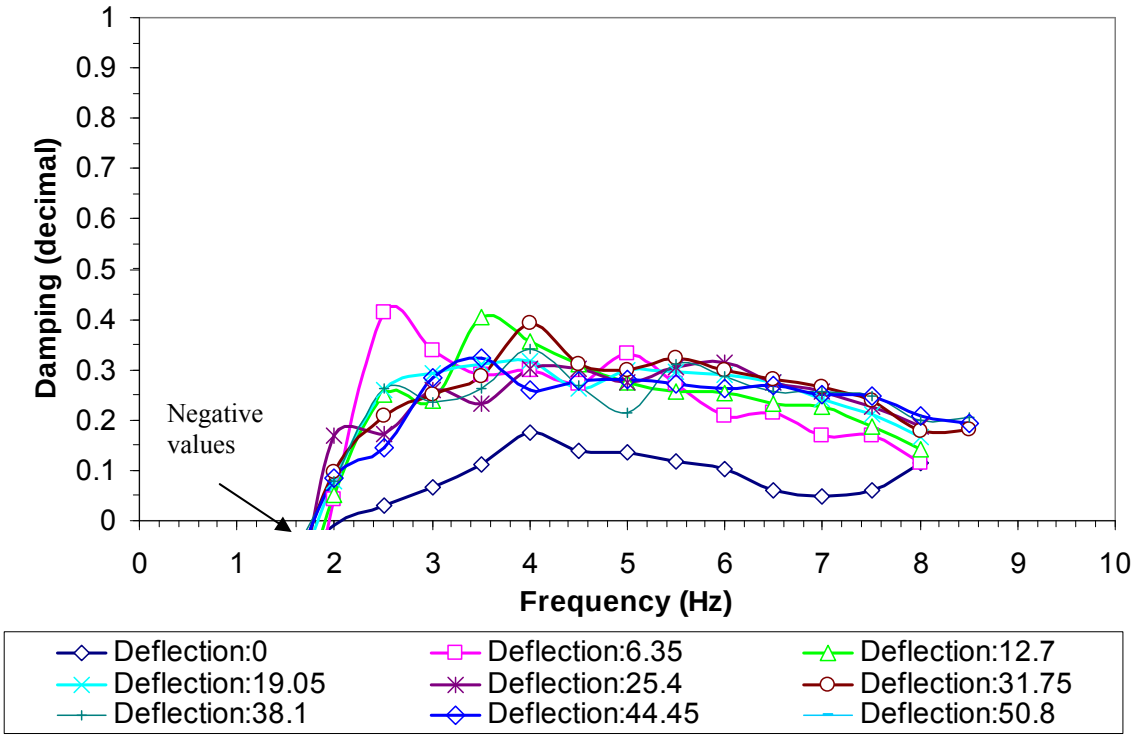

Figure 6.8: Loose silty sand system damping versus forcing frequency

The damping ratio is plotted as a function of forcing frequency for tests at each static deflection level in Figure 6.8. Apart from the test at zero static deflection, the damping ratios at the other deflection levels are relatively consistent and fall within a fairly narrow range. This result indicates that the damping ratio is relatively unaffected by the static deflection level except at very small deflections. System damping ratios for the pile cap with the loose silty sand backfill typically ranged from 25% to 35% for frequencies from about 3 to 6 Hz. However, from 6 to 8 Hz the data shows a decreasing trend in damping ratio with a typical range of 15% to 25%. The damping ratio for the pile cap at zero static deflection was much lower with a typical range between 5% and 15%. At this low deflection level, the passive force on the cap may not be mobilize sufficiently to produce the higher levels of damping observed at greater deflection levels.

6.4 BASELINE PILE DYNAMIC RESISTANCE RESPONSE

6.4.1 LOAD-DEFLECTION CURVES

Once again, the average dynamic load and displacement were extracted from the output file produced by the data processing spreadsheet. The average was taken over twenty hysteresis loops. Dynamic load-deflection curves are presented in Figure 6.9 and Figure 6.10 are in terms of deflection and frequency, respectively.

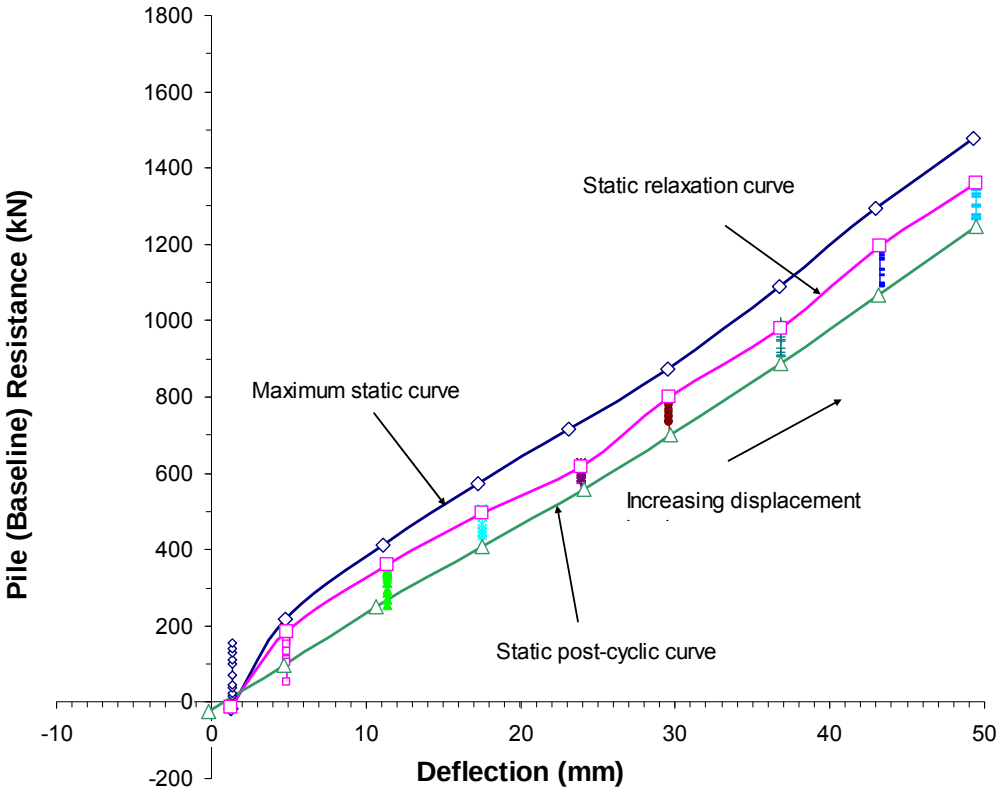

Figure 6.9: Baseline pile static and dynamic system load-deflection curves

The static maximum, relaxation, and post-cycling load-deflection curves are also shown in these figures for comparison. These dynamic system response load-deflection

curves for the baseline (no backfill) pile system also correlate well with their appropriate static curves. In Figure 6.9 a space is not observed between the last point on the dynamic system load-deflection plot and the superimposed static system post-cycling load-deflection curve. This is because this test does not have a backfill material that would continue degrading as the eccentric shaker ramped down as observed with the loose silty sand system response.

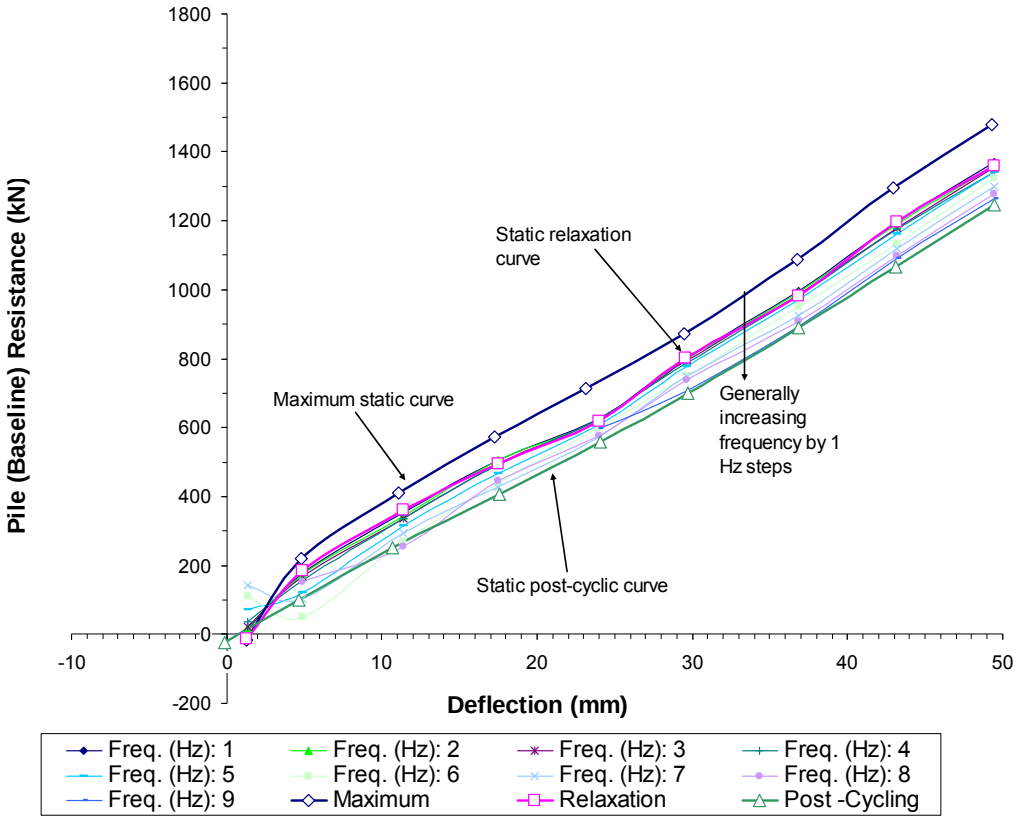

Figure 6.10: Baseline pile static and dynamic system load-deflection curves in terms of frequency

Observing the system load-deflection curves (Figure 6.11) closely, curves for frequencies between 1 to 4.5 Hz generally map over each other showing no large increases in load or large signs of degradations distinguishable to the naked eye; although

variations are observable. As the frequency rises out of this range to the 5 to 8 Hz range, degradation is distinguishable. Overall, there seems to be more variation in the results of these curves as compared to the test with the loose silty sand backfill against the pile cap.

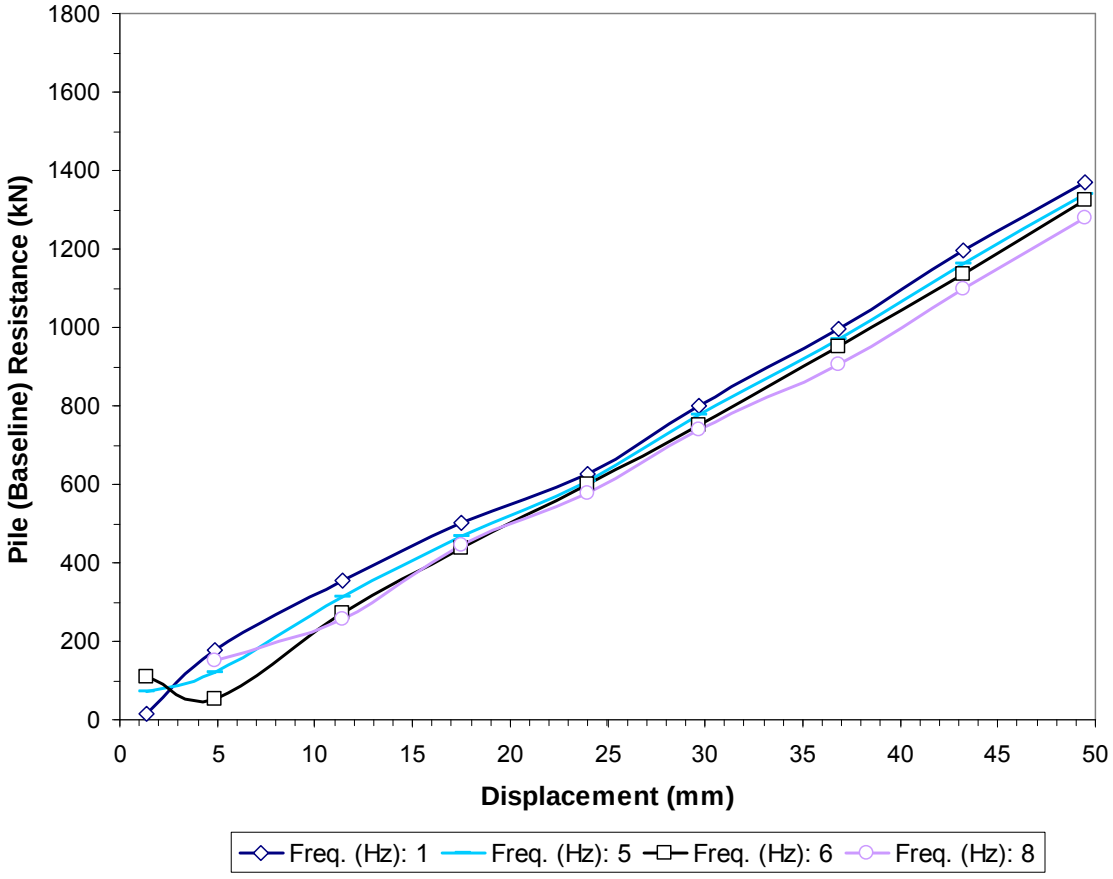

Figure 6.11: Baseline pile load-deflection curve in terms of frequency

6.4.2 DYNAMIC DISPLACEMENT AMPLITUDE

The pile (baseline) dynamic displacement amplitude expresses similar trends to that presented in the system response section; however, there are distinct differences (see Figure 6.12 and Figure 6.13). The dynamic displacement amplitude is plotted as a

function of the forcing frequency in Figure 6.12 for the tests conducted at each static deflection increment. A change in the shaker basket weights is easily observed in the dynamic displacement amplitude versus frequency plot. As mentioned previously, a bi-modal resonance effect is suspected to be present. Furthermore, the decrease in dynamic displacement amplitude is observed for the lighter shaker weight. As the initial static deflection level increased, the peak displacement amplitude tended to decrease and the natural frequency of the system tended to increase. Peak dynamic displacement amplitude typically decreased from 1.6 to 1.5 mm for low static deflection levels with the larger shaker weight to about 0.8 mm at greater static deflection levels with the smaller shaker weight. By observation, the natural frequency of the system falls in the range of 5 and 7.5 Hz. and increases as the static load level increases.

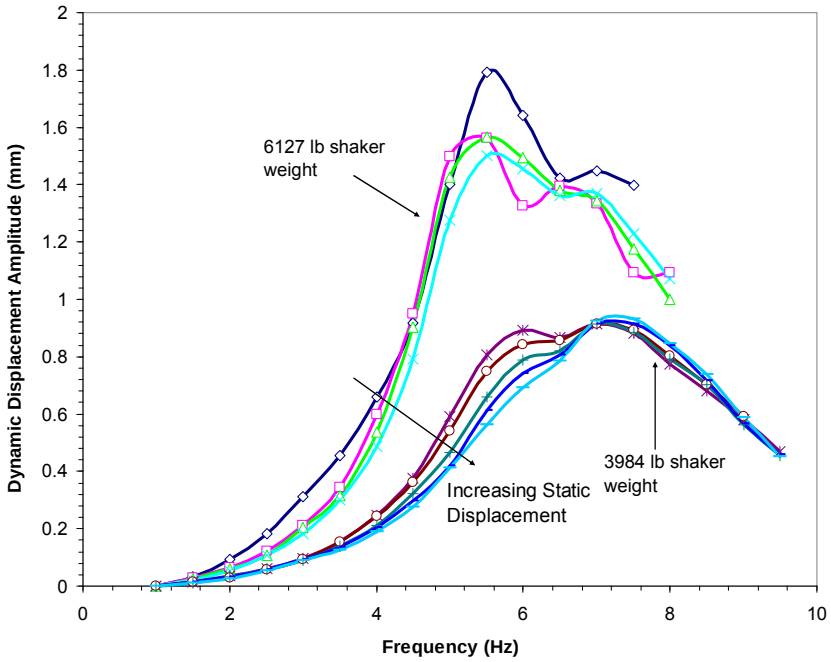

Figure 6.12: Pile (baseline) dynamic displacement amplitude versus forcing frequency

Figure 6.13 shows two distinct differences when compared to the system with loose silty sand backfill. The first difference is observed in the dashed lines representing the dynamic displacement amplitude as a function of static displacement, the resistance decreases much less with increasing frequency relative to the test with backfill. This may be attributed to the decrease of resistance seen in the system dynamic displacement amplitude to the loose silty sand backfill. The second difference is the dramatic drop in displacement amplitude at 25.4 mm. This is observed for all frequencies. This is due to the change in the shaker basket weight at test 5 (25.4 mm target deflection) mentioned before. The weight was decreased from 692.2 kN-mm (6127 lb-in) to 450.1 kN-mm (3984 lb-in).

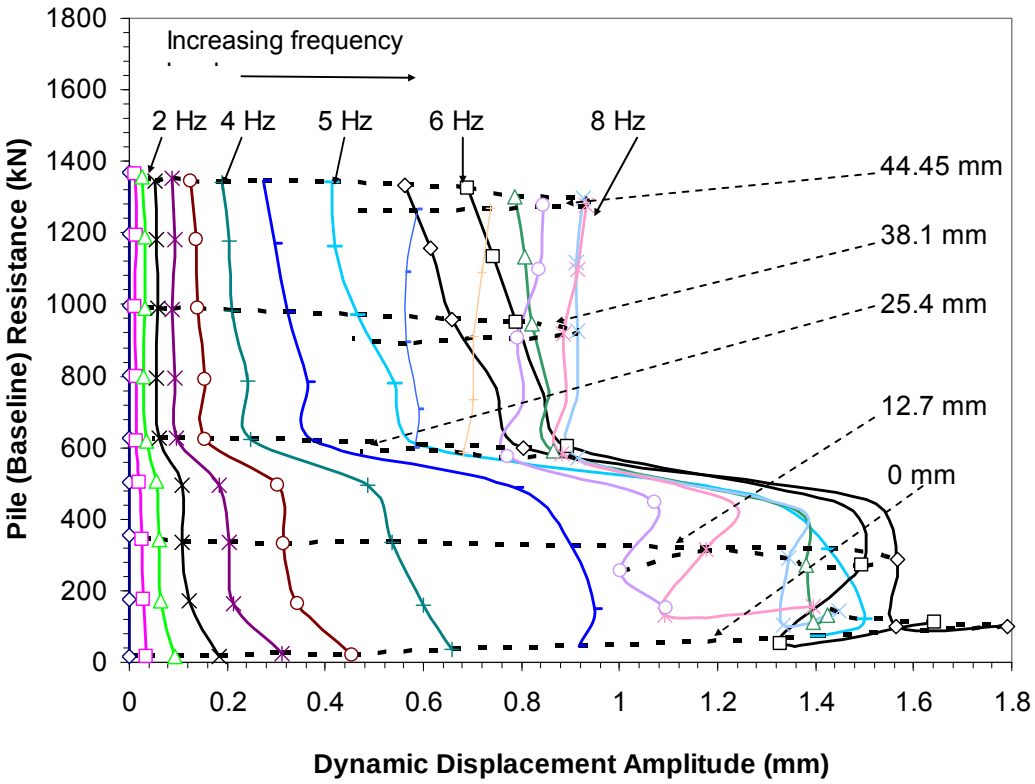

Figure 6.13: Pile (baseline) dynamic displacement amplitude versus resistance

6.4.3 STIFFNESS AND DAMPING

Plots of the dynamic pile (baseline) stiffness as a function of forcing frequency are provided for each static displacement level in Figure 6.14. The plots show each static displacement test taking on stiffness values in the region of 40 kN/mm to 100 kN/mm for frequencies between 4 and 8 Hz. This stiffness is about half of that observed for the test with backfill in place. Figure 6.14 shows a trend of decreasing stiffness from 3 to 5.5 Hz. Thereafter, the system begins to increase in stiffness. This decrease in stiffness from 3 to 5.5 Hz is likely due in part to the increases in dynamic displacement amplitude caused by system resonance. This is in harmony with the observation that stiffness typically decreases as displacement increases.

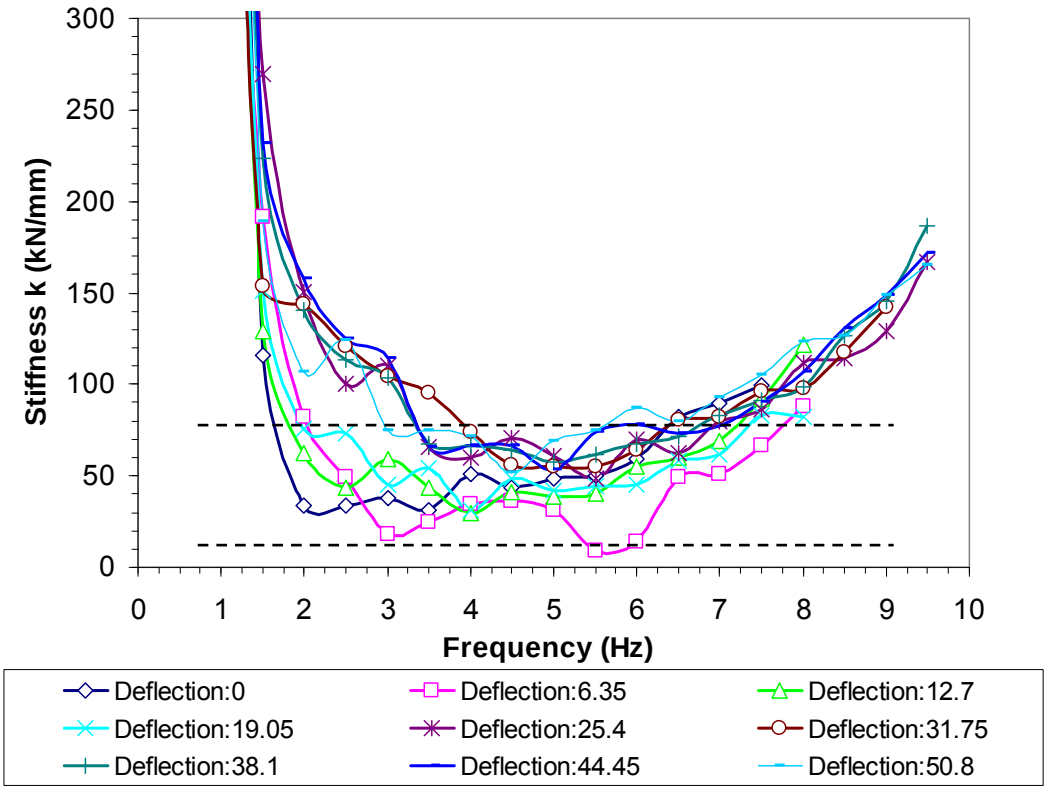

Figure 6.14: Pile (baseline) stiffness versus forcing frequency

The damping ratio for the pile cap alone (baseline condition) is plotted as a function of forcing frequency for tests at each static deflection level in Figure 6.8. The test results indicate that damping decreases substantially as the forcing frequency increases. There does not appear to be any consistent trend in damping with static deflection level. In addition, the damping exhibited by the 6.35 mm displacement does not follow the normal trend and will currently be ignored. In the frequency range from 3 Hz to 4.5 Hz. the damping ratio was within the range of 25% to 50%. However, from 4.5 Hz to 8 Hz. the data shows a decreasing trend in damping trailing off to zero between 8 and 9 Hz.

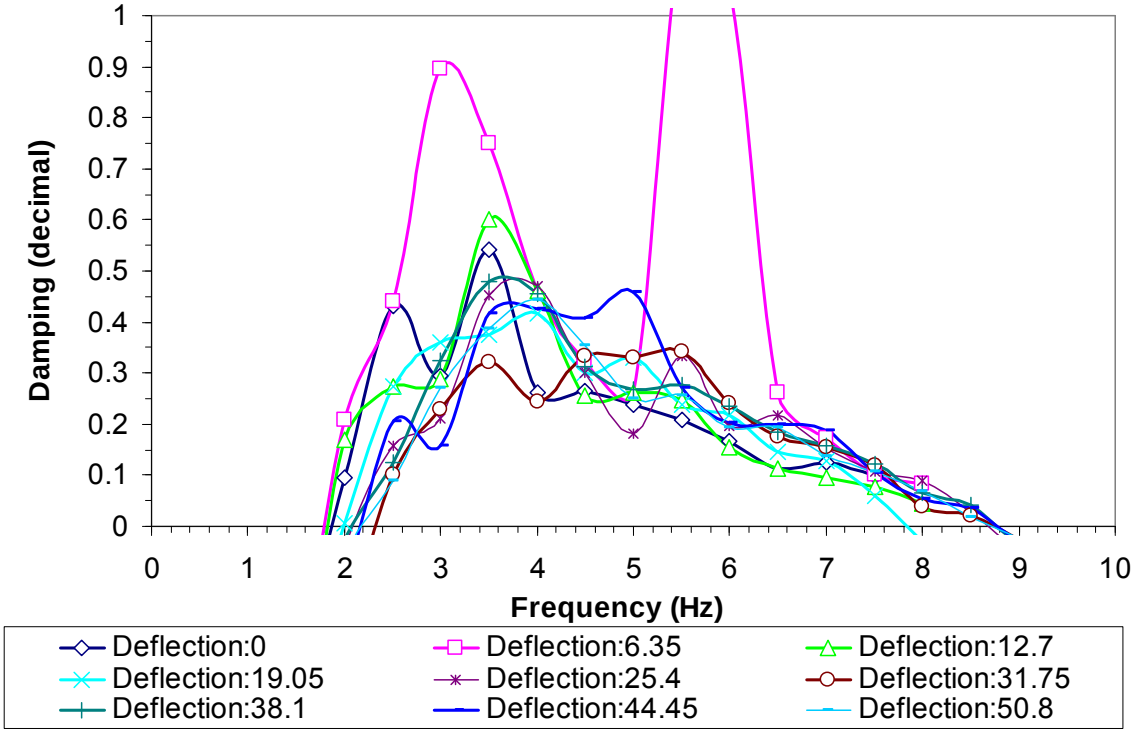

Figure 6.15: Pile (baseline) damping versus forcing frequency

6.5 DYNAMIC PASSIVE EARTH RESISTANCE RESPONSE

6.5.1 LOAD-DEFLECTION CURVES

Once again the passive earth resistance was isolated using the difference between the dynamic response of the pile cap system with loose silty sand backfill and the baseline pile dynamic response. However, errors inherent to linear interpolation are more pronounced in the resultant dynamic passive earth resistance curves. When interpolating, if the slope between two points that straddle the desired deflection is very steep, the interpolated load may introduce error when solving for the passive earth resistance. Dynamic load-deflection curves are presented in Figure 6.16 and Figure 6.17 in terms of deflection and frequency, respectively.

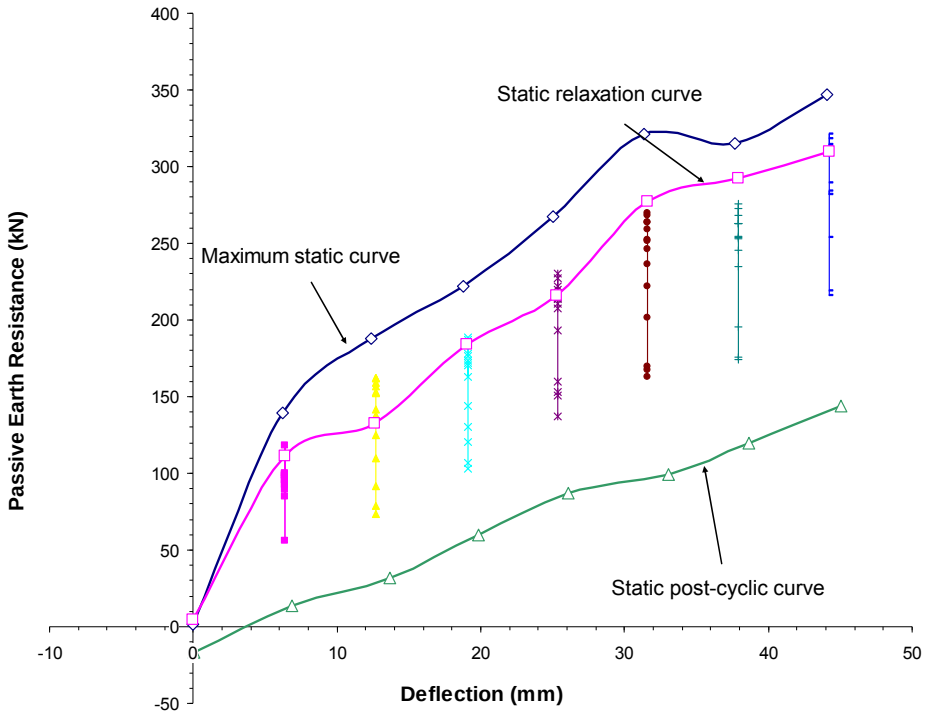

Figure 6.16: Static and dynamic passive earth resistance load-deflection curves

The static maximum, relaxation and post-cycling load-deflection curves are also shown in these figures for comparison. By observation, the dynamic load-deflection curves presented in Figure 6.16 have a wider spread of load values for each tested deflection. In other words, the drop off in load capacity of the backfill is more pronounced than that observed for the pile cap alone.

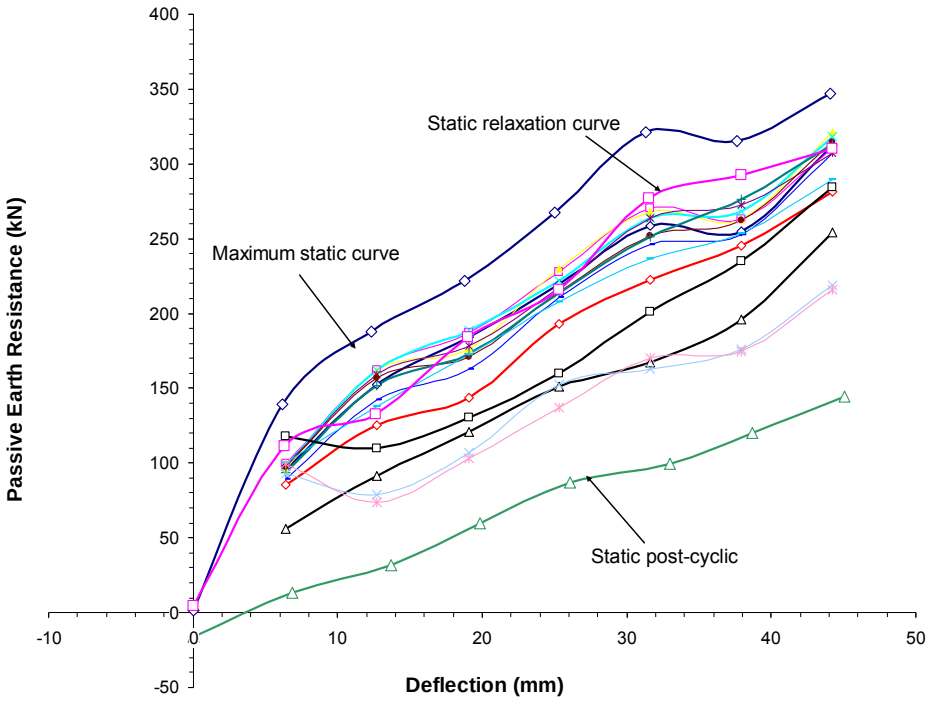

Figure 6.17: Static and dynamic passive earth resistance load-deflection curves in terms of frequency

Over the last six tests, excluding the first two tests because of variability, the percent degradation experienced by the passive earth resistance between 1 to 8 Hz ranged from ~52% to ~30%, for tests three to eight. These estimates represent the difference of the load at the beginning of the test to ending of the test. This approach does not account for the backfill gaining a little strength in certain instances experienced in the 1 to 2.5 Hz range. In comparison, the percent degradation experienced by the baseline curves

between 1 to 8 Hz ranged from ~11% to 8%, for tests three to eight; lower values due to the lack of backfill.

Superimposing the static passive earth resistance curves upon the dynamic passive earth resistance curves reveals the approximate error that may have been introduced by the interpolation process. Generally, the error appears to be rather small and the dynamic curves fit appropriately within the static load-deflection boundaries.

6.5.2 STIFFNESS AND DAMPING

Plots of the dynamic passive backfill stiffness as a function of forcing frequency are provided for each static displacement level in Figure 6.18. The passive earth stiffness

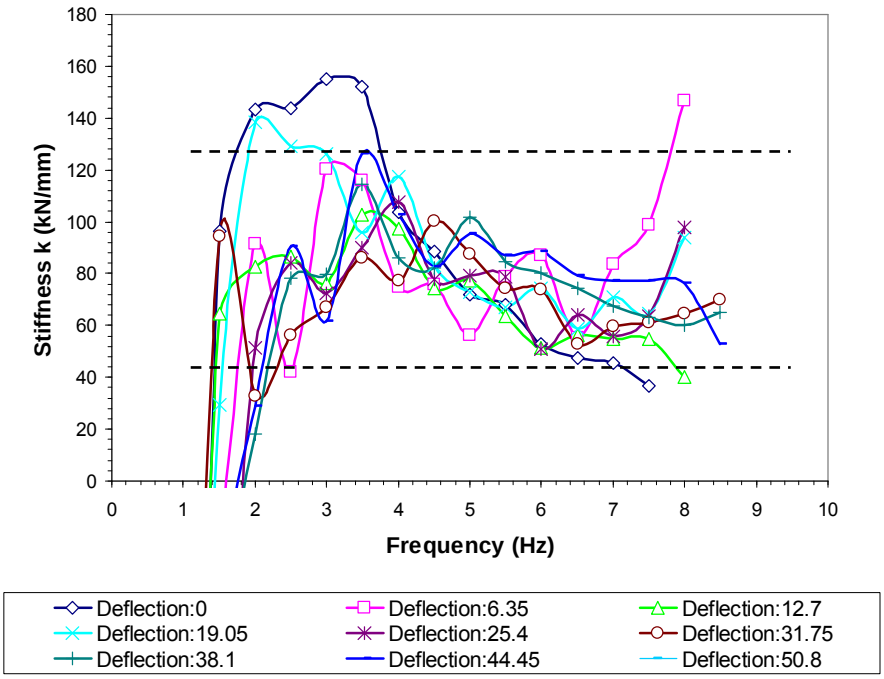

Figure 6.18: Loose silty sand passive earth stiffness versus forcing frequency

was calculated by simply subtracting the baseline (no backfill) stiffness from the loose silty sand stiffness, yielding the passive earth stiffness. The passive earth stiffness clearly decreases with frequency in the frequency range from 3 to 8.5 Hz. Within this frequency range the computed stiffness values are in the region of 40 kN/mm to 130 kN/mm. These passive soil stiffness values are roughly about half of the stiffness of the total system stiffness and they are about the same or slightly higher than the baseline stiffness values.

The damping ratio for the passive backfill soil alone is plotted as a function of forcing frequency for tests at each static deflection level in Figure 6.19. The loose silty sand backfill damping ratio was obtained by first calculating the damping coefficient, c, for both the system (backfill) and baseline (no backfill) case using Equation 6.7 and Equation 6.8:

$$c_{system} = \zeta_{system} * 2\sqrt{k_{system} * m_{system}} \quad \textbf{(6.7)}$$

$$c_{baseline} = \zeta_{baseline} * 2\sqrt{k_{baseline} * m_{baseline}} \quad \textbf{(6.8)}$$

$$c_{backfill} = c_{system} - c_{baseline} \quad \textbf{(6.9)}$$

$$\zeta_{backfill} = \frac{c_{backfill}}{2\sqrt{k_{backfill} * m_{backfill}}} \quad \textbf{(6.10)}$$

where, ζ is the damping ratio, k is the stiffness, and m is the mass. Next, the baseline damping coefficient is subtracted from the system damping coefficient to isolate the loose silty sand (backfill) damping coefficient (Equation 6.9). Finally, the damping ratio is recomputed using Equation 6.10 with the known stiffness and mass of the loose silty sand backfill.

Damping experienced by the isolated loose silty sand shows a generally increasing trend with frequency for frequencies from 3 to 8 Hz (see Figure 6.19). However, there is much more scatter in the damping ratio for the passive soil resistance than for the baseline or total system cases. Nevertheless, the average damping ratio shown for the backfill soil increases from about 32% at a frequency of 3 Hz to a value of about 55% at a value of 8 Hz. This damping ratio for the backfill soil is considerably higher than that for the pile cap only. The higher damping ratios at higher frequencies exhibited by the backfill provide the additional damping which allows the system damping to remain roughly constant over a wide frequency range.

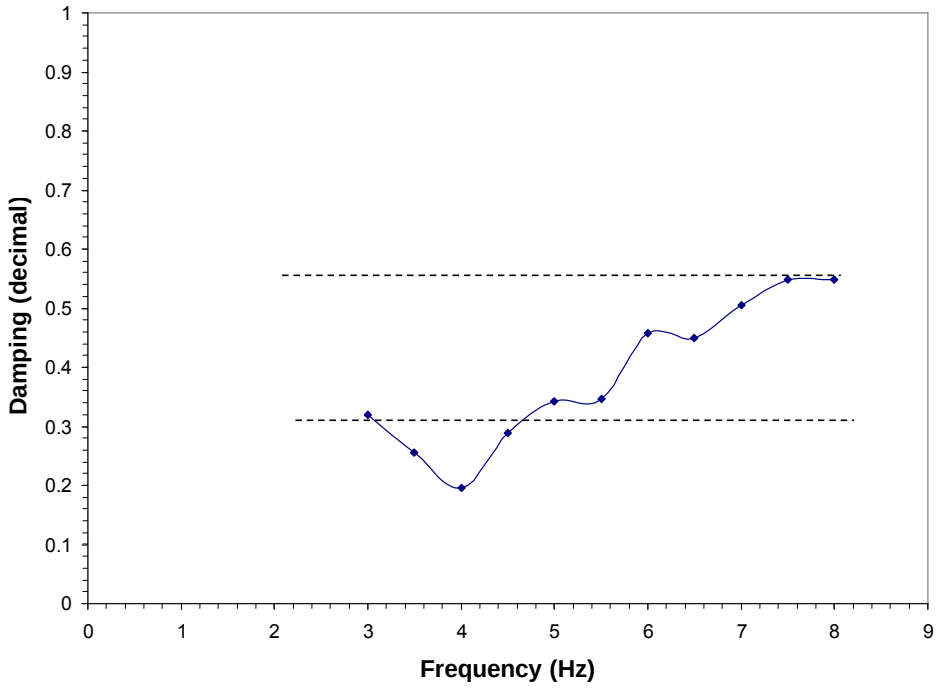

Figure 6.19: Loose silty sand passive earth damping versus forcing frequency

CHAPTER 7- CONCLUSION

Based on the analysis of the cyclic and dynamic testing of a full-scale pile cap with loose silty sand backfill the following conclusions are presented:

1) Despite the fact that the backfill sand was in a loose state, the passive earth resistance accounted for approximately 22% of the total system resistance, with piles contributing approximately 78%.

2) Relaxation of the passive earth resistance at the conclusion of cycling load typically reduced the resistance by about 70% of its initial maximum value. Generally, 17% of this decrease can be attributed to relaxation immediately prior to cyclic loading while the remaining 53% occurred during the cyclic loading.

3) The Coulomb and Log-spiral methods for estimating P_{ult} yielded the best agreement with measured capacity with under-estimations of 3% and 10% error, respectively. The Rankine and Caltrans methods produced results which under- and over-estimated the measured capacity by 47% and 166%, respectively. The Duncan and Mokwa hyperbolic method provided the best estimate of the measured load-deflection curves.

4) The dynamic displacement amplitudes during the eccentric mass shaker tests typically ranged between .4 and 2 mm for frequencies between 5 and 9.5 Hz. The displacement levels were small enough that the load-displacement loops remained entirely below the previous maximum load and represent behavior under reloading conditions rather than virgin loading conditions.

5) The dynamic displacement tended to decrease somewhat as the total static load applied to the system increased. In addition, the natural frequency falls in the range of 5 and 7.5 Hz. as the static load level increases.

6) In general terms, the presence of the loose silty sand backfill nearly doubled the dynamic stiffness of the pile cap. The stiffness of the backfill and pile cap combined was typically between 100 and 200 kN/mm for frequencies between 4 and 8 Hz, while the stiffness for the backfill alone was typically between 40 and 100 kN/mm for frequencies between 4 and 8 Hz.

7) Generally, the stiffness of the pile cap and the pile cap with backfill appears to decrease with frequency until the natural period of the system is approached but then begins to increase with frequency. This trend is especially evident for the case with the pile only but is less evident for the case with the pile cap and backfill.

8) The damping ratio for the pile cap with backfill typically ranged from 35 to 10% and the damping ratio for the pile cap without backfill

ranged from 50 to 8% within the frequency range from 4 to 8 Hz. In both cases, the damping ratio is considerably higher than would be expected for structural materials, but is typical of applications involving soil-structure interaction. The damping ratio is also higher than the 10% value suggested for use in some seismic codes.

9) The overall isolated loose silty sand stiffness shows a general decreases trend with values from 130 to 40 kN/mm for frequencies 4 to 8 Hz. However, the isolated loose silty sand damping ratio shows a general increasing trend with values from 32% to 55% for frequencies 3 and 8 Hz.

REFERENCES

Bozorgzadeh, A., Ashford, S. A., and Restrepo, J. I. (2005). "Stiffness and ultimate strength of bridge abutments: soil-dependent model". *Proceedings of the Caltrans Bridge Research Conference*, Paper No. 04-504, Sacramento, California.

Caltrans (2004). "Seismic design criteria, version 1.3." California Department of Transportation, Sacramento, California.

Clough, G.W., and Duncan, J.M. (1991). Earth retaining structures. *In Foundation engineering handbook.* 2nd ed. *Edited by* H.Y. Fang. Van Nostrand Reinholdt, New York, pp. 223–235.

Cole, R.T. (2003). "Full-Scale Effects of Passive Earth Pressure on The Lateral Resistance of Pile Caps." Doctor of Philosophy Dissertation, Brigham Young University, Provo, Utah.

Cole, R. T. and Rollins, K. M., (2006). "Passive earth pressure mobilization during cyclic loading." *Journal of Geotechnical and Geoenvironmental Engineering,* ASCE Companion paper submitted to ASCE for Review.

Duncan, J.M., and Chang, C.-Y. (1970). "Nonlinear Analysis of Stress and Strain in Soils". Journal of Soil Mechanics and Foundations Division, ASCE, Vol. 96, No. Vol. SM5.

Duncan, J. M., and Mokwa, R. L., (2001). "Passive earth pressures: theories and tests." *Journal of Geotechnical and Geoenvironmental Engineering,* ASCE Vol. 127, No. 3, pp. 248-257.

Gadre, A., and Dobry, R., (1998). "Lateral cyclic loading centrifuge tests on square embedded footing." *Journal of Geotechnical and Geoenvironmental Engineering*, ASCE Vol. 124, No. 11, pp. 1128-1138.

Goel, R. K., and Chopra, A. K. (1997). "Evaluation of bridge abutment capacity and stiffness during earthquakes." *Earthquake Spectra,* Vol. 13, No. 1, pp. 1-23.

Humar, J. L.(1990). "Dynamics of structures", Prentice-Hall, Englewood Cliffs, N.J.

Mokwa, R. L. and, Duncan, J. M., (2001). "Experimental evaluation of lateral-load resistance of pile caps." *Journal of Geotechnical and Geoenvironmental Engineering,* ASCE Vol. 127, No. 2, pp. 185-192.

Personius, S.F., and Scott, W.E. (1992). "Surficial geologic map of the Salt Lake City segment of the Wasatch Fault Zone, Davis, Salt Lake, and Utah Counties, Utah" U.S. Geological Survey miscellaneous Investigation Series Map 1-2106, scale 1:50,000.

Price, T. E. and, Eberhard, M.O., (2005). "Factors contributing to bridge-embankment interaction." *Journal of Structural Engineering,* ASCE Vol. 131, No. 9, pp. 1345-1354.

Rollins, K. M., Clayton, R.J., Mikesell, R. C., and Blaise, B. C. (1997). "Drilled shaft side friction in gravelly soil." Report No. UT-97.02, *Utah Department of Transportation*, Utah.

Rollins, K. M. and, Cole, R. T., (2005). "Cyclic lateral load behavior of a pile cap and backfill." *Journal of Geotechnical and Geoenvironmental Engineering,* ASCE Companion paper submitted to ASCE for Review.

Rollins, K. M. and, Sparks, A., (2002). "Lateral resistance of full-scale pile cap with gravel backfill." *Journal of Geotechnical and Geoenvironmental Engineering,* ASCE Vol. 128, No. 9, pp. 711-723.

APPENDIX A: INSTRUMENTATION LOCATIONS

The locations of fifty-five instruments are included in this summary with instrument measurement type, location, and unit type.

Table A.1: Instrument locations

NEESR-BYU
Phase 1, August 2005
T. Gerber & K. Rollins

Measurement Channel Table, Rev.10

R. Nigbor & A. Salamanca, nees@UCLA, 12/20/05

units appear to be in inches
South = + East = + Up = +

	No.	Measurement Type	Sensor ID	DAQ Channel No.	Sensor Source		Model	S/N	Sensor Component/Axis	Location, m			Orientation	Signal Conditioner	Data Units (EU)	Channel Sensitivity volts/EU	Qualitative Location
										X	Y	Z					
BNC-A	1	Displacement	D1	Q2781	BYU	MTS			1				X	Analog output from controller	in	0.25	East Actuator ("A, bad")
BNC-A	2	Displacement	D2	Q2782	BYU	MTS			1				X	Analog output from controller	in	0.25	West Actuator ("B, good")
BNC-A	3	Load	L1	Q2783	BYU	MTS			1				X	Analog output from controller	kip	0.01667	East Actuator ("A, bad")
BNC-A	4	Load	L2	Q2784	BYU	MTS			1				X	Analog output from controller	kip	0.01667	West Actuator ("B, good")
BNC-A	5	Shaker Speed	S1	Q2785	UCLA				1				na	Shaker control output	revolution	1.0	
BNC-B	6	Displacement	D3	Q2791	BYU	Ametek	P-20A	0704-22054	1	-150	102.25	-6	X	9.97VDC excitation	in	0.50	Reaction Cap, East Side, Top; South = -
BNC-B	7	Displacement	D4	Q2792	BYU	Ametek	P-20A	0801-16528	1	-150	102.25	-32	X	9.97VDC excitation	in	0.50	Reaction Cap, East Side, Bottom; South = -
BNC-B	8	Displacement	D5	Q2793	BYU	Ametek	P-20A	0701-16326	1	0	103	-6	X	9.97VDC excitation	in	0.50	Test Cap, East Side, Top; South = +
BNC-B	9	Displacement	D6	Q2794	BYU	Ametek	P-20A	0704-22058	1	0	-103	-6	X	9.97VDC excitation	in	0.50	Test Cap, West Side, Bottom; South = +
BNC-B	10	Displacement	D7	Q2795	BYU	Ametek	P-20A	0801-16527	1	0	103	-32	X	9.97VDC excitation	in	0.50	Test Cap, East Side, Bottom; South = +
BNC-B	11	Displacement	D8	Q2796	BYU	Ametek	P-20A	SP8-13597	1	-150.5	-103	-32	X	9.97VDC excitation	in	0.50	Reaction Cap, West Side, Bottom; South = -
Q-A	12	Acceleration	A1	Q2891	UCLA	Kinemetrics	ES-T	1701	1	116.5	99	0	z	None	g	10.0	Test Cap, Top, SE Corner; Down = -
	13	Acceleration	A2	Q2892	UCLA	Kinemetrics	ES-T	1701	2	116.5	99	0	y	None	g	10.0	Test Cap, Top, SE Corner; East = +
	14	Acceleration	A3	Q2893	UCLA	Kinemetrics	ES-T	1701	3	116.5	99	0	x	None	g	10.0	Test Cap, Top, SE Corner; South = +
Q-B	15	Acceleration	A4	Q2894	UCLA	Kinemetrics	ES-T	1702	1	3	99	0	z	None	g	10.0	Test Cap, Top, NE Corner; Down = -
	16	Acceleration	A5	Q2895	UCLA	Kinemetrics	ES-T	1702	2	3	99	0	y	None	g	10.0	Test Cap, Top, NE Corner; East = +
	17	Acceleration	A6	Q2896	UCLA	Kinemetrics	ES-T	1702	3	3	99	0	x	None	g	10.0	Test Cap, Top, NE Corner; South = +
Q-A	18	Acceleration	A7	Q2901	UCLA	Kinemetrics	ES-T	1550	1	115.5	-98.5	0	z	None	g	10.0	Test Cap, Top, SW Corner; Down = -
	19	Acceleration	A8	Q2902	UCLA	Kinemetrics	ES-T	1550	2	115.5	-98.5	0	y	None	g	10.0	Test Cap, Top, SW Corner; East = +
	20	Acceleration	A9	Q2903	UCLA	Kinemetrics	ES-T	1550	3	115.5	-98.5	0	x	None	g	10.0	Test Cap, Top, SW Corner; South = -
Q-B	21	Acceleration	A10	Q2904	UCLA	Kinemetrics	ES-T	1445	1	3	-99	0	z	None	g	10.0	Test Cap, Top, NW Corner; Down = -
	22	Acceleration	A11	Q2905	UCLA	Kinemetrics	ES-T	1445	2	3	-99	0	y	None	g	10.0	Test Cap, Top, NW Corner; East = +
	23	Acceleration	A12	Q2906	UCLA	Kinemetrics	ES-T	1445	3	3	-99	0	x	None	g	10.0	Test Cap, Top, NW Corner; South = +

Table A.2: Instrument locations (continued)

NEESR-BYU
Phase 1, August 2005
T. Gerber & K. Rollins

nees@UCLA — The George E. Brown, Jr. Network for Earthquake Engineering Simulation

Measurement Channel Table, Rev.10

R. Nigbor & A. Salamanca, nees@UCLA, 12/20/05

units appear to be in inches
South = + East = + Up = +

	No.	Measurement Type	Sensor ID	DAQ Channel No.	Sensor Source		Model	S/N	Sensor Component/Axis	Location, m			Orientation	Signal Conditioner	Data Units (EU)	Channel Sensitivity volts/EU	Qualitative Location
										X	Y	Z					
Q-A	24	Acceleration	A13	Q2911	UCLA	Kinemetrics	ES-T	1443	1	-154.625	97.5625	0	z	None	g	10.0	Reaction Cap, Top, SE Corner; Down = -
	25	Acceleration	A14	Q2912	UCLA	Kinemetrics	ES-T	1443	2	-154.625	97.5625	0	y	None	g	10.0	Reaction Cap, Top, SE Corner; East = +
	26	Acceleration	A15	Q2913	UCLA	Kinemetrics	ES-T	1443	3	-154.625	97.5625	0	x	None	g	10.0	Reaction Cap, Top, SE Corner; South = +
Q- B	27	Acceleration	A16	Q2914	UCLA	Kinemetrics	ES-T	1189	1	174	0	-22	z	None	g	10.0	Backfill, Mid-depth, 4th South; Down = -
	28	Acceleration	A17	Q2915	UCLA	Kinemetrics	ES-T	1189	2	174	0	-22	y	None	g	10.0	Backfill, Mid-depth, 4th South; East = +
	29	Acceleration	A18	Q2916	UCLA	Kinemetrics	ES-T	1189	3	174	0	-22	x	None	g	10.0	Backfill, Mid-depth, 4th South; South = +
Q-A	30	Acceleration	A19	Q2921	UCLA	Kinemetrics	ES-T	1190	1	156	0	-22	z	None	g	10.0	Backfill, Mid-depth, 2nd South; Down = -
	31	Acceleration	A20	Q2922	UCLA	Kinemetrics	ES-T	1190	2	156	0	-22	y	None	g	10.0	Backfill, Mid-depth, 2nd South; East = +
	32	Acceleration	A21	Q2923	UCLA	Kinemetrics	ES-T	1190	3	156	0	-22	x	None	g	10.0	Backfill, Mid-depth, 2nd South; South = +
Q-B	33	Acceleration	A22	Q2924	UCLA	Kinemetrics	ES-T	1191	1	-356	-97.3125	0	z	None	g	10.0	Reaction Cap, Top, NW Corner; Down = -
	34	Acceleration	A23	Q2925	UCLA	Kinemetrics	ES-T	1191	2	-356	-97.3125	0	y	None	g	10.0	Reaction Cap, Top, NW Corner; East = +
	35	Acceleration	A24	Q2926	UCLA	Kinemetrics	ES-T	1191	3	-356	-97.3125	0	x	None	g	10.0	Reaction Cap, Top, NW Corner; South = +
White Hub	36	Acceleration	A25	Q2941	UCLA	Kinemetrics	ES-U	541	1	156	0	-11	X	White HUB	g	10.0	Backfill, Upper Depth, 2nd South; South = +
White Hub	37	Acceleration	A26	Q2942	UCLA	Kinemetrics	ES-U	542	1	192	0	-22	X	White HUB	g	10.0	Backfill, Mid-depth, 3rd South; South = +
BNC-C	38	Displacement	D9	Q2944	BYU	Ametek	P-20A	0704-22057	1	0	-103	-32		9.97VDC Excitation	in	0.50	Test Cap, West Side, Top; South = +
BNC-C	39	Displacement	D10	Q2945	BYU	Ametek	P-20A	0704-22055	1	-150.5	-103	-6		9.97VDC Excitation	in	0.50	Reaction Cap, West Side, Top; South = -
BNC-D	40	Earth Pressure	P1	Q2811	BYU	Geocon	3500	1500	1	120	0.4	-28.25	X	13VDC excitation	kPa	0.00833	Test Cap, South Face, 3rd Down, Far East
BNC-D	41	Earth Pressure	P2	Q2812	BYU	Geocon	3500	1497	1	120	-7.85	-15.25	X	13VDC excitation	kPa	0.00833	Test Cap, South Face, 2nd Down, East
BNC-D	42	Earth Pressure	P3	Q2813	BYU	Geocon	3500	1501	1	120	-16.1	-34.5	X	13VDC excitation	kPa	0.00500	Test Cap, South Face, 4th Down, West
BNC-D	43	Earth Pressure	P4	Q2814	BYU	Geocon	3500	1496	1	120	-24.35	-8.5	X	13VDC excitation	kPa	0.00500	Test Cap, South Face, 1st Down, Far West
BNC-D	44	none		Q2815	BYU												
BNC-D	45	none		Q2816	BYU												
BNC-E	46	none		Q2721	BYU												
BNC-E	47	none		Q2722	BYU												
White Hub	48	Acc. UniAxial	A27	Q2724	UCLA	Kinemetrics	ES-U	543	1	138	0	-22	y	White HUB	g	10.0	Backfill, Mid-depth, 1st South; South = +
White Hub	49	Acc. UniAxial	A28	Q2725	UCLA	Kinemetrics	ES-U	544	1	156	0	-44	y	White HUB	g	10.0	Backfill, Lower Depth, 2nd South; South = +
Q-A	50	Acceleration	A29	Q2771	UCLA	Kinemetrics	ES-T	1192	1	-60	103.25	0	z	none	g	10.0	Reference Beam, East Side; Down = -
	51	Acceleration	A30	Q2772	UCLA	Kinemetrics	ES-T	1192	2	-60	103.25	0	y	none	g	10.0	Reference Beam, East Side; East = +
	52	Acceleration	A31	Q2773	UCLA	Kinemetrics	ES-T	1192	3	-60	103.25	0	x	none	g	10.0	Reference Beam, East Side; South = +
Q-B	53	Acceleration	A32	Q2774	UCLA	Kinemetrics	ES-T	1193	1	-60	-103.25	0	z	none	g	10.0	Reference Beam, West Side; Down = -
	54	Acceleration	A33	Q2775	UCLA	Kinemetrics	ES-T	1193	2	-60	-103.25	0	y	none	g	10.0	Reference Beam, West Side; East = +
	55	Acceleration	A34	Q2776	UCLA	Kinemetrics	ES-T	1193	3	-60	-103.25	0	x	none	g	10.0	Reference Beam, West Side; South = +